Universität Hamburg
DER FORSCHUNG | DER LEHRE | DER BILDUNG

On Anisotropies of Ultra-high Energy Cosmic Rays

Dissertation zur Erlangung des Doktorgrades
an der Fakultät für Mathematik, Informatik und Naturwissenschaften
der Universität Hamburg

vorgelegt von

Andrej Dundović

aus Koprivnica, Kroatien

Hamburg, 2018

Gutachter der Dissertation:

Prof. Dr. Günter Sigl

Prof. Dr. Dieter Horns

Gutachter der Disputation:

Prof. Dr. Marcus Brüggen

Prof. Dr. Dieter Horns

Prof. Dr. Jochen Liske

Prof. Dr. Günter Sigl

Dr. Alexander Westphal

Datum der Disputation: 25. 06. 2018

Vorsitzender des Pröfungsausschusses:

Prof. Dr. Jochen Liske

Vorsitzender des Promotionsausschusses:

Prof. Dr. Wolfgang Hansen

Dekan der Fakultät für Mathematik,
Informatik und Naturwissenschaften:

Prof. Dr. Heinrich Graener

...dobri moj čitatelju, ne požali truda,
pak izađi sa mnom o sunčanom zapadu
iz tijesne izbe svoje i uskih ulica,
gdje jedva vidiš to krasno nebo, na otvorenu ravnicu
i posveti koju uru motrenju pojava, kojima ćeš biti svjedok.
Naći ćeš doduše dosta ljudi, koji će te gledati u čudu,
što li nalaziš u tome zabave, da se zadubljuješ u to nebo,
jer žalibože danas tisuće i tisuće i obrazovanih ljudi
svaki dan gledaju te krasne pojave, a da ih ne vide.
Neka ti oni ne budu mjerilom, rđav uzgoj,
pretjerana borba za svakidašnji život,
možda i niske strasti ugušile su u njima polet srca,
koji već ne može da shvaća takovih užitaka.
Ne dao nam Bog da ikad, pa ni u dubokoj starosti,
padnemo na te niske grane!
Oton Kučera, *Naše Nebo* (1895)

Zusammenfassung

Diese Dissertation behandelt den Einfluß der Verteilung der Quellen kosmischer Strahlung sowie der kosmischen Magnetfelder auf die Anisotropie von Einfallsrichtungen kosmischer Strahlung mit Fokus auf ultra-hohe Energien. Präsentiert werden die zwei hauptsächlichen Untersuchungen dieses Sachverhalts sowie eine Nebenthematik, welche für diese beiden wichtig ist.

Der erste Themenbereich befasst sich mit der Anisotropie verursacht durch eine einzige Quelle, wobei der Beitrag aller anderen Quellen als isotrop angenommen wird. Der Fluss kosmischer Strahlung wird beeinflusst von turbulenten Magnetfeldern, welche die Einfallsrichtungen zerstreuen. Diese Zerstreuung wird mit einer Fisher Distribution nachgestellt. Dieses Modell wird dann eingeschränkt durch Vergleich mit Messungen des Pierre Auger Observatoriums, insbesondere der beobachteten dipolaren Anisotropie. Mit der Kleinwinkelnäherung ergibt sich der quadratische Mittelwert des Ablenkungswinkels zur Sichtlinie zu $\left(50^{+11}_{-10}\right)^\circ$. Es wird gezeigt, dass der Ablenkungswinkel noch größer wäre, falls die Teilchen verschiedene Gebiete eines strukturierten Feldes passieren würden. Die Anwendung dessen auf zwei potenzielle Quellen, Cen A und das Virga Cluster, liefert eine Abschätzung der Kohärenzlänge und Feldstärke des dazwischenliegenden tubulenten Magnetfeldes.

Der zweite Themenbereich behandelt die Auswirkung von Magnetfeldern auf Anisotropien indem es die Anwendbarkeit von Liouville's Theorem auf kosmische Strahlung untersucht. Das Konzept des Einfangens kosmischer Strahlung wurde herausgestellt als eine potenzielle Ursache von Anisotropien und ein Beispiel dessen Anwendung wird demonstriert. Das Einfangen in einem strukturierten feld kann dipolare Anisotropien hervorrufen.

Das Nebenthema erforscht den Übergang von geradliniger zu diffusiver Propagation und leitet ein präzises Kriterium für den Fall turbulenter Magnetfelder ab.

Abstract

This dissertation deals with the influence of cosmic ray source distributions and cosmic magnetic fields on anisotropies in the arrival directions with a focus on the ultra-high energy range. Two main investigations regarding the subject are presented and one side topic important for the first two.

The first topic is the study of anisotropies caused by a single source where the rest of sources are contributing only isotropically. The cosmic ray flux is affected by a turbulent magnetic field which spreads the arrival directions, and that spread is modelled with a Fisher distribution. The model is then constrained against measurements of the Pierre Auger Observatory, especially against its dipolar anisotropy. Under the small angle approximation, this gives the root mean square angular deflection with respect to the line of sight of $\left(50^{+11}_{-10}\right)^{\circ}$. It is shown that the angular deflection would be even greater if particles were crossing different domains of a structured magnetic field. When applying this to two potential nearby sources, Cen A and the Virgo cluster, estimates between the coherence length and field strength are obtained for the intervening turbulent magnetic field.

In the second topic, effects of magnetic fields on anisotropies are considered by inspecting the applicability of Liouville's theorem on cosmic ray anisotropies. The concept of trapping was identified as a potential cause of anisotropies, and one case of its application is demonstrated. It is shown how the trapping in a structured field can generate a dipolar anisotropy.

The side topic explores the transition from the rectilinear to diffusive propagation where a precise criterion is derived for the case of a turbulent magnetic field.

List of Publications

Chapter 4 of this thesis is based on the following publication:

[1] Andrej Dundović and Günter Sigl, *Anisotropies of Ultra-high Energy Cosmic Rays Dominated by a Single Source in the Presence of Deflections*, Submitted to JCAP, [arXiv:1710.05517].

Contents

List of Figures

1 | Introduction

The night sky. It occupies man's interest and fires his imagination, today as well as in ancient times. When Galileo Galilei used his new invention, the telescope, and pointed it at the night sky, he discovered the four largest satellites of Jupiter. That certainly had a tremendous impact on people's way of thinking about the Universe at that time. From that moment on, people started to build bigger and bigger telescopes to improve their senses and to see further and better into mysterious realms of the Universe. Although our understanding of the astronomical phenomena improved greatly from Galileo's times, the fascination with cosmic phenomena has never dried up.

In the last more than a hundred years, people observed a phenomenon of radiation in our atmosphere that undoubtedly comes from above, from Space. This phenomenon was first named "cosmic radiation", and a bit later "cosmic rays", the name that survived to the present day, even though today we know that the "rays" part is not strictly correct since this phenomenon consists of particles, not rays. Nowadays, we see cosmic rays as charged energetic subatomic particles that constantly bombard our planet. The most energetic of them initiate in the atmosphere showers of secondary particles, which can spread over a $10\,\mathrm{km}^2$ area on the ground level. Kinetic energies of these particles range from below 10^9 eV up to a few 10^{20} eV, and, as such, cosmic rays represent a unique phenomenon which continuously extends in energy over the broader orders of magnitude known to mankind. Needless to say, cosmic rays of the highest energy, named ultra-high energy cosmic rays or UHECR for short, are the most energetic phenomenon, which by far exceeds the energies of particle accelerators such as the Large Hadron Collider. Their immense energy brings two fundamental, interconnected questions that motivate many

researchers in the world to explore them. What kind of subatomic physics emerges on those energies? Where does Nature create those particles in the first place?

While the former question can be seen as a continuation of fundamental research in elementary particle physics, the latter one fits more as an astrophysical topic. The latter question, the question of the "origin", can be restated in an astronomical form: can high energy cosmic rays serve as a new kind of astronomy - astronomy of charged particles that would line up with other new astronomies, such as gamma-ray astronomy, high-energy neutrino astronomy, and gravitational wave astronomy? In that way, we would get another "eyes" to use to see new phenomena of the Universe, as Galileo did with his telescope.

Unfortunately, the charged nature of cosmic rays together with the existence of omnipresent cosmic magnetic fields makes this quest troublesome, if not daunting. The Lorentz force inevitably bends cosmic ray trajectories; magnetic field irregularities scatter them; different types of interactions change their composition and reduce their energy. All of that eventually makes the information about their origin seemingly lost. It has to be clarified that the origin of cosmic rays depends on their energy, and not that a single acceleration mechanism is responsible for the whole energy range.

Direct evidence of major acceleration mechanisms for energies up to GeV come from spacecraft missions, for example. These mechanisms are identified as interplanetary shock waves associated with the solar wind, and as solar flares. Furthermore, although not *in situ* observed, it is well argued, by several independent arguments, that cosmic rays up to PeV energies come from our galaxy, where the commonly considered acceleration mechanisms are located in supernova remnants and high-energy binary systems. However, the origins and acceleration mechanisms of cosmic rays above the PeV energy range remains under continuous debate without strong support for any proposed hypothesis.

The origin of cosmic rays of the highest energies is a topic of special interest even for the researchers outside of the cosmic ray community. Those cosmic rays of energies up to 20 joules per particle are in every aspect extreme, so the assumption is that

they originate from an equally extreme environment, which could reveal new insights for fundamental questions of matter. Yet, it is not clear what sources and associated mechanisms are responsible for them. What significantly complicates the origin problem is that those cosmic rays apparently originate outside of our galaxy, where our knowledge and experimental reach is even weaker than in our galaxy, where it is already unsatisfactory.

Without sufficient knowledge of the positions of UHECR sources and the structure and strength of the intervening magnetic fields, it is difficult to discriminate between the influences of magnetic fields and the source distribution within the cosmic rays framework alone. The cosmic ray research relies on advancements in other fields, and especially in determining galactic and extra-galactic magnetic fields.

The recent discovery of the dipolar anisotropy by the Pierre Auger Observatory above $8 \times 10^{18}\,\mathrm{eV}$ is the first distinct feature in the context of UHECR arrival directions; the first sign of anisotropy in that energy range. The motive of this thesis is to explore possible causes of this feature, but to do so, the problem of the cosmic ray propagation has to be systematically analysed. What follows is the examination of a simple model of a single source of cosmic rays and how it influences the anisotropic pattern that can be observed, while taking into account the non-trivial propagation through a turbulent field. Finally, effects of magnetic fields on the anisotropies are studied, and the hope is that the Auger Prime, the ongoing upgrade of the Pierre Auger Observatory, which should be able to distinguish better the composition of UHECR per event, would give new valuable data to learn more about those effects.

This thesis is structured as follows. Chapter 2 depicts the historical development of the research field by going through the most important steps that were made so far to reach today's level of knowledge, including, at the very end, a review of the current status of observations. Special but brief attention is given to the Pierre Auger Observatory as being the main source of new findings in the last decade in the context of ultra-high energy cosmic rays, and because it is the cosmic ray experiment best known to the author since the author participated in its activities for the past three years.

The role of this chapter is also to introduce the terminology used later pedagogically. Chapter 3 is where the theoretical foundations necessary to understand the propagation of cosmic rays are laid down and how they interact with turbulent magnetic fields. The problem of transitioning between the rectilinear propagation to diffusion is inspected in the last section. Chapter 4 condenses the study of anisotropies that are caused by a single source where the cosmic rays are deflected by a turbulent magnetic field, while the rest of the sources are considered to contribute isotropically. In the following sections of that chapter some derived topics are also presented: the effects of structured fields on the model; constraining the model parameters by the experimental data of large-scale anisotropies, and giving some prediction for relevant quantities, where the prediction of dipolar amplitude on energies beyond currently measured is maybe the most important one; a short discussion how a group or cluster of sources could replace a single source. Chapter 5 investigates the consequences of Liouville's theorem on anisotropies and gives an example and a demonstration where this could no longer apply. In the appendix, two technical topics that are significantly used in the main part are covered: relevant topics of spherical harmonics and a description of the cosmic ray propagation framework - CRPropa.

2 | Historical overview and current status

A systematic approach to any research matter is generally accomplished in two ways. One way is to use a formal system composed of definitions or axioms, theorems, lemmas and corollaries, which is known since the time of Euclid's Elements [2] and later frequently used through the whole history of western science, like in Newton's Principia [3], Maxwell's Theory of Electromagnetism [4] or it is often how nowadays quantum mechanics is introduced [5, 6]. Not to mention modern mathematics, which probably cannot be imagined without its use. It can be said that a topic of interest can be presented in this way if it forms, to some degree, a closed system of concepts and their mutual relations [7, *Non-Relativistic Quantum Mechanics*, ch. 6] and is concerned mainly of theoretical, abstract or formal considerations, i.e., if it forms a theory. Another way, on the other hand, is to describe the development of a topic and its main ideas in the fashion in which it really progressed, in a historical context. This is probably less grateful since it cannot encompass the conciseness, completeness and elegance of the former one, but despite this, it does not need an external motivation or justification since its causality is already given by history itself. This approach could be appropriate for most research subjects, especially for those who still have many open questions.

The field of cosmic rays is, before anything else, a phenomenological subject which is still being actively developed. In it, even around main concepts such as the definition of cosmic ray, there is no strict consensus in the community. For example, in Stanev's book [8] "Cosmic rays are often defined as charged particles that reach the Earth from

interstellar space. (...) Neutral particles are obviously not included (...)", V. L. Ginzburg uses "mostly relativistic" particles in his definition [9], Thomas K. Gaisser is more specific [10] "(Cosmic ray particles) are ionized nuclei (...)" while, on contrary, in some texts electrons and positrons are counted [11, 12] or even neutral particles [13]: "(ultra-high energy cosmic rays) are mostly charged particles". Clearly, different definitions occupy different aspects of research and are chosen to deal with different sides of the phenomenon. For an experimentalist who measures an extensive air shower, there is no clear distinction between various particles that initiated the shower as that cannot be measured, only inferred. Thus, narrowing the subject of interest only to charged particles would go without a basis in experimental data. This can be seen in the fact that the Pierre Auger Observatory, although built as a cosmic ray observatory, in principle can detect photons [14] and neutrinos [15]. A theoretician thinks about the questions of definition differently. If she keeps the definition extensively wide, that leads to an inability to accurately describe her theoretical model. The wider the definition is, the more mechanisms have to be included in the model which, therefore, makes it difficult to draw unambiguous and falsifiable statements from it.

Since the formal definition cannot be given unambiguously, the only proper way to demonstrate the evolution of cosmic ray concepts is to derive them from historical considerations where the interplay of the theory and the experiment took place. These considerations will present how many hypotheses, to explain differences in observed phenomena, were made among which many were refuted with experiments. Later, some of them were restored by re-interpreting old experiments or in light of new experiments. Although the process is somehow chaotic, it can be concluded that the overall knowledge about this matter qualitatively improved. That idea of the dialectical development of knowledge on examples of mathematical topics is vividly expressed in Imre Lakatos' well-known book Proofs and Refutations [16], but the author of this work speculates that it could be applied universally, thereby, in the field of cosmic rays too.

Another reason for reviewing the history of the subject is that it can nicely show how some conclusions are trivial and evident today but were enigmatic and dubious fifty

years ago, and that can serve as a good motivation for further research as the nature of any subject is infinite and one can never close it marking it as "solved". The process of gaining knowledge always opens new questions which one did not even know that existed. The whole history of science can serve as an example of that.

2.1 Discovery of radiation

The history of cosmic rays probably could not begin without the development of a theory of electric and magnetic phenomena and without understanding the phenomenon of radiation.

Although empirically known from ancient times as a property of amber and loadstone (magnetite), which as witnesses stand the Greek etymology of the modern words ἤλεκτρον (elektron) for amber and μαγνῆτις λίθος (magnētis lithos) for loadstone, a scientific theory of electric and magnetic phenomena was explored and developed at the end of the 18th and in the 19th centuries by many workers, such as Coulomb, Volta, Ampère, Ørsted, Ohm and Faraday, among others. Finally, by 1865 James Clerk Maxwell was the one who established it as a complete mathematical framework [4] which is known today as classical electrodynamics.

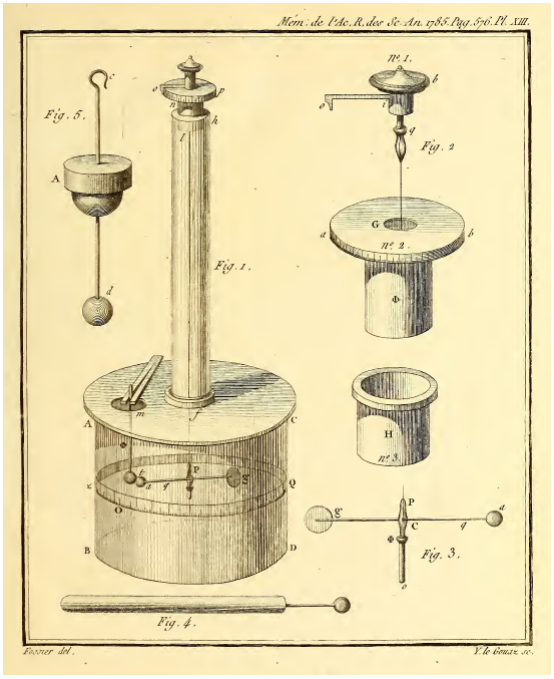

Figure 2.1: The sketch of a torsion balance electrometer, a device with which Coulomb performed his measurements. The figure is taken from [17], licensed under public domain.

The theory of electrodynamics provided necessary mathematical tools to explore related phenomena such as radiation, which was started to be systematically investigated at the end of 18th century by the work of H. Herz, P. Lenard and W. Röntgen. Firstly,

it was considered as a form of electromagnetic radiation predicted by Maxwell, but soon it showed new properties so that the differentiation and a better understanding of it waited until the beginning of the 20th century in the light of new technical inventions [18]. Brief reviews of important discoveries are listed next.

In 1785, Charles-Augustin de Coulomb, by using his invention, the torsion balance electrometer (fig. 2.1), reported that the device spontaneously discharges due to the action of the air rather than by defective insulation [17]. Coulomb's observation was later confirmed by M. Faraday and W. Crookes who further improved the experiment. At this point, the effect was known to be caused by some sort of radiation which ionizes the air inside of the electroscope, but the source of this radiation remained unknown.

It is interesting that further progress came after the invention of the photographic plate. This invention was a result of a centuries-old effort of how to faithfully convey a picture seen through *camera obscura* (see the history of photography [19] for details, or from a physicist's perspective [20]).

From 1886 to 1889, in a series of experiments, H. Hertz discovered electromagnetic waves. His student P. Lenard expanded his supervisor's work focusing on cathode rays, but it was Wilhelm Röntgen who used a photographic plate while experimenting with Hertz's and Lenard's cathode tubes and found X-rays in 1895 [21]. "It seemed at first a new kind of invisible light. It was clearly something new, something unrecorded..." he wrote at that time. The term "rays" was picked on account of their property of propagating themselves in straight lines as light does. The actual constitution of this radiation of energy was still unknown [22]. A year later, Henri Becquerel investigated further Rötgen's rays which led him to find that uranium salts emit penetrating radiation which, again, was registered on a photographic plate. By inspecting the properties of this phenomenon, Becquerel realized that it has distinct properties compared to X-rays, so he concluded that this is a new form of radiation. His work was continued by Pierre and Marie Curie radioactivity, which was recognised as the discovery of radioactivity [22]. They showed that radioactive elements emit radiation which ionises the air. The pioneering work of Ernest Rutherford in the following years gave the differentiation of

radiation into charged alpha and beta, and neutral one – gamma radiation.

The simplest explanation of Coulomb's observation of the spontaneous discharge of the electroscope at that point was due to the newly discovered radioactivity of radioactive materials, as it was the mechanism which was already experimentally demonstrated [23]. Other possibilities were that it originates from the atmosphere or it has an extra-terrestrial source, which was speculated already by Nikola Tesla in his patent about the method of utilizing radiant energy in 1901 [24]: "My own experiments and observations lead me to conclusions (...) that sources of such radiant energy throw off with great velocity minute particles of matter which are strongly electrified", and "The rays of radiations (...) may be derived from a natural source, as the sun, (...)".

2.2 Search for the sources of radiation

Julius Elster and Hans Geitel at the beginning of the 20th century conducted a series of different measurements by isolating electroscopes with a thick metal box, where again they observed the same phenomena which led them to the conclusion that the radiation has to be highly penetrating [25]. Charles Thomson Rees Wilson did underground experiments to see if natural radioactivity would decrease [26]. He did not find any reduction from which he concluded that natural radioactivity is not extra-terrestrial in origin [27]: "It is unlikely, therefore, that the ionisation is due to radiation which has traversed our atmosphere; it seems to be, as Geitel concludes, a property of air itself." Theodor Wulf improved the measuring device and used it to investigate the dependence of radiation on altitude by using the 300 metres elevation of the Eiffel tower [28, 29]. Unfortunately, unknowing that the metal of the tower also contributed to radioactivity, the results of his measurements were dubious and inconclusive regarding whether the radiation increases or decreases with height.

Domenico Pacini questioned the Earth's crust origin of radioactivity and carried out a series of experiments on and below the sea surface. He found out that radiation is still present and it falls with depth. Thus, he concluded that the reason should be from an extra-terrestrial contribution [30] (English translation from [23]): "[it] appears from the

results of the work described in this Note that a sizable cause of ionisation exists in the atmosphere, originating from penetrating radiation, independent of the direct action of radioactive substances in the soil."

Figure 2.2: Victor Hess and his balloon crew in one of many balloon experiments taken in 1911 and 1912. Source: APS, licensed under public domain.

The first experiments during balloon flights took place to investigate Wulf's altitude results. By ascending up to 4,500 metres above sea level, Albert Gockel found out that the ionisation did not decrease with height as expected in the hypothesis of terrestrial origin and confirmed Pacini's conclusion. Gockel also introduced the term "kosmische Strahlung" in his writings to Wulf [31]. In his thesis, Erwin Schrödinger demonstrated that the altitude results could be explained if a part of radioactivity comes from Earth and a part from above [23].

Finally, balloon flights conduced by Victor Hess (fig. 2.2) in 1911 and 1912 up to 5,000 metres gave enough of precise experimental data from which he concluded that the increase of ionisation with height must be due to radiation coming from above, probably extra-terrestrial in origin [32, 33] (English translation in [27]): "The discoveries revealed by the observations here given are best explained by assuming that radiation of great penetrating power enters our atmosphere from the outside and engenders ionisation even in counter lying deep in the atmosphere." Additionally, he saw no difference in the radiation between night and day, and during an eclipse implying that the Sun is not directly responsible. His results were later confirmed by the work of Kolhörster at even higher altitudes up to 9,300 metres [34].

2.3 First observed properties of cosmic rays

The First World War interrupted the research of cosmic rays. After the war, in 1926, R. A. Millikan and G. H. Cameron continued with experiments, measured the radiation at various depths in lakes at high altitudes [35] and reported that the underwater ionisation rate of the lower lake corresponded to the rate obtained approximately two metres deeper in the higher lake. This showed that two metres of water in lakes absorbed about the same amount of radiation as almost two kilometres of air. Although Millikan admitted that the radiation comes from above, he coined the term "cosmic rays" because he was convinced that the radiation was electromagnetic in nature due to its incredible penetrating power which was then only related to gamma rays. The conclusion was wrong, but the name stayed to this day. Improvements of Geiger-Müller tubes soon after enabled Kohlörster and Bothe to make a comparison between the known corpuscular radiation and cosmic radiation in which they noticed similarities and that led them to infer the corpuscular property of cosmic rays [36] (English translation in [27]).

In several expeditions, of which an especially important was the one in 1930 from Amsterdam to Bangkok, J. Clay observed that the penetrative power of the primary cosmic rays decreases with latitude [37]. Later Arthur Compton confirmed those results [38, 39] and inferred that this could be caused by the Earth's magnetic field if cosmic rays are (mostly) charged particles, making the Millikan claim about the non-charged property unconvincing.

Another insight into the nature of cosmic rays followed from Alvarez, Compton [40] and Bruno Rossi [41]. Rossi demonstrated that the Earth's magnetic field bent incoming charged particles and measured near the geomagnetic equator the higher flux in west-east direction compared to the east-west one concluding that cosmic rays are predominantly positive. In addition, during his experiments which employed improved Bothe's coincidence method, Rossi noticed that his detectors, even in a triangle configuration where a cosmic ray could not transverse all of them, gave coincidental signals from which he assumed the production of showers of secondary particles [42]. In spite

of this, the discovery of extensive air showers that cover a large area is attributed to Pierre Auger and his collaborators [43] since they not only performed measurements of correlation between separated detectors but also indicated that the energy of a primary particle, which produces a shower by colliding with air molecules, could reach the energy of 10^{15} eV. That energy was several orders of magnitude higher than any known before.

In the following years, Marcel Schein, by isolating detectors with thick lead walls, came to the conclusion that primary cosmic rays cannot be electrons and should be composed mostly of protons at $10^9 - 10^{12}$ eV [44].

In the thirties and forties, measurements of cosmic rays also gave a lot of additional discoveries. Probably the best known are the discovery of the positron (Anderson, 1933 [45]) and the muon (Neddermeyer and Anderson, 1936 [46]), but after a decade, the investigation in high energy particle physics turned to man-made particle accelerators.

2.4 Consequences of extensive air showers

Extensive air showers revealed the existence of highly energetic particles, but they also brought many difficulties by themselves. Most notably is the difficulty of identifying primary cosmic ray properties such as its energy, composition and directional information from the air shower event. These quantities are not as easy to determine from the air showers as before, with direct measurements. Thus, the theoretical work and advancements in other areas, such as measurements of nuclear cross-sections in particle accelerators, were needed to enable further progress in cosmic ray experiments.

Fortunately, already by 1937, Bethe, Heitler, Bhabha, Carlson and Oppenheimer in series of papers developed a concept of electromagnetic cascades from which a better qualitative inference about the primary cosmic ray that caused the extensive air shower could be made [47, 48, 49].

By employing the cascade theory, a series of experiments observed that the energy of primary cosmic rays stretches over an immense energy range, but the occurrence frequency of events on higher energies was rapidly decreasing. The decrease in the energy spectrum could be described with an inverse power law, which raised the question of

origin since a power law behaviour is considered as a signature of a non-thermal process of the acceleration. To explain this, Enrico Fermi in 1949 [50] proposed a mechanism of acceleration by collisions against a moving magnetic field front which can yield such a spectrum, although, particles are already required to have some initial energy before they can gain energy in Fermi's process, what is known as the injection problem.

More precise data measurements brought into light the first distinct feature of the energy spectrum observed in 1959. The feature is the steepening of the spectrum around 10^{16} eV [51]. It was called the "knee" due to its resemblance to the shape of a human leg (see fig. 2.4).

In the following decades, many array experiments for detection of air showers were built. Technologically, this was led by the application of photomultiplier tubes (PMTs) which succeed Geiger-counter techniques. A detailed overview of those experiments, experimental techniques and new analysis that they employed can be found in [42], but the most important ones can be highlighted.

John Linsley at the Volcano Ranch experiment (New Mexico) reported the detection of a primary cosmic ray of energy 10^{20} eV [52]. Also, he reported a hint of a flattening of the spectrum above 10^{18} eV [53]. The Haverah Park experiment (1964 – 1987) built in the UK recognised and confirmed those results, but it took a few decades and more ambitious experiments such as AGASA and Fly's Eye until these results were established as unambiguous.

The discovery of the cosmic microwave background (CMB) radiation by Penzias and Wilson [54] had a consequence on the interpretation of the cosmic ray energy spectrum. Greisen [55] and, independently, Kuzmin and Zatsepin [56] predicted that the microwave background should limit the maximum energy of cosmic rays because above 5×10^{19} eV cosmic rays significantly interact with CMB photons via Δ resonance:

$$\gamma_{\mathrm{CMB}} + p \rightarrow \Delta^{+} \rightarrow p + \pi^{0}, \tag{2.1}$$

or

$$\gamma_{\mathrm{CMB}} + p \rightarrow \Delta^{+} \rightarrow n + \pi^{+}. \tag{2.2}$$

That means that ultra-high energy cosmic rays coming from sources beyond the local galactic supercluster (more than 50 Mpc) rapidly lose their energy by collisions with the CMB photons and that should be observed as a spectrum cut-off in the case where cosmic rays are not accelerated in Milky Way's neighbourhood.

Another important theoretical consideration was brought by B. Peters in 1961 [57]. Motivated by the discovery of the "knee" feature, he examined the possibility of shifting that feature based on the composition of the primary cosmic rays, which can be caused either by a limitation of the electromagnetic acceleration processes or by the leakage of particles from the galaxy. That would, for example, mean that iron nuclei can be accelerated by the cosmic ray source to higher energies compared to protons, or can be contained better in the galactic magnetic field, which would be seen as composition cycles, named Peter's cycles, in the energy spectrum. Forty-five years later, experiments KASCADE and KASCADE-Grande identified this spectral steeping of the heavy component at about 8×10^{16} eV which is in agreement, e.g. 26 times higher, if the light component knee is at about 3 to 5 10^{15} eV [58, 59].

2.4.1 The Pierre Auger Observatory

Nowadays giant air shower arrays succeeded kilometre-scale arrays to access the energy spectrum above 1 EeV. Two such observatories currently operate and actively contribute with new findings. These are the Pierre Auger Observatory (later only PAO) [60, 61] and the Telescope Array (later only TA) [62]. TA is located in the northern hemisphere, in Utah, U.S., while PAO is located in the southern hemisphere, in the Province of Mendoza, Argentina. In both cases, a hybrid technique of air shower detection is used that combines fluorescence detectors (FD) and surface detectors (SD), but the difference is that in case of TA scintillation detectors serve as surface detectors and in case of PAO these are water Cherenkov tanks. The fluorescence detectors work only during clear moonless nights and observe the longitudinal shower development which gives a calorimetric energy measurement. The surface detectors in principle have a 100% duty cycle and observe particles on ground level, i.e., capture the air shower lateral

distribution. As they observe mutually orthogonal components of the air shower, these two techniques are complementary.

A brief description of the Pierre Auger Observatory is given in the following few paragraphs. The focus is on PAO since the author is a member of the Pierre Auger Collaboration and, therefore, more familiar with details of its operation. For more detailed descriptions the reader is referred to the instrumentation papers [60, 61, 63, 64, 65, 66].

The Pierre Auger Observatory was first proposed in 1992 by Jim Cronin and Alan Watson, its construction started in 2000 and finished in 2008, but it is recording showers since 2004 when the array was still incomplete. It is built on a flat elevated plateau in average 1400 metres above sea level at the south of the Province of Mendoza, next to the city of Malargüe. This altitude is chosen as it has a favourable atmospheric depth of 875 cm^2 for ground experiments at which vertical cosmic-ray showers originated from ultra-high energy cosmic rays already reached their maximum shower development yet the shape of the vertical shower profile around the maximum can still be well captured by the fluorescence detectors. The fluorescence detectors are extremely sensitive to light so a rather low amount of light pollution around Malargüe provides good conditions for these techniques. One cannot intuitively express what is meant by low light pollution, but as the light pollution roughly correlates with the population living in the area, it is illustrative to notice how this part of Argentina is largely unpopulated with 0.8 inhabitants per square kilometre [67]. To put this number into perspective, Hamburg has 2397 while Germany has 231 inhabitants per square kilometre [68]. On top of that, the dry weather conditions of this location are also favourable for the experiment.

The PAO surface detector array [63] (the right panel of figure 2.3) consists of more than 1600 water Cherenkov tanks on the area of 3000 km^2 arranged on a triangular grid with 1.5 km spacing in between. Additional 49 stations are placed more densely on the area of 24 km^2 with 750 m spacing in between to measure lower energy showers. A 10 m^2 cylindrical water tank holds 12 t of ultra-pure water in a sealed liner with a reflective inner surface. Three photomultiplier tubes (PMTs) are immersed in the water

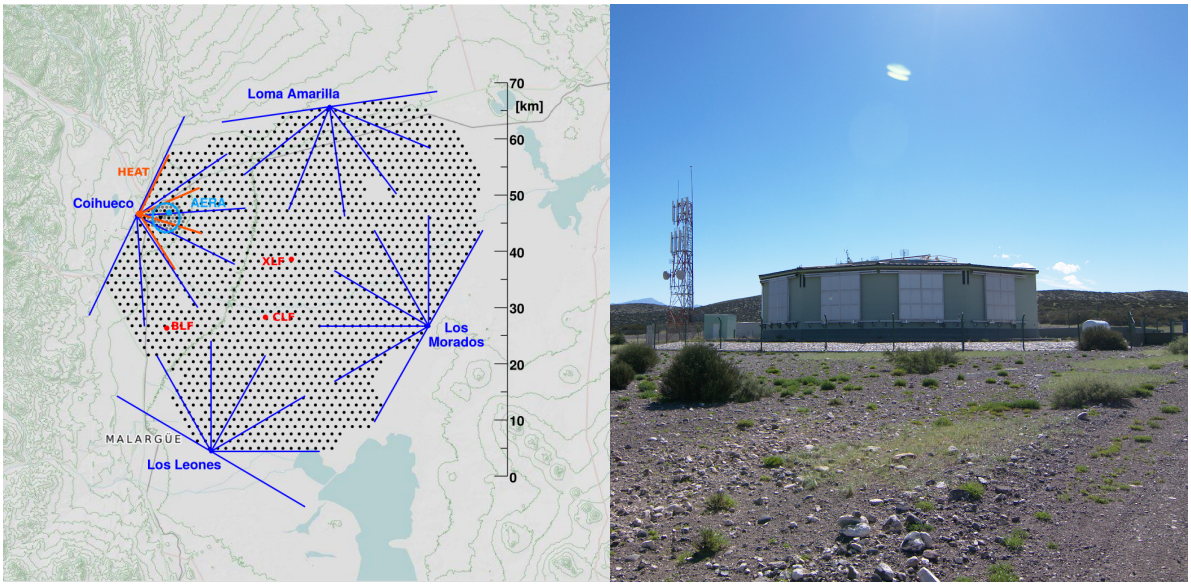

Figure 2.3: On the left is the layout of the Pierre Auger Observatory showing the grid of surface detectors and four locations where fluorescence detectors are housed (Courtesy of Darko Veberic, the Pierre Auger Observatory, licensed under CC-BY-SA). On the right is a photo of an FD building, namely Coihueco. As it can be seen, during the day the telescopes are protected from the daylight with shutter doors.

from above and records the Cherenkov light. The Cherenkov light is produced when a relativistic charged particle interacts with the water. The recorded data is wirelessly transmitted via FD stations, the central data acquisition systems at the observatory campus. The tank's electronics are powered by two batteries which are charged by two solar panels.

The fluorescence method [64] is implemented with 24 fluorescence telescopes distributed at four different locations in blocks of six telescopes. They are pointed horizontally just above the ground where surface detectors are deployed. Each FD location covers a 180° azimuthal angle in a way that each of the six telescopes has a $30° \times 30°$ field of view. The left photo in figure 2.3 depicts one FD building which houses six telescopes. The telescopes themselves are based on a modified Schmidt camera design which is composed of an aperture, corrector ring, mirror and a PMT camera. This system partially corrects spherical aberration and eliminates coma aberration. Fluorescence light passes through a $3.8\,\mathrm{m}^2$ large circular opening, a UV pass filter glass window which improves the signal-to-noise ratio by reducing unwanted EM frequencies. After

the UV filter, the light is refracted by an annular lens and reflected by the $13\,\mathrm{m}^2$ large spherical mirror and directed to the PMT camera placed at the focal plane of the mirror. Three additional telescopes called "High-Elevation Auger Telescopes" (HEAT), built as an extension of the original telescopes, are angled more toward the sky to record air showers of lower energy which develop at higher altitudes.

Both surface and fluorescence detectors record and classify an event when certain patterns and conditions are met, implemented through various on-line (local) and off-line (post-processing) triggers. These triggers filter the noise and non-shower signals keeping only relevant recordings. Then, from the collected data, follows the event reconstruction. The surface detector stations can provide information of the arrival times and deposited energy. From that, the shower geometry can be obtained by fitting models to the measured data, consequently determining the arrival direction (the shower axis) and the relative energy estimation. The absolute calibration of the shower energy is done by using so-called hybrid events which are also recorded with the FD. In case of the FD, one can recover the shower properties such as the profile of deposited energy by measuring the flux of photons from the PMT camera and correlating that with the geographical location measured by at least one SD station. One of the most important characteristics in this context of the shower profile is the depth of the maximum energy deposit X_{max} because it is sensitive to the composition of the primary cosmic ray, which means that the composition of the primary can be statistically inferred from it. X_{max} should be interpreted as the point where the shower development reaches the maximum number of particles N_{max}. The exact expression depends on the longitudinal development model, which can be described with, for example, the Gaisser-Hillas function [69]:

$$N(X) = N_{\mathrm{max}} \left(\frac{X - X_0}{X_{\mathrm{max}} - X_0} \right)^{\frac{X_{\mathrm{max}} - X_0}{\lambda}} \exp\left(\frac{X_{\mathrm{max}} - X_0}{\lambda} \right) \tag{2.3}$$

where X_0 is the point where the primary particle interacted for the first time and initiated the shower and λ is a shape parameter. The parameter X is a function of

'slant depth':

$$X(t) = \int_l^\infty \rho(\mathbf{r}(l'))\mathrm{d}l' \tag{2.4}$$

which expresses how much of atmospheric density ρ the shower traversed by moving along the longitudinal coordinate l of the shower axis.

Events are classified into the following categories: vertical, inclined and hybrid events. Vertical and inclined events are distinguished by the zenith angle: those below $\theta < 60^\circ$ are considered as vertical, while those arriving from the 60° to 80° are labelled as inclined. The hybrid events are those detected by the FD in combination with at least one SD station. Events can be detected if they are above a threshold energy which is 3×10^{18} eV for vertical, 4×10^{18} eV for inclined, and 10^{18} eV for hybrid events. Events detected by HEAT and the 750 m array are treated and analyzed separately as they measure air showers of lower energies with a threshold energy of 10^{18} eV and 3×10^{17} eV, respectively.

The Pierre Auger Observatory develops and tests other techniques of shower detection. For example, AMIGA (Auger Muons and Infill for the Ground Array) is a part of the 750 m array which adds underground scintillator muon counters buried below water tanks to measure the muon content of air showers [70]; and AERA (Auger Engineering Radio Array) which investigates the radio technique of measuring the shower signal [71]. At the time of writing this, a testing phase of an important upgrade of the SDs named 'AugerPrime' is underway in which, among other things, on top of every water tank, a scintillator detector will be added [72]. The primary goal of the upgrade is to identify the primary cosmic ray composition better.

2.5 Current status of the main observables

The main observables on which modern experiments concentrate their efforts are the energy spectrum, a statistically expressed composition of primaries depending on energy, and anisotropies in the arrival directions. These will be now presented independently but without physical interpretations since most of the interpretations are still under debate,

and covering all of them equally would be out of the scope of this short overview.

2.5.1 Energy spectrum

Since the beginning of the cosmic ray measurements, the energy spectrum is one of the main observables and it simply represents the total number of particles N crossing an area A in a solid angle Ω per time t with energy E in the form of a differential flux:

$$j(E) = \frac{\mathrm{d}^4 N}{\mathrm{d}A\mathrm{d}\Omega\mathrm{d}E\mathrm{d}t}(E) \tag{2.5}$$

The term "particles" almost universally in this context refers to atomic nuclei.

On figure 2.4, a collected set of measurements of this quantity from various experiments is shown. The chosen set of the plot does not include many other experiments to avoid a clutter, but it is enough to show the main characteristics. The first thing to note is the enormous spread of the spectrum across the 12 orders of magnitude, from 10^9 eV to more than 10^{20} eV. Over the spectrum, the flux rapidly decreases following quite faithfully an inverse power law $j(E) \propto E^{-\gamma}$, where γ in the range from 2.4 to 2.7 [79] for the biggest part of the spectrum. Illustratively, that counts 1000 particles per square metre at 10^9 eV, just one per square metre around 10^{15} eV, and less than one per square kilometre in a century above 10^{20} eV.

The solar activity and the Earth's magnetic field greatly influence the spectrum below the 10^9 eV range, so the flux below that range is usually not perceived as a part of the spectrum. On the other end, the number of detected events is so reduced that it is not easy to make firm conclusions, but the Pierre Auger Observatory, as the largest and, thereby, the most authoritative experiment, detects the flux suppression above 4×10^{19} eV [80], which is also confirmed by TA [81]. The suppression was originally observed with a statistical significance of five standard deviations by HiRes [82].

Other observed features are the steepening of the spectrum from $\gamma \sim 2.6$ to $3.1 - 3.3$ above 3×10^{15} eV and the flattening again to $\gamma \sim 2.7$ at $\sim 5 \times 10^{18}$ eV [83, 84]. The former feature is usually called the 'knee', and the latter is called the 'ankle' due to an association of the shape of the plot to a human leg. Unfortunately for this analogy, the

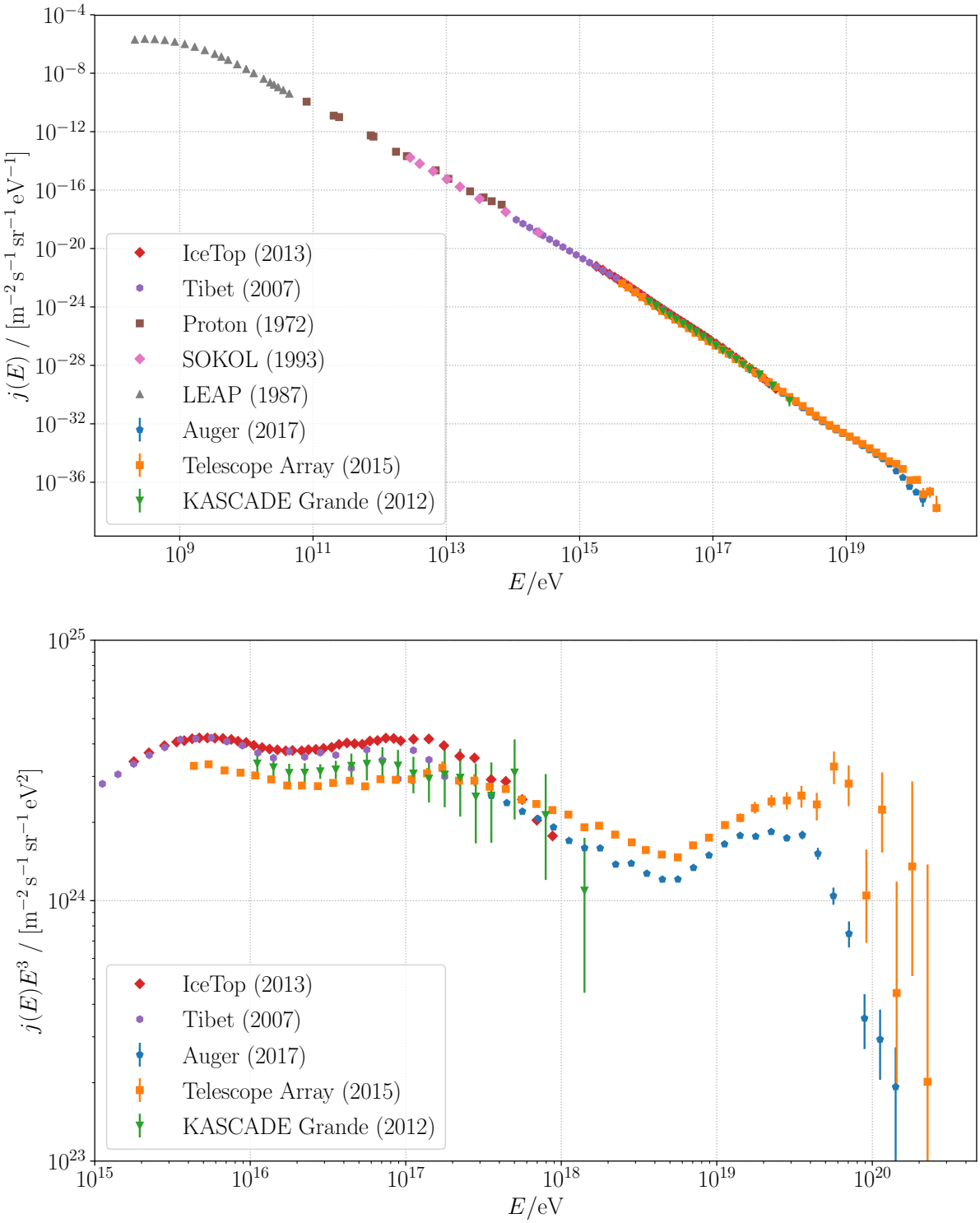

Figure 2.4: The top panel shows the all-particle energy spectrum of cosmic rays measured by various experiments [73, 74, 75, 76, 77, 78]. The bottom panel shows only the highest energy range where the flux is multiplied by E^3 to enhance the visibility of the knee, ankle and cut-off features.

additional characteristics were recently also observed: a flattening around 2×10^{16} eV and a steepening at 1.3×10^{17} eV to $\gamma\sim3.3$ in the so-called second knee feature [76, 85, 86].

2.5.2 Composition

The cosmic ray composition can be precisely determined for energies below 10^{15} eV where the flux is still accessible for direct measurements of primary particles. The composition in that range effectively follows the abundance of elements in the solar system. The only exception are the light elements $3\leq Z\leq5$ and the elements close to iron $21\leq Z\leq25$ [87]. The difference for these few elements can be explained by spallation processes of primary cosmic rays in the galaxy [88]. In this energy range, all nuclei exhibit the same power-law in the energy spectrum.

Above 10^{15} eV the description is not so simple and unambiguous as in the lower energy range since the composition can only be inferred from air showers. The depth of the maximum energy deposit $X_{\max}$, as mentioned in 2.4.1, is the main observable easily accessible to the air shower experiments which are sensitive to the composition of the primary cosmic ray. For example, an iron primary initiates the shower earlier than the proton primary and, thus, the difference between them is $100\,\mathrm{g/cm^2}$. Yet, even in that observable there are significant uncertainties and fluctuations, as the fluctuations from shower to shower are of the order $\sigma_{\mathrm{sh}}(X_{\max})\sim20-60\,\mathrm{g/cm^2}$ and the experimental resolution does not exceed $20\,\mathrm{g/cm^2}$, making the composition identification per event hardly possible. Therefore, the results are obtained only from a statistical inference with the help of Monte Carlo air shower simulation codes such as CORSIKA (COsmic Ray SImulations for KAscade) [89].

KASCADE Grande reported a composition change after the (first) knee towards heavy nuclei [58, 59]. Above 1 EeV, the High Resolution Fly's Eye and TA report the presence of light composition again [90, 91]. PAO reports are consistent with that result before the ankle, but at higher energies, it suggests a mixed composition around the ankle with a tendency to iron when reaching the cut-off region [92, 93]. There are ongoing efforts to resolve the discrepancy between PAO and others [94].

2.5.3 Anisotropies

Back in the early days of cosmic rays, the measurement of their arrival directions presented one of the hardest observables to obtain, which is opposite to the situation in contemporary experiments in which arrival directions can be accurately measured. For example, PAO can determine the angular resolution better than 1° or in the worst case 2.2°, depending on the number of the SD stations triggered by a shower [95]. In spite of that, the vast amount of experimental data on arrival directions for years did not reveal anything significant besides a high level of isotropy. One could say that the terminology in the community changed accordingly – to a notion of deviations from isotropy, i.e., to anisotropies. Recently, due to modern experiments and the increased statistics of detected events that picture has slightly changed, showing signs of anisotropy at various energy ranges and at various angular scales. Nevertheless, the fact that the cosmic ray sky is highly isotropic generally remains.

The arrival directions of cosmic rays can be represented as the sum of Dirac delta functions on the surface of the unit sphere:

$$\Phi(\mathbf{n}) = \frac{\mathrm{d}N(\mathbf{n})}{\mathrm{d}\Omega} = \sum_{i=1}^{N} \delta(\mathbf{n} - \mathbf{n}_i) \tag{2.6}$$

where $\mathbf{n}_i$ are the arrival directions of totally N events. The anisotropy $\Phi(\mathbf{n})$ can be expanded in spherical harmonics (see Appendix A):

$$\Phi(\mathbf{n}) = \sum_{\ell \geq 0} \sum_{m=-\ell}^{\ell} a_{\ell m} Y_{\ell m}(\mathbf{n}) \tag{2.7}$$

where the information about the anisotropy is encoded in the coefficients $a_{\ell m}$ of the expansion. Additionally, the angular power spectrum can be defined as the average squared amplitude of the coefficients:

$$C_\ell = \frac{1}{2\ell + 1} \sum_{m=-\ell}^{\ell} |a_{\ell m}|^2 \tag{2.8}$$

where the moment order of ℓ represents anisotropies of an angular scale $180°/\ell$.

Now, with this definition in mind, experimental results can be divided into two groups: those focused on large-scale anisotropies around $\ell \sim 1$, such as the dipolar or quadrupolar anisotropy, and those focused on small scales anisotropies, like the clustering of events in a certain region of the sky referred to as "hot spots". Ideally, a full-sky observatory is needed to give a true description in terms of C_ℓ [96], but unfortunately, up to now, every experiment covers only a certain part of the sky, which requires reconstruction methods that introduce additional assumptions about correlations between multiple moments. Another issue is that many experiments can only detect variations in the flux as a function of the right ascension (RA), α, but not on the declination, δ, due to uncertain attenuation of showers in the atmosphere, geomagnetic influences on the shower, among others. Combining the data sets, experiments try to overcome these difficulties, as, for example, PAO and TA in [97].

In the $10^{12} - 10^{15}\,\mathrm{eV}$ energy range, experiments such as Tibet-ASγ, Milagro or IceCube/IceTop, report large-scale anisotropies with an amplitude of about 10^{-3} to 10^{-4} [98, 99, 100, 101]. On the other hand, KASCADE showed no significant excesses [102]. The equatorial component, which can be more precisely measured, of a dipolar anisotropy is determined to increase up to $10^{12}\,\mathrm{eV}$ with maximum values of 10^{-3}, and then decreases up to $10^{14}\,\mathrm{eV}$, where it reaches minimum values of 10^{-4}. The direction of the equatorial component of the dipole at $\sim 300 \times 10^{15}\,\mathrm{eV}$ is aligned with the direction of the Galactic centre. For a more detailed review see [103, 104].

In the energy range above $10^{15}\,\mathrm{eV}$, the first solid sign of anisotropy was recently established by PAO at 8 EeV with a five-sigma certainty [105]. That anisotropy is a dipole pointing to $(\alpha, \delta) = (100°, -24°)$ and with an amplitude of about 6.5%. For comparison, the Galactic centre is located in Sagittarius A* [106], at $(266°, -29°)$, which means that the dipole is pointing almost in the opposite direction of the Galactic centre.

At the highest energies of cosmic rays, where the propagation should become more rectilinear, and where small scale anisotropies are expected as a sign of sources, TA and PAO reports the following. The largest departure from isotropy, according to the

PAO analysis [13], is at an energy threshold of 54 EeV in a 12° radius window centred at $(\alpha, \delta) = (198°, -25°)$. This is $\sim 18°$ away from the direction of Centaurus A $(201°, -43°)$ [107], yet the excess is not statistically significant. TA reports the maximum departure from isotropy in a 20° angular radius at $(\alpha, \delta) = (148.5°, 43.2°)$ with a 3.4σ significance. The autocorrelation analysis does not deviate from an isotropic expectation, both for PAO [13] and TA [108]. The only exception is a moderate deviation from isotropy above the 57 EeV threshold at $20° - 30°$ angular scales.

Testing a possible correlation of arrival directions with catalogues of extragalactic objects, such as the 2MRS catalogue [109], the Swift-BAT X-ray catalogue of AGNs [110] and a catalogue of radio galaxies with jets [111] did not yield any significant correlation [13, 112]. PAO recently reported a 4σ deviation from isotropy at an intermediate angular scale for the case of starburst galaxies [78].

It can be suggested that the absence of significant correlations with visible objects implies the important role of Galactic and/or extragalactic magnetic fields on the propagation of cosmic rays.

3 | Charged particles in magnetic fields

In the previous chapter, it was shown how the concept of cosmic rays has developed and been refined through time and how it was necessary that other related fields advance in order to open paths for new ideas and hypotheses. Despite significant advancements, many questions in the research field of cosmic rays persist today, and one could expect that the described process of progress will, in one way or another, continue. An implication of this is that the accumulated knowledge is not a final one and that definitions and premises that are valid now will be unsatisfactory and insufficiently strict in the future. On the other hand, it is hardly possible to build any formally consistent structure on such a fluid ground without stating at least some building blocks as facts. Therefore, to lay the foundations for a theoretical investigation one has to start from a basic set of assumptions which are based on, but not strictly tied up with, the experience, and which have firm relationships to already established physical theories. As Hannes Alfvén put it in his book [113]: "When we try to apply to cosmic phenomena the laws [of physics] in which the experience [gained in the laboratory] is condensed, we make an enormous extrapolation, the legitimacy of which can be checked only by comparing the theoretical results with observations".

The previous introductory paragraph uncovered and announced the task of this chapter. It is to give an overview of the underlying theories and discuss some of the later used assumptions.

Of course, by immersing the subject into the mathematical framework, there is the danger of losing connections with the real world substance of the studied phenomena. On the other hand, the gain is in establishing an overall consistency between different

aspects of the researched phenomenon and related theories, which is a difficult job in its own right, but which could be even more difficult without mathematical tools. Emphasising the limits and assumptions of given derivations could be seen as a safeguard measure against the described danger.

With that said, the first assumption in this research is that cosmic rays are charged particles that traverse the Universe. There is plenty experimental evidence which supports this assumption, although chances that cosmic rays above 10^{15} eV, in the domain of air shower experiments, are neutral persist as an academic possibility as long as the composition of the primary cosmic ray remains directly unseen. By being charged, they primarily interact with electromagnetic fields. Many indications show that the Universe is filled with magnetic fields on all scales. They are highly irregular and are structured following to some extent the matter distribution [114, 115, 116]. The known theoretical framework of electromagnetism founded by Maxwell [4] can be employed to deal with this scenario.

The classical electromagnetic theory of fields is completely described by the set of four equations valid in vacuum [117]:

$$\begin{aligned} \nabla \cdot \mathbf{E} &= \frac{\rho}{\epsilon_0} \\ \nabla \times \mathbf{B} - \frac{\partial \mathbf{E}}{c^2 \partial t} &= \mu_0 \mathbf{j} \\ \nabla \times \mathbf{E} + \frac{\partial \mathbf{B}}{\partial t} &= 0 \\ \nabla \cdot \mathbf{B} &= 0 \end{aligned} \tag{3.1}$$

where $\mathbf{E}$ and $\mathbf{B}$ are, respectively, the electric and magnetic field, and $\mathbf{j}$ and ρ charge and current density.

Another essential equation is the Lorentz force equation which describes the dynamics, i.e., the effect of those fields on a charge q which moves with relativistic velocity $\mathbf{u}$ in them:

$$\frac{\mathrm{d}\mathbf{p}}{\mathrm{d}t} = q(\mathbf{E} + \mathbf{u} \times \mathbf{B}) \ . \tag{3.2}$$

Sometimes it is easier to obtain the result of a problem with the Lagrangian formalism, in which a charged particle in electromagnetic potentials $\mathbf{A}$ and Φ is given by the following Lagrangian [117]:

$$\mathcal{L} = -mc^2/\gamma + \frac{e}{c}\mathbf{u}\cdot\mathbf{A} - q\Phi \ . \tag{3.3}$$

in which m represents the rest mass, and γ is, traditionally, the Lorentz factor $\gamma = 1/\sqrt{1-\frac{u^2}{c^2}}$.

The Hamiltonian $\mathcal{H}$ is also worth to note down. It can be derived by finding the canonical momentum $\mathbf{P}$ from $\mathcal{L}$, which is conjugated with the position coordinate $\mathbf{x}$:

$$P_i = \frac{\partial L}{\partial u_i} = \gamma m u_i + \frac{e}{c}A_i \Rightarrow \mathbf{P} = \gamma m\mathbf{u} + \frac{e}{c}\mathbf{A} = \mathbf{p} + \frac{e}{c}\mathbf{A} \tag{3.4}$$

from which, by a Legendre transformation of $\mathcal{L}$, $\mathcal{H} = \mathbf{P}\cdot\mathbf{u} - \mathcal{L}$, follows the Hamiltonian:

$$\mathcal{H} = c\sqrt{m^2c^2 + \left(\mathbf{P} - \frac{q}{c}\mathbf{A}\right)^2} + q\Phi \ . \tag{3.5}$$

In most cases of interest, the electric component of electromagnetic field in the Universe vanishes due to the high conductivity of the interstellar medium [118, 119], hence, the particle only interacts with the magnetic field. From now on, $\mathbf{E}$ and Φ will be removed from the Lorentz force in all formulations mentioned above.

In a uniform magnetic field, the particle generally exhibits a motion that can be described as gyration perpendicular to the field lines and motion parallel to the field lines. These two form a helix of constant pitch around the magnetic field line. The angle between the particle's velocity vector $\mathbf{u}$ and the local magnetic field line $\mathbf{B}$ is called the pitch angle. Equation (3.2) thus can be rewritten as follows:

$$\frac{\mathrm{d}\mathbf{u}}{\mathrm{d}t} = \mathbf{u}\times\omega_g \tag{3.6}$$

where $\omega_g = \frac{qc\mathbf{B}}{E}$ is the gyration or precession frequency. E is the particle's energy $E = \gamma mc^2$. A quantity also related to the gyration movement is the radius of gyration, $r_g =$

$\frac{|\mathbf{p}|}{|q|B_\perp}$, also called the Larmor radius or the gyroradius. Another convenient parameter here is the magnetic rigidity $\mathcal{R} = |\mathbf{p}c|/q$ since particles with the same magnetic rigidity follow same trajectories in the magnetic field even if they have a different charge number or momentum.

Determining the behaviour of a moving charge even in a static magnetic field can represent a difficult problem, in most cases unsolvable analytically. Nevertheless, before introducing numerical methods, there are several analytical results which are good to investigate to develop intuition in this context.

The first consideration is when a charge gyrates around a slowly varying magnetic field line for which the adiabatic invariants method can be applied as it will be shown in the next section following [120, 117, 79, 121].

3.1 Slowly changing magnetic fields

The concept of adiabatic invariants was introduced in celestial mechanics and in the old quantum theory, and here it can be applied when a charged particle moves through a slowly varying field. To be more concrete, it is required that the magnetic field strength change, $\Delta B/B$, is insignificant during a single orbital period $T = 2\pi/\omega_g$ of a particle, making the action integral invariant:

$$J = \oint \mathbf{P}_\perp \cdot \mathrm{d}\mathbf{l} = \text{const.} \tag{3.7}$$

where $\mathbf{P}_\perp$ is the transverse component of the canonical momentum 3.4 which is parallel to the line element directed along the circular path of a particle $\mathrm{d}\mathbf{l}$. Thus, the action integral yields:

$$\begin{aligned} J &= \oint \mathbf{P}_\perp \cdot \mathrm{d}\mathbf{l} = \oint \mathbf{p}_\perp \cdot \mathrm{d}\mathbf{l} + \frac{e}{c} \oint \mathbf{A} \cdot \mathrm{d}\mathbf{l} \\ &= \oint m u_\perp r_g \mathrm{d}\theta + \frac{e}{c} \int_S \nabla \times \mathbf{A} \cdot \mathrm{d}\mathbf{a} \\ &= 2\pi m r_g^2 \gamma \omega_g + \frac{e}{c} \int_S \mathbf{B} \cdot \hat{\mathbf{n}} \, \mathrm{d}a \end{aligned} \tag{3.8}$$

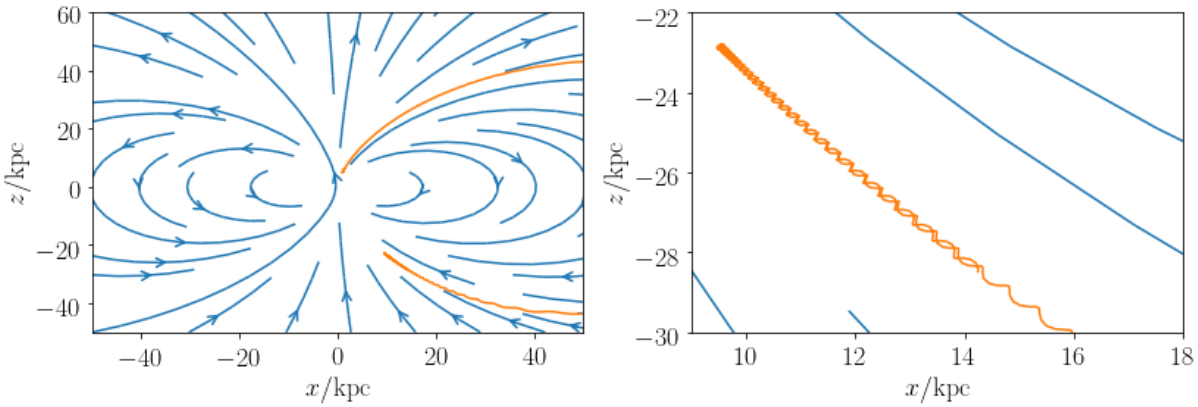

Figure 3.1: The orange line shows the gyration of a particle along a field line, represented in blue, in the magnetic field of a magnetic dipole. After reaching a certain threshold, the particle is bounced as it can be seen clearly on the right panel. The particle is basically trapped in the magnetic field. This scenario has been investigated in studies of the Earth's magnetosphere (see [122] for example). The trajectory shown here is produced with CRPropa (appendix B).

where in the last line the first integral has been integrated over θ just after the substitution $u_\perp = \omega_g \gamma r_g$ has been applied and Stoke's theorem has been employed in the second integral. The variable of integration da is a surface element of the area enclosed by the circular path. The second integral can be solved by observing that the unit vector $\hat{\mathbf{n}}$ is anti-parallel to $\mathbf{B}$, which leaves $-\frac{e}{c} r_g^2 \pi B$. From the definition of $\omega_\mathbf{g}$ the first term is $2\frac{e}{c} r_g^2 \pi B$. After subtracting, the action integral yields

$$J = \frac{e}{c} r_g^2 \pi B \ . \tag{3.9}$$

Therefore, according to the adiabatic invariance of J, $\Delta(\pi r_g^2 B)$ vanishes which means that the flux passing through the particle's orbit is linked with the area of the orbit. Equivalent statements are $B r_g^2 = p_\perp^2 / B = \gamma \mu$, where $\mu = (e \omega_g r_g^2 / 2c)$ is the magnetic moment of the current loop of the particle in orbit. From the last equality, it can be concluded that the magnetic moment is itself an adiabatic invariant in the nonrelativistic limit.

The direct consequence of this result is a phenomenon called the magnetic mirroring. If a particle is spiraling through a static magnetic field $\mathbf{B}$ around the z axis in which there is also a small positive gradient of B, it will bounce at some point $z = z_0$. To show

this, the particle's velocity is decomposed into perpendicular and parallel components to **B**: $v^2 = v_{||}^2 + v_{\perp}^2$. The adiabatic invariant $p_{\perp}^2/B = \text{const.}$ yields:

$$\frac{v_{\perp 0}^2}{B_0} = \frac{v_{\perp}^2}{B} \tag{3.10}$$

where zero indices represent values at $z = 0$. Using this, the relation between the components of the velocity becomes:

$$v_{||}^2 = v_0^2 - v_{\perp 0}^2 \frac{B(z)}{B_0} \ . \tag{3.11}$$

Increasing $B(z)$ will be shrinking the particle's orbit while decreasing the parallel component $v_{||}$ which at some point z_0 will eventually reach zero. At that point it will bounce and continue spiraling in the negative z direction. Figure 3.1 shows a more complex but also more realistic case of magnetic mirroring in the magnetic field of the dipole.

The magnetic mirroring also stands behind a mechanism of the acceleration of cosmic rays developed by E. Fermi [50] as mentioned in sec. 2.4. In Fermi acceleration a charged particle is bouncing, due to the magnetic mirror effect, in a magnetic field between two interstellar clouds if the magnetic field in them is greater than the area in between. When clouds are moving relatively towards each other, the charged particle gains energy on each reflection. Now it is clear why the particle has to have an initial velocity. Otherwise, it cannot be trapped, and the acceleration mechanism does not work. A more detailed description can be found, for example, in [10, 88].

3.2 Scattering in magnetic fields

Magnetic fields in the Universe at all scales are expected to contain irregularities which have a profound effect on a moving charge. In the case of interplanetary magnetic fields these irregularities were directly measured, for example, by the Mariner 4 spacecraft (see [123] for more). Magnetic fields of larger scales, galactic and extra-galactic, are also assumed to contain irregularities [115, 114]. A charged particle is scattered

when it encounters those irregularities, and that can change the field line around which it gyrates. The effectiveness of the scattering depends on the size of the irregularity compared to the particle's gyroradius. If the irregularity is much bigger than the gyroradius, the particle follows the field line of the irregularity conserving its adiabatic invariants. On the other hand, if irregularities are too small compared to the gyroradius, the particle continues to gyrate along the mean magnetic field line like in the case when irregularities are not present. Thus, only irregularities of comparable size to the gyroradius significantly scatter the particle.

Accumulation of scatterings eventually leads to a stochastic motion where the particle inevitably "forgets" its original pitch angle, thus two states of the particle separated enough become completely uncorrelated. That can be described by a Wiener process, i.e., Brownian motion [124, 125]. A basic question which determines the nature of scattering is what does it mean "separated enough". It turns out that this depends on the details of the system, i.e., the particle properties and magnetic field characteristics.

Without knowing details of a scattering process, movement of a charged particle can be roughly classified purely statistically, by observing its mean square displacement. The mean square displacement is defined as:

$$\left\langle (\Delta r)^2 \right\rangle \equiv \left\langle (r(t) - r(0))^2 \right\rangle \ . \tag{3.12}$$

The mean square displacement is a continuous function of time, which can be assumed to have a form of

$$\left\langle (\Delta r)^2 \right\rangle \sim t^{\sigma} \ . \tag{3.13}$$

A different type of motion is represented by a different regime of the parameter σ,

namely [126]:

$$\begin{aligned} \text{subdiffusion}: &\quad 0 < \sigma < 1 \ , \\ \text{normal diffusion}: &\quad \sigma = 1 \ , \\ \text{superdiffusion}: &\quad 1 < \sigma < 2 \ , \\ \text{rectilinear propagation}: &\quad \sigma = 2 \ . \end{aligned} \tag{3.14}$$

The rectilinear propagation represents a motion without any deflections, the normal diffusion is actually a Brownian movement, while sub- and superdiffusion are regimes known as anomalous diffusion.

To continue further with the analysis one has to know more about the nature of irregularities in magnetic fields where the scattering takes place. The most commonly considered case of an irregular magnetic field in this area of research is a turbulent magnetic field, therefore, a short review is needed, first about magnetohydrodynamics and then followed by details of turbulent magnetic field modelling.

3.3 Magnetohydrodynamics

The plasma state, which implies high conductivity, is the dominating state of matter in the Universe. Electrical currents there, which occur due to the movement of charges in the plasma, induce magnetic fields. In that setting turbulent magnetic fields arise. The theoretical realm where the plasma and magnetic fields are investigated is called magnetohydrodynamics (abbreviated as MHD). But before immersing into it, a few remarks are needed on regular hydrodynamics.

Within the hypothesis of continuum, it is believed that all fluid flows are described by the Navier-Stokes equations which relate the fluid density field $\rho(\mathbf{x}, t)$ and its velocity

field $\mathbf{u}(\mathbf{x}, t)$ [127]:

$$\left(\frac{\partial}{\partial t} + \mathbf{u} \cdot \nabla\right) \rho = -\rho \nabla \cdot \mathbf{u} \ ,$$
$$\rho \left(\frac{\partial}{\partial t} + \mathbf{u} \cdot \nabla\right) \mathbf{u} = -\nabla p + \mu \nabla^2 \mathbf{u} + \mathbf{f} \ . \tag{3.15}$$

The first equation is the mass-conservation equation where the bracket represents the Lagrangian (material) derivative, while the second one is the momentum equation where the right-hand side contains the force terms: $-\nabla p$ is the gradient of the local fluid pressure $p(\mathbf{x}, t)$, $\mu \nabla^2 \mathbf{u}$ is the net force associated with internal friction or viscosity μ, and $\mathbf{f}(\mathbf{x}, t)$ is any external force per unit mass acting on the fluid.

The Navier-stokes equations, besides the laminar class of flows, also describe highly irregular flow patterns called turbulence (for an introduction see [128]). First systematic studies of this phenomenon were conducted by O. Reynolds [129]. One of his observations is that the turbulence phase can be characterized by the relative importance of the inertial and viscous forces, that is, by a quantity later named after him, the Reynolds number:

$$Re = \frac{\rho u L}{\mu} = \frac{u L}{\nu} \tag{3.16}$$

where L is the characteristic dimension of a system under consideration, and the fluid is described by its density ρ, velocity u, and the dynamic and kinematic viscosity, μ and ν, respectively. The turbulent regime is reached when the Reynolds number is high, roughly above 1000.

After Reynolds, the phenomenon of turbulence was studied by many scholars, including N. Kolmogorov [130, 131, 132, 133] (also see [134, 135]). He developed a theory based on a statistical approach and derived the following. He used the assumption that the phenomenon of turbulence has the property of transferring energy from larger eddies to smaller eddies which are independent of scale which expands within a certain range. The upper boundary of this range is defined by the scale at which the system receives the energy, while the lower boundary is the one at which the energy dissipates due to viscosity. That assumption of scale invariance, called the scale universality, is confirmed

by many experimental tests (for an overview see [136]), but there are also indications of scale dependent features like intermittency [137].

Although Kolmogorov used complex mathematical arguments, the same result can be sketched by a dimensional argument. From the universality assumption follows that the energy dissipation rate ϵ is constant:

$$\epsilon \sim \frac{\Delta\rho_\ell}{\Delta t} \tag{3.17}$$

where $\Delta\rho_\ell$ is the change of energy density of scale ℓ transfer in time Δt. The change of energy density is proportional to the kinetic energy $\Delta\rho_\ell \sim v_\ell^2$, while $\Delta t = \ell/v_\ell$. That yields

$$\epsilon \sim \frac{\Delta\rho_\ell^{3/2}}{\ell} = \text{const.} \Rightarrow \Delta\rho_\ell \propto \ell^{2/3} \ . \tag{3.18}$$

It is convenient to transform this into an inverse Fourier space of v_ℓ where $k \propto 1/\ell$:

$$\mathbf{v}(\mathbf{k}, t) = \frac{1}{(2\pi)^3} \iiint_{\mathbb{R}^3} \mathbf{v}(\mathbf{x}, t) \mathrm{e}^{\mathrm{i}\mathbf{x}\cdot\mathbf{k}} \mathrm{d}^3\mathbf{x} \tag{3.19}$$

so that $\Delta\rho_\ell(v_\ell) \to \Delta\rho_k(v_k)$ which finally gives:

$$\Delta\rho_k \sim k^{-2/3} \Rightarrow E(k) \equiv \frac{\mathrm{d}\Delta\rho_k}{\mathrm{d}k} \sim k^{-5/3} \ . \tag{3.20}$$

The study of turbulence can be generalized to the magnetohydrodynamical case [138] where the Navier-Stokes equations (3.15) are combined with Maxwell's equations (3.1) in the following way.

In Ohm's law for the plasma

$$\mathbf{j} = \sigma(\mathbf{E} + \mathbf{u} \times \mathbf{B}) \tag{3.21}$$

where σ is conductivity, the second and the third Maxwell's equations are employed without the displacement current term since the plasma is too slow compared to the

speed of light to be relevant in this case:

$$\begin{aligned}\nabla \times \mathbf{B} &= \mu_0\sigma(\mathbf{E} + \mathbf{u} \times \mathbf{B}) \\ \nabla \times \nabla \times \mathbf{B} &= \mu_0\sigma\left[\nabla \times \mathbf{E} + \nabla \times (\mathbf{u} \times \mathbf{B})\right] \\ -\nabla^2\mathbf{B} &= \mu_0\sigma\left[\nabla \times (\mathbf{u} \times \mathbf{B}) - \frac{\partial \mathbf{B}}{\partial t}\right] .\end{aligned} \tag{3.22}$$

In the last line the vector identity

$$\nabla \times (\nabla \times \mathbf{B}) = \nabla(\nabla \cdot \mathbf{B}) - \nabla^2\mathbf{B} \tag{3.23}$$

has been used. This gives the induction equation:

$$\frac{\partial \mathbf{B}}{\partial t} = \nabla \times (\mathbf{u} \times \mathbf{B}) + \eta\nabla^2\mathbf{B} \tag{3.24}$$

where $\eta = 1/\mu_0\sigma$. The first term on the right-hand side is known as the convective term responsible for "freezing" magnetic field lines in the plasma. The second term is called diffusive and shows the resistive leakage of the magnetic field lines across the plasma [121]. The induction equation can be rewritten in a more "hydrodynamical" form[1]:

$$\left(\frac{\partial}{\partial t} + \mathbf{u} \cdot \nabla\right)\mathbf{B} = (\mathbf{B} \cdot \nabla)\,\mathbf{u} - \mathbf{B}\,(\nabla \cdot \mathbf{u}) + \eta\nabla^2\mathbf{B} \; . \tag{3.26}$$

In the second equation of (3.15), the force term $\mathbf{j} \times \mathbf{B} = (\nabla \times \mathbf{B}) \times \mathbf{B}/\mu_0$ is added:

$$\left(\frac{\partial}{\partial t} + \mathbf{u} \cdot \nabla\right)\mathbf{u} = -\frac{1}{\rho}\nabla p + \frac{\mu}{\rho}\nabla^2\mathbf{u} + \frac{1}{\rho}\mathbf{f} + \frac{1}{\rho\mu_0}\,(\nabla \times \mathbf{B}) \times \mathbf{B} \; . \tag{3.27}$$

The following identity

$$(\nabla \times \mathbf{B}) \times \mathbf{B} = (\mathbf{B} \cdot \nabla)\,\mathbf{B} - \nabla\left(\frac{B^2}{2}\right) \; , \tag{3.28}$$

[1]By exploiting the following identity:

$$\nabla \times (\mathbf{u} \times \mathbf{B}) = \mathbf{u}\,(\nabla \cdot \mathbf{B}) - \mathbf{B}\,(\nabla \cdot \mathbf{u}) + (\mathbf{B} \cdot \nabla)\,\mathbf{u} - (\mathbf{u} \cdot \nabla)\,\mathbf{B} \; . \tag{3.25}$$

and the incompressibility condition $\nabla \cdot \mathbf{u} = 0$ in eq. (3.26) and eq. (3.27) yield the set of equations:

$$\begin{aligned}
\left(\frac{\partial}{\partial t} + \mathbf{u}\cdot\nabla\right)\mathbf{B} &= (\mathbf{B}\cdot\nabla)\,\mathbf{u} + \eta\nabla^2\mathbf{B}\ , \\
\left(\frac{\partial}{\partial t} + \mathbf{u}\cdot\nabla\right)\mathbf{u} &= -\frac{1}{\rho}\nabla\left(p - \frac{B^2}{2\mu_0}\right) + \frac{\mu}{\rho}\nabla^2\mathbf{u} + \frac{1}{\rho}\mathbf{f} + \frac{1}{\rho\mu_0}(\mathbf{B}\cdot\nabla)\,\mathbf{B}\ , \\
\nabla\cdot\mathbf{u} &= 0\ , \\
\nabla\cdot\mathbf{B} &= 0
\end{aligned} \tag{3.29}$$

which describe the incompressible MHD theory.

3.3.1 Turbulent magnetic fields

The incompressible MHD theory can be applied to the interstellar plasma to develop a theory of interstellar turbulence of magnetic fields by investigating the dynamics of the Alfvén waves in the cosmic plasma [113, 139, 140, 141]. However, here a phenomenological approach will be followed referring to some parts of the theoretical results.

Here only a magnetic turbulent field $\delta\mathbf{B}(\mathbf{x}, t)$ with homogeneous statistical properties is considered following references [142, 126]. The magnetic field can be given in the wavenumber space for the ith component ($i = x, y, z$):

$$\delta B_i(\mathbf{x}, t) = \int \frac{\mathrm{d}^3k}{(2\pi)^3}\delta B_i(\mathbf{k}, t)\mathrm{e}^{\mathrm{i}\mathbf{k}\cdot\mathbf{x}}\ . \tag{3.30}$$

For studies of charged particle transport, the two-point-two-time correlation tensor takes an important role:

$$\langle\delta B_i(\mathbf{x}, t)\delta B_j(\mathbf{x}_0, t_0)\rangle = (2\pi)^{-6}\int \mathrm{d}^3k \int \mathrm{d}^3k'\,\langle\delta B_i(\mathbf{k}, t)\delta B_j(\mathbf{k}', t_0)\rangle\,\mathrm{e}^{\mathrm{i}\mathbf{k}\cdot\mathbf{x}+\mathrm{i}\mathbf{k}'\cdot\mathbf{x}_0}\ . \tag{3.31}$$

With $\Delta t_0 = 0$ and $\mathbf{x_0} = 0$ in the previous equation, the homogeneity condition defines:

$$\langle\delta B_i(\mathbf{k}, t)\delta B_j(\mathbf{k}', 0)\rangle = (2\pi)^6 P_{ij}(\mathbf{k}, t)\delta(\mathbf{k} + \mathbf{k}') \tag{3.32}$$

where $P_{ij}(\mathbf{k},t)$ is the correlation tensor in the wavenumber space. Further on, by assuming the same temporal behaviour of all tensor components, the magnetostatic correlation tensor $P_{ij}(\mathbf{k}) \equiv P_{ij}(\mathbf{k},0)$ and the dynamical correlation function $\Gamma(\mathbf{k},t)$ can be separated:

$$P_{ij}(\mathbf{k},t,t_0) = P_{ij}(\mathbf{k})\Gamma(\mathbf{k},t) \ . \tag{3.33}$$

The focus will be given on isotropic turbulence which prescribes the following form for the magnetostatic correlation tensor in the most general way [142]:

$$P_{ij}(\mathbf{k}) = A(k)\delta_{ij} + B(k)k_ik_j + C(k)\sum_n \epsilon_{ijn}k_n \ . \tag{3.34}$$

where $B(k)$ has nothing to do with the magnetic field which is denoted either as the vector quantity $\mathbf{B}$ or per component B_i. The same notation will be used to be consistent with the literature, but only in the next few paragraphs. Maxwell's equations (3.1) require the solenoidal constraint:

$$\sum_i \partial_i \delta B_i(\mathbf{x}) = 0 \Rightarrow \sum_i k_i \delta B_i(\mathbf{k}) = 0 \tag{3.35}$$

which by using eq. (3.32) results

$$\sum_{ij} \langle k_i \delta B_i(\mathbf{k}) k_j \delta B_j(\mathbf{k}')\rangle = \sum_{ij} k_i k_j P_{ij}(\mathbf{k}) = 0 \ . \tag{3.36}$$

Inserting eq. (3.34) into the last equation fixes the relationship between $B(k)$ and $A(k)$:

$$B(k) = -\frac{A(k)}{k^2} \tag{3.37}$$

and, therefore, it reduces the original expression to:

$$P_{ij}(\mathbf{k}) = A(k)\left(\delta_{ij} - \frac{k_ik_j}{k^2}\right) + C(k)\sum_n \epsilon_{ijn}k_n \ . \tag{3.38}$$

Additionally, the magnetostatic correlation tensor also has to satisfy the following:

$$P_{ij}(\mathbf{k}) = \left\langle \delta B_i \delta B_j^* \right\rangle = \langle \delta B_i^* \delta B_j \rangle^* = \langle \delta B_j \delta B_i^* \rangle^* = P_{ji}^*(\mathbf{k}) \tag{3.39}$$

which puts additional constraints on the coefficients, namely:

$$A(k) = A(k)^* \qquad \text{and} \qquad C(k) = -C(k)^* \tag{3.40}$$

or by words: $A(k)$ has to be real and $C(k)$ has to be imaginary. It is customary to redefine

$$C(k) = \mathrm{i}A(k)\frac{\sigma(k)}{k} \tag{3.41}$$

without loosing generality where $\sigma(k)$ is a real number called the magnetic helicity. Finally, the magnetostatic correlation tensor reads:

$$P_{ij}(\mathbf{k}) = A(k)\left[\delta_{ij} - \frac{k_i k_j}{k^2} + \mathrm{i}\sigma(k)\sum_n \epsilon_{ijn}\frac{k_n}{k}\right] . \tag{3.42}$$

The functions $A(k)$ and $\sigma(k)$ are specified by the turbulence model, where $A(k)$ is usually referred as the geometry.

Continuing the derivation, the emphasis will be on the magnetostatic turbulence without helicity as one of the most widely studied and numerically accessible models. That means that $\Gamma = 1$ in eq. (3.33) and $\sigma(k) = 0$. Following [143] and [141], $A(k)$ is given by:

$$A(k) = \frac{\mathbf{B}^2(k)}{8\pi k^2} \tag{3.43}$$

that can be normalised by requiring

$$B_{\mathrm{rms}}^2 = \int_0^\infty \mathrm{d}k \mathbf{B}^2(k) . \tag{3.44}$$

At this point a Kolmogorov type power law can be used to describe $\mathbf{B}^2(k)$. This is well-founded since the power law dependence has also been observed in experiments, for example by the Helios 2 spacecraft (see [126]). Thus, by assuming $\mathbf{B}^2(k) \propto k^{-n}$ and

normalising eq. (3.44), one obtains:

$$\mathbf{B}^2(k) = B_{\mathrm{rms}}^2(n-1)k^{-n}\frac{1}{k_{\mathrm{min}}^{1-n} - k_{\mathrm{max}}^{1-n}} \tag{3.45}$$

where n is a spectral index, k_{min} and k_{max} have been introduced as integration boundaries which correspond to physical dimensions $2\pi/L_{\mathrm{max}}$ and $2\pi/L_{\mathrm{max}}$, respectively. Alternatively, the same equation can be expressed without referring to k_{min}, k_{max}:

$$\mathbf{B}^2(k) = B_{\mathrm{rms}}^2 k^{-n}(n-1)\frac{\left(\frac{2\pi}{L_{\mathrm{max}}}\right)^{n-1}}{1-\left(\frac{L_{\mathrm{min}}}{L_{\mathrm{max}}}\right)^{n-1}} \tag{3.46}$$

The Kolmogorov spectrum 5/3 is recovered when $n = 5/3$ is plugged in.

The coherence length is a characteristic length scale for the spatial decorrelation of the turbulence and it is an important parameter to characterise the turbulent field. It is defined so that the area of $L_c B_{\mathrm{rms}}^2$ is equal to the total area under the correlation function [126]:

$$L_c \equiv \frac{1}{B_{\mathrm{rms}}^2}\int_{-\infty}^{\infty} \mathrm{d}L\, \langle \delta\mathbf{B}(0)\delta\mathbf{B}(\mathbf{x}(L))\rangle \tag{3.47}$$

where the integration goes along the path $\mathbf{x}(l)$ in a fixed direction. It can be evaluated as follows:

$$\begin{aligned}
L_c &\overset{(3.31)}{=} \frac{1}{B_{\mathrm{rms}}^2}\int_{-\infty}^{\infty}\mathrm{d}L\frac{1}{(2\pi)^6}\sum_i^3\sum_j^3\int\mathrm{d}^3k\int\mathrm{d}^3k'\,\langle\delta B_i(\mathbf{k})\delta B_j(\mathbf{k}')\rangle\,\mathrm{e}^{\mathrm{i}\mathbf{k}\cdot\mathbf{x}(L)}\\
&\overset{(3.32)}{=} \frac{1}{B_{\mathrm{rms}}^2}\int_{-\infty}^{\infty}\mathrm{d}L\sum_i^3\sum_j^3\int\mathrm{d}^3k\int\mathrm{d}^3k'\frac{\mathbf{B}^2(k)}{8\pi k^2}P_{ij}(\mathbf{k},t)\delta(\mathbf{k}+\mathbf{k}')\mathrm{e}^{\mathrm{i}\mathbf{k}\cdot\mathbf{x}(L)}\\
&\overset{(3.42)}{=} \frac{1}{B_{\mathrm{rms}}^2}\int_{-\infty}^{\infty}\mathrm{d}L\int\mathrm{d}^3k\frac{\mathbf{B}^2(k)}{8\pi k^2}\sum_i^3\sum_j^3\left[\delta_{ij}-\frac{k_ik_j}{k^2}\right]\mathrm{e}^{\mathrm{i}\mathbf{k}\cdot\mathbf{x}(L)}\\
&= \frac{1}{B_{\mathrm{rms}}^2}\int_{-\infty}^{\infty}\mathrm{d}L\int\mathrm{d}^3k\frac{\mathbf{B}^2(k)}{8\pi k^2}\sum_i^3\left[\delta_{ii}-\frac{k_ik_i}{k^2}\right]\mathrm{e}^{\mathrm{i}\mathbf{k}\cdot\mathbf{x}(L)}\\
&= \frac{1}{B_{\mathrm{rms}}^2}\int_{-\infty}^{\infty}\mathrm{d}L\int_0^{\infty}\mathrm{d}k k^2\int_0^{2\pi}\mathrm{d}\phi\int_{-1}^{1}\mathrm{d}\cos(\theta)\,\frac{\mathbf{B}^2(k)}{8\pi k^2}2\mathrm{e}^{\mathrm{i}kx(L)\cos(\theta)}\\
&= \frac{1}{B_{\mathrm{rms}}^2}\int_0^{\infty}\mathrm{d}k\int_{-\infty}^{\infty}\mathrm{d}L\mathbf{B}^2(k)\frac{1}{kx(L)}\sin(kx(L))
\end{aligned} \tag{3.48}$$

by employing Cauchy's residue theorem for the inner integral, the equation reads:

$$L_c = \frac{\pi}{B_{\rm rms}^2}\int_0^\infty \mathrm{d}k \frac{\mathbf{B}^2(k)}{k} \overset{(3.46)}{=} \pi(n-1)\frac{\left(\frac{2\pi}{L_{\rm max}}\right)^{n-1}}{1-\left(\frac{L_{\rm min}}{L_{\rm max}}\right)^{n-1}}\int_{k_{\rm min}}^{k_{\rm max}} \mathrm{d}k k^{-n-1} \tag{3.49}$$

this finally results in:

$$L_c = \frac{1}{2}L_{\rm max}\cdot\frac{n-1}{n}\cdot\frac{1-\left(\frac{L_{\rm min}}{L_{\rm max}}\right)^{n}}{1-\left(\frac{L_{\rm min}}{L_{\rm max}}\right)^{n-1}}\ . \tag{3.50}$$

This equation gives, for a Kolmogorov-type spectrum $n = 5/3$, approximate values $L_c \approx L_{\rm max}/2$ when $L_{\rm min} \sim L_{\rm max}$ and $L_c \approx L_{\rm max}/5$ when $L_{\rm min} \ll L_{\rm max}$.

3.4 Propagation in turbulent magnetic fields

Now the stage is ready to investigate scatterings of charged particles when they traverse turbulent magnetic fields. There are several different approaches to this topic. Historically, the problem of transport of cosmic rays in irregular magnetic fields was modelled by the Fokker-Planck equation (see [144] for one of the first papers, or book [141] for a comprehensive overview). The Fokker-Planck equation is a type of master equation that deterministically describes the time evolution of the distribution function $f(\mathbf{r}, \mathbf{v})$ starting from a given initial distribution. It can be seen as a generalization of Liouville's theorem which includes Brownian motion. Accordingly, its solution is an ensemble-averaged particle distribution function. Yet, the distribution function approach can represent a difficulty when dealing with the dynamics of a single particle, especially if the particle has not reached a diffusive behaviour [145]. A different route will be taken here, after [143], by using stochastic differential equations (SDE) (see [124, 146]). This route has an advantage compared to the Fokker-Planck formalism when confronted with an interpretation of a single particle case in a non-diffusive regime since results of SDE are expressed as averaged values of physical quantities, and not as distribution

functions.

To simplify the analysis, the presented derivations and equations are restricted to a relativistic particle where the particle's velocity can be approximated with the speed of light, i.e., $u \approx c$. The justification for this depends on the context, but in most cases for particles above $10^{15}\,\mathrm{eV}$ the approximation is almost always acceptable. It can be checked by evaluating:

$$\frac{u}{c} = \sqrt{1 - \frac{(mc^2)^2}{E^2}} \tag{3.51}$$

where E is energy and m is the mass of the particle.

The unit vector of the velocity, i.e., the direction in which the particle is currently heading, $\hat{\mathbf{n}} = (n_1, n_2, n_3)$, will be the main parameter which depends on the deflection by a turbulent quasi-static magnetic field $\mathbf{B}$:

$$(3.6) \Rightarrow u\frac{\mathrm{d}\hat{\mathbf{n}}}{\mathrm{d}s}\frac{\mathrm{d}s}{\mathrm{d}t} = \left(\frac{qc}{E}\right) u\hat{\mathbf{n}} \times \mathbf{B} \Rightarrow \frac{\mathrm{d}\hat{\mathbf{n}}}{\mathrm{d}s} = \left(\frac{q}{E}\right) \hat{\mathbf{n}} \times \mathbf{B}\ , \quad \frac{\mathrm{d}n_i}{\mathrm{d}s} = \left(\frac{q}{E}\right) \epsilon_{ijk} n_j B_k \tag{3.52}$$

which is just a rewritten version of the Lorentz force equation (3.6) for ultra-relativistic particles $u \approx c \Rightarrow s \equiv ct$. The quantity s denotes the path length which the particle traverses. The particle performs Brownian motion in the flight direction $\hat{\mathbf{n}}$ with a corresponding diffusion coefficient $\mathcal{D}_0$. This can be modelled with the stochastic differential equation of the Ito form [146]:

$$\mathrm{d}n_i = -2\mathcal{D}_0 n_i \mathrm{d}s + \sqrt{2\mathcal{D}_0}\,(\delta_{ij} - n_i n_j)\,dW_j \tag{3.53}$$

where the implicit summation convention is used. With the quantity $\mathrm{d}\mathbf{W} \equiv (\mathrm{d}W_1, \mathrm{d}W_2, \mathrm{d}W_3)$ the Wiener process in three dimensions is set. It satisfies $\langle \mathrm{d}W_i \rangle = 0$ and $\langle \mathrm{d}W_i \mathrm{d}W_j \rangle = \delta_{ij}\mathrm{d}s$. The first term in eq. (3.53) reflects 'dynamical friction', while the second one is due to random deflections in the plane perpendicular to $\hat{\mathbf{n}}$.

First, the averaged deflection angle can be derived:

$$\begin{aligned} &\frac{\mathrm{d}\langle n_i(s)\rangle}{\mathrm{d}s} = -2\mathcal{D}_0\langle n_i(s)\rangle \\ &\Rightarrow \langle n_i(s)\rangle = \langle n_i\rangle_0 \mathrm{e}^{-2\mathcal{D}_0 s} \Rightarrow \langle \hat{\mathbf{n}}(s)\rangle = \langle \hat{\mathbf{n}}\rangle_0 \mathrm{e}^{-2\mathcal{D}_0 s} \end{aligned} \tag{3.54}$$

which shows in case of $s \to \infty$ the particle completely forgets its original direction of flight. The subscript 0 denotes initial values at $s = 0$.

The next task is to employ eq. (3.53) to calculate the evolution of $\langle n_i n_j\rangle$ during propagation. In the case of two stochastic integrals X and Y, the following relation applies [147]:

$$\mathrm{d}(X \cdot Y) = \mathrm{d}X \cdot Y + X \cdot \mathrm{d}Y + \mathrm{d}X \cdot \mathrm{d}Y \tag{3.55}$$

from which $\mathrm{d}(n_i n_j)$ yields:

$$\begin{aligned} \mathrm{d}(n_i n_j) =& \mathrm{d}n_i \cdot n_j + n_i \cdot \mathrm{d}n_j + \mathrm{d}n_i \cdot \mathrm{d}n_j \\ =& \left(-2\mathcal{D}_0 n_i \mathrm{d}s + \sqrt{2\mathcal{D}_0}\left(\delta_{ik} - n_i n_k\right) dW_k\right) \cdot n_j \\ &+ n_i \cdot \left(-2\mathcal{D}_0 n_j \mathrm{d}s + \sqrt{2\mathcal{D}_0}\left(\delta_{jk} - n_j n_k\right) dW_k\right) \\ &+ \left(-2\mathcal{D}_0 n_i \mathrm{d}s + \sqrt{2\mathcal{D}_0}\left(\delta_{ik} - n_i n_k\right) dW_k\right) \cdot \left(-2\mathcal{D}_0 n_j \mathrm{d}s + \sqrt{2\mathcal{D}_0}\left(\delta_{jk} - n_j n_k\right) dW_k\right) \\ =& 2\mathcal{D}_0(\delta_{ij} - 3n_i n_j)\mathrm{d}s \\ &+ \sqrt{2\mathcal{D}_0}\left[n_i\left(\delta_{ik} - n_i n_k\right)\mathrm{d}W_k + n_j\left(\delta_{jk} - n_j n_k\right)\mathrm{d}W_k\right] \end{aligned} \tag{3.56}$$

where the properties $(\mathrm{d}s)^2 = 0$, $\mathrm{d}W_i \mathrm{d}s = \mathrm{d}s\mathrm{d}W_i = 0$, $\mathrm{d}W_i \mathrm{d}W_j = \delta_{ij}\mathrm{d}s$ were used. By taking the average, only the first term on the right-hand side is left:

$$\mathrm{d}\langle n_i n_j\rangle = 2\mathcal{D}_0(\delta_{ij} - 3\langle n_i n_j\rangle)\mathrm{d}s \Rightarrow \frac{\mathrm{d}\langle n_i n_j\rangle}{\mathrm{d}s} = 2\mathcal{D}_0(\delta_{ij} - 3\langle n_i n_j\rangle)\ . \tag{3.57}$$

The result of integration is:

$$\langle n_i n_j\rangle = \langle n_i n_j\rangle_0 \mathrm{e}^{-6\mathcal{D}_0 s} + \frac{\delta_{ij}}{3}\left(1 - \mathrm{e}^{-6\mathcal{D}_0 s}\right)\ . \tag{3.58}$$

By following the path of propagation $x_i(s) = \int_0^s \mathrm{d}s' n_i(s')$ along the coordinate axes and averaging it, one gets:

$$\langle x_i(s)\rangle = \frac{\langle n_i\rangle_0}{2\mathcal{D}_0}\left(1 - \mathrm{e}^{-2\mathcal{D}_0 s}\right) \ . \tag{3.59}$$

One should be cautious when interpreting this result. By construction of the integral, the path is already assumed to be along an axis so the equation can only describe the ballistic regime of propagation which in limit $\mathcal{D}_0 s \ll 1$ becomes $\langle x_i(s)\rangle \approx \langle n_i\rangle s$, i.e., that the particle follows a straight line. In the diffusive regime, the under integral function is already zero and there is no path to follow along an axis, thus the integration yields $\langle x_i\rangle = 0$ which is a well-known result of Brownian motion.

Finally, two additional relations used later are also derived (see [143] for the full derivations). The correlation between the particle's flight direction and position:

$$\begin{aligned}\frac{\mathrm{d}\langle x_i n_j\rangle}{\mathrm{d}s} &= \langle n_i n_j\rangle - 2\mathcal{D}_0\langle x_i n_j\rangle \Rightarrow \\ \langle x_i n_j\rangle &= \frac{\langle n_i n_j\rangle_0 - \frac{1}{3}\delta_{ij}}{4\mathcal{D}_0}\mathrm{e}^{-2\mathcal{D}_0 s}\left(1 - \mathrm{e}^{-4\mathcal{D}_0 s}\right) + \frac{\delta_{ij}}{6\mathcal{D}_0}\left(1 - \mathrm{e}^{-2\mathcal{D}_0 s}\right) \ .\end{aligned} \tag{3.60}$$

That was necessary to calculate the correlation between two positions:

$$\begin{aligned}\frac{\mathrm{d}\langle x_i x_j\rangle}{\mathrm{d}s} =& 2\langle x_i n_j\rangle \Rightarrow \\ \langle x_i x_j\rangle =& \frac{1}{4\mathcal{D}_0^2}\left(\langle n_i n_j\rangle_0 - \frac{1}{3}\delta_{ij}\right)\left[1 - \mathrm{e}^{-2s\mathcal{D}_0} - \frac{1}{3}\left(1 - \mathrm{e}^{-6s\mathcal{D}_0}\right)\right] \\ &+ \frac{\delta_{ij}}{3\mathcal{D}_0}\left[s - \frac{1}{2\mathcal{D}_0}\left(1 - \mathrm{e}^{-2s\mathcal{D}_0}\right)\right] \ .\end{aligned} \tag{3.61}$$

After lengthy work to obtain these expressions, some concrete results may follow.

3.4.1 Quasi-rectilinear propagation

In the limit of small angle scatterings, i.e., in the *quasi-linear approximation* [148, 126, 141], where $\mathcal{D}_0 s \ll 1$, one can find the average (root mean square) deflection angle θ_{rms}, a quantity which will be used later when the so-called quasi-rectilinear (or ballistic)

propagation will be analysed.

If the particle is deflected by a small angle θ in its direction of flight $\hat{\mathbf{n}}$, for example, along the z-direction $\hat{\mathbf{e}}_z$, it can be approximated by:

$$\cos(\theta) \approx 1 - \frac{1}{2}\theta^2 \Rightarrow \theta^2 \approx 2\left[1 - \cos(\theta)\right] = 2\left(1 - \hat{\mathbf{n}} \cdot \hat{\mathbf{e}}_z\right) \ . \tag{3.62}$$

Averaging the expression and plugging in $\langle n_z \rangle$ from eq. (3.54) the following result is derived:

$$\langle \theta^2 \rangle \approx 2\left(1 - \langle n_z \rangle\right) = 4\mathcal{D}_0 s \tag{3.63}$$

where in the last step the small angle approximation $\mathcal{D}_0 s \ll 1$ ensures that $\langle n_z \rangle = \mathrm{e}^{-2\mathcal{D}_0 s} \approx 1 - 2\mathcal{D}_0 s$.

In analogy to a spatial diffusion coefficient $\mathcal{K}_{xx} = \lim_{t\to\infty}\langle(\Delta x)^2\rangle/2t$, and by following the Taylor-Green-Kubo formulation of the diffusion coefficient [126]:

$$\mathcal{K}_{xx} = \int_0^\infty \mathrm{d}t \left\langle \frac{\mathrm{d}x}{\mathrm{d}t}(t)\frac{\mathrm{d}x}{\mathrm{d}t}(0)\right\rangle \ , \tag{3.64}$$

the diffusion coefficient in the flight direction takes the form:

$$\mathcal{D}_{ij} \equiv \lim_{\Delta s\to\infty} \frac{\langle \Delta n_i \Delta n_j\rangle}{2\Delta s} = \int_0^\infty \mathrm{d}s \left\langle \frac{\mathrm{d}n_i}{\mathrm{d}s}(0)\frac{\mathrm{d}n_j}{\mathrm{d}s}(s)\right\rangle \tag{3.65}$$

where $\Delta n_i \equiv n_i - \langle n_i\rangle$ and, therefore, $\langle \Delta n_i \Delta n_j\rangle = \langle n_i n_j\rangle$ since the mean vanishes, $\langle n_i\rangle = 0$. Using eq. (3.52) one has

$$\begin{aligned}\mathcal{D}_{ij} &= \left(\frac{q}{E}\right)^2 \int_0^\infty \mathrm{d}s \epsilon_{ikl} n_k(0) \epsilon_{jqr} n_q(s) \langle B_l(0) B_r(\mathbf{x}(s))\rangle \\ &= \left(\frac{q}{E}\right)^2 \int_0^\infty \mathrm{d}s \epsilon_{ikl} n_k(0) \epsilon_{jqr} n_q(s) \frac{1}{(2\pi)^6} \int \mathrm{d}^3k \int \mathrm{d}^3k' \left\langle \delta B_l(\mathbf{k}) \delta B_k(\mathbf{k}')\right\rangle \mathrm{e}^{\mathrm{i}\mathbf{k}\cdot\mathbf{x}(s)} \ .\end{aligned} \tag{3.66}$$

Again, in the next step the assumption $n_k(0)n_q(s) \approx n_k(0)n_q(0)$ is introduced due to the quasi-linear approximation. To be more specific, this approximation is valid if the deflection of the particle is small within one coherence length of the turbulent field:

$|\Delta\hat{\mathbf{n}}| \sim L_c/r_g \ll 1$. Furthermore, the same approximation guarantees that $\mathbf{x}(s) \approx \hat{\mathbf{n}}s$. The integral now can be evaluated in the same manner as in eq. (3.48), which results in the following expression:

$$\mathcal{D}_{ij} = \frac{\pi}{8}\left(\frac{qc}{E}\right)^2 (\delta_{ij} - n_i n_j) \int_{k_{\min}}^{k_{\max}} \mathrm{d}k \frac{\mathbf{B}^2(k)}{k} \ , \tag{3.67}$$

or, by representing it with the scalar diffusion coefficient in the quasi-linear approximation:

$$\mathcal{D}_{ij} = \mathcal{D}_0^{\mathrm{ql}} (\delta_{ij} - n_i n_j) \ , \quad \mathcal{D}_0^{\mathrm{ql}} \equiv \frac{1}{8}\left(\frac{qc}{E}\right)^2 L_c B_{\mathrm{rms}}^2 = \frac{1}{8}\frac{L_c}{r_g^2} \ . \tag{3.68}$$

At this point, $\mathcal{D}_0^{\mathrm{ql}}$ can be substituted in eq. (3.63):

$$\theta_{\mathrm{rms}}^2 \approx 4\mathcal{D}_0^{\mathrm{ql}} s = \frac{1}{2}\left(\frac{qc}{E}\right)^2 B_{\mathrm{rms}}^2 L_c s = \frac{1}{2}\frac{L_c}{r_g^2} s \tag{3.69}$$

which represents the root mean square angular spread around the initial direction and it is consistent with other approaches, for example [149].

This theoretical result is compared with a Monte Carlo simulation using CRPropa (appendix B). The comparison is shown in fig. 3.2. The simulation is performed by sampling 500 particle trajectories and recording their deflection angles θ_{rms} at various distances relative to the initial angle. By using two different energies, $E = \{2.0, 5.0\}\,\mathrm{EeV}$, in a turbulent magnetic field defined by $B_{\mathrm{rms}} = 1\,\mathrm{nG}$, and $L_c = 0.5\,\mathrm{Mpc}$, two gyroradii are compared, $r_g = \{2.16, 5.40\}\,\mathrm{Mpc}$. As it can be seen, the comparison of the theoretical calculation with the numerical result is in agreement for the second gyroradius in which the small angle approximation is still valid for the whole range of displayed distances. On the other hand, the first gyroradius in the given range of distances breaks the inequality $\mathcal{D}_0^{\mathrm{ql}} s < 1$. An investigation of the validity of the small angle approximation is reserved for the next section.

The angle θ_{rms}^2 is important in the reference frame of the particle. However, the observer is more interested in an angle that closes the line of sight from the source and the particle's arrival direction. That means that the angle of interest is given by

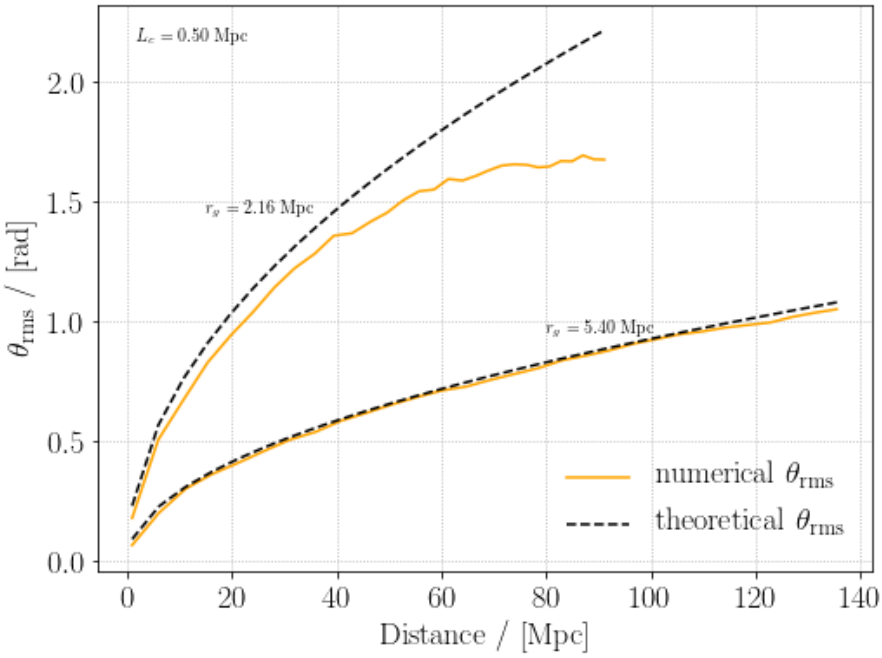

Figure 3.2: The plot shows the average deflection angle theoretically given with eq. (3.69) for two distinct gyroradii, $r_g = \{2.16, 5.40\}$ Mpc (black lines). The orange lines are the same values extracted from two propagation simulations (see details in the text). The displayed discrepancy between the theoretical and numerical results for the 2.16 Mpc gyroradius represents the violation of the small angle approximation.

$\alpha = \arccos(\hat{\mathbf{n}} \cdot \hat{\mathbf{r}}) = \arccos(\langle \hat{\mathbf{n}} \cdot \mathbf{r} \rangle / \langle |\mathbf{r}| \rangle)$ where $\mathbf{r}$ is a vector between the observer and the particle's origin. In the limit of quasi-rectilinear propagation, the root mean square quantity of this angle is given by [143]:

$$\alpha^2_{\rm rms} \approx \frac{4}{3}\mathcal{D}_0 L = \frac{1}{3}\theta^2_{\rm rms} = \frac{1}{6}\left(\frac{qc}{E}\right)^2 B^2_{\rm rms} L_c L \tag{3.70}$$

where s has been substituted with L to highlight the change of the context, from the path that the particle crossed to the distance from the particle's origin.

Due to scatterings, not only that the particle's original direction is altered, but also it is delayed compared to the speed of light, albeit, locally, it is approximately taken that it moves at the speed of light (see eq. (3.51)). The formula can be derived from the above expressions and reads:

$$c\langle t_{\rm delay} \rangle \approx \frac{1}{3}\mathcal{D}_0 s^2 \ . \tag{3.71}$$

3.4.2 Transition from rectilinear propagation to diffusion

Equation (3.61) is general enough to demonstrate the transition from rectilinear propagation to (normal) diffusion already defined in relations (3.14). The mean square displacement in this case yields:

$$\begin{aligned}\left\langle r^2(t)\right\rangle =& \left\langle x^2(t)\right\rangle + \left\langle y^2(t)\right\rangle + \left\langle z^2(t)\right\rangle \\ =& \frac{ct}{\mathcal{D}_0}\left[1 - \frac{1}{2ct\mathcal{D}_0}\left(1 - \mathrm{e}^{-2ct\mathcal{D}_0}\right)\right] \ . \end{aligned} \tag{3.72}$$

In the rectilinear regime, $ct\mathcal{D}_0 \ll 1$, that equation gives:

$$\left\langle r^2(t)\right\rangle \xrightarrow[ct\mathcal{D}_0 \ll 1]{} (ct)^2 \qquad \text{(rectilinear)} \ , \tag{3.73}$$

while in the diffusive regime, $ct\mathcal{D}_0 \gg 1$, the limit becomes:

$$\left\langle r^2(t)\right\rangle \xrightarrow[ct\mathcal{D}_0 \gg 1]{} \frac{ct}{\mathcal{D}_0} \qquad \text{(diffusive)} \ . \tag{3.74}$$

This result can be better understood with the help of eq. (3.69), valid within the small angle approximation, in which the quantity $ct\mathcal{D}_0$ represents the root mean square deflection angle $ct\mathcal{D}_0 = \theta_{\mathrm{rms}}^2/4$, so the transition is expressed relative to $\theta_{\mathrm{rms}} = 2\,\mathrm{rad}$.

Another way to see the result is by the second equality in eq. (3.69). If the trajectory length $L = ct$ is transformed in a number of coherence lengths crossed $\lambda \equiv L/L_c$, the above mentioned regimes are then distinguished compared to:

$$\lambda(L_c/r_g)^2/8 \approx 1 \ , \tag{3.75}$$

which is plotted on the left panel of figure 3.3. The interpretation is now straightforward: the diffusion regime occurs when the deflection L_c/r_g is high and/or when many coherence lengths are crossed, and vice versa for the rectilinear regime. One should notice that eventually, $t \to \infty$, or to be more precise, if the age of the Universe allows, every motion will inevitably enter the diffusive picture, and the ratio L_c/r_g only deter-

mines whether will this happen sooner or later. To underline the context again, this perspective is correct when the small angle approximation is valid, $L_c \ll r_g$.

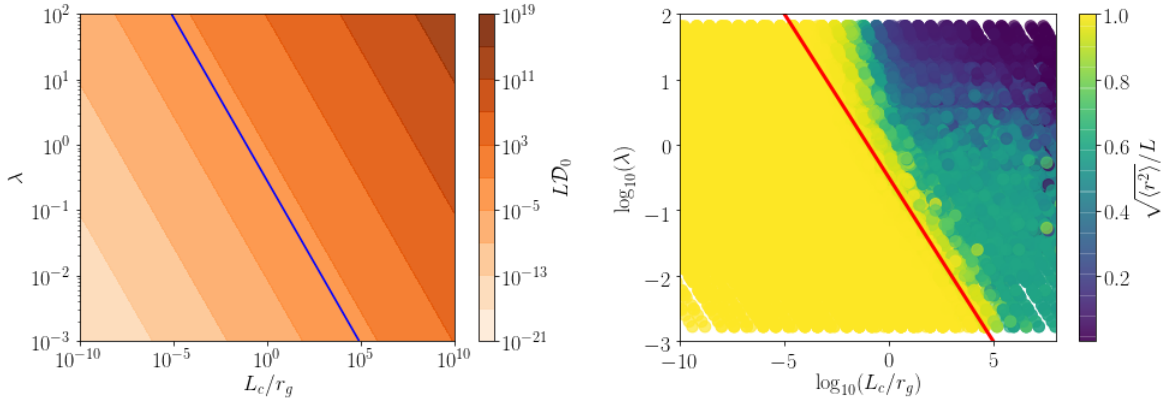

Figure 3.3: The calculated quantity $L\mathcal{D}_0$ for ranges of $\lambda = L_c/L$ and L_c/r_g is plotted on the left panel with eq. (3.75) marked as the blue line. The quantity $\sqrt{\langle r^2\rangle}/L$ on the right panel is numerically obtained by sweeping the same range of parameters with independent simulations, where drawn every dot is one simulation in which two hundred particles were propagated in a turbulent field for a fixed length L. The red line on the right corresponds to the blue line on the left, which shows that Monte Carlo simulations are in good agreement with the theoretical consideration where the discrepancy indicates the breakage of the interpretation based on the small angle approximation.

In the lower limit, the spatial diffusive coefficient $\mathcal{K}$, commonly defined as $\langle r^2\rangle = 2\mathcal{K}t$, reads

$$\mathcal{K}(E) = \frac{c}{2\mathcal{D}_0} = 4\frac{cr_g^2(E)}{L_c} \tag{3.76}$$

which is known in literature as the (spatial) diffusion coefficient at "high" energies [150] where the constant factor in the front depends on the definition of the coherence length (eq. (3.47)) and, hence, may vary.

To get a broader picture without relying on the small angle approximation, the following numerical procedure is employed to demonstrate the transition. A few thousand simulations in CRPropa were performed with different initial parameters[2]: the particle's energy E, the magnetic field strength $B_{\rm rms}$, the coherence length $L_c(L_{\rm min}, L_{\rm max})$ and the spectral index of turbulence n. In every simulation, two hundred protons are simulated in a different realisation of a turbulent magnetic field for ten fixed trajectory distances L up to 100 kpc. The right panel of figure 3.3 shows how the quantity $\sqrt{\langle r^2\rangle}/L$, which

[2]The included ranges of the simulation parameters are: $E = [10^{15}, 10^{21}]$ eV, $B_{\rm rms} = [10^{-10}, 10^{-5}]$ G, $L_{\rm min} = 2$ kpc, $L_{\rm max} = [5, 150]$ kpc, and $n = \{0, 1, 3/2, 5/3, 3, 5\}$.

can serve as a measure of the transition, depends on the initial parameters which are expressed in $\lambda = L_c/L$ and L_c/r_g. The transition occurs where it was expected by eq. (3.75). The numerical result also depicts the range of the small angle approximation, which breaks at $r_g \sim L_c$: the border obtained numerically bends away from the transition line after $L_c > r_g$.

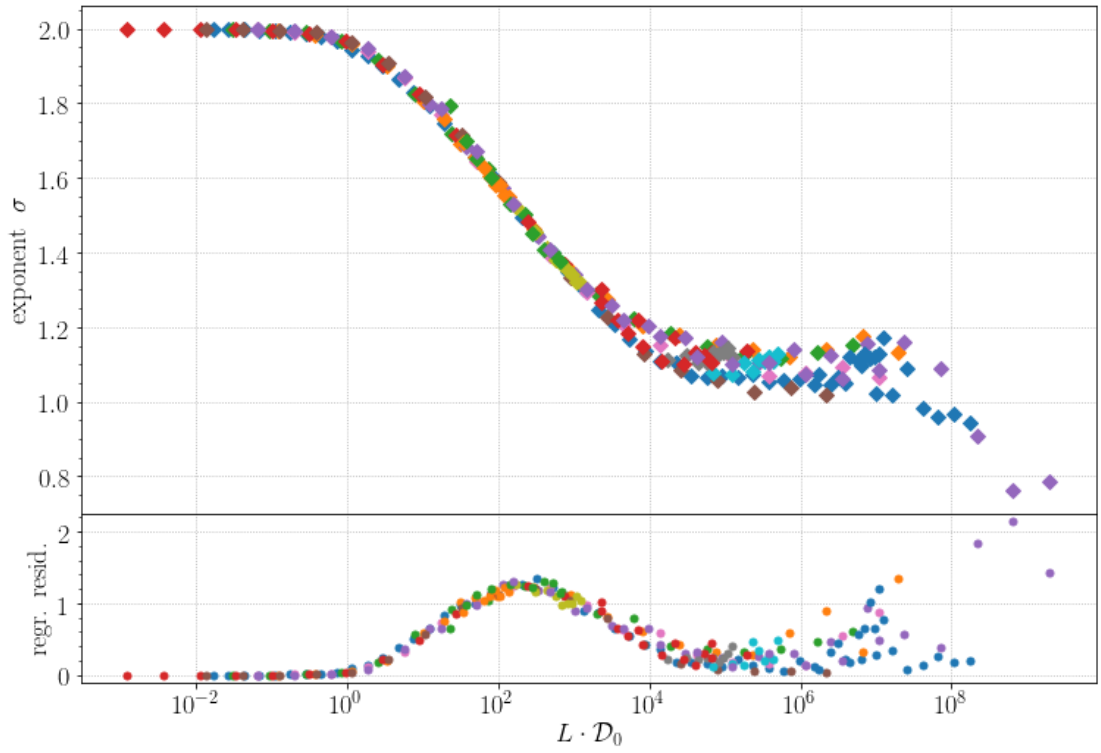

Figure 3.4: The transition between the rectilinear propagation and diffusion is shown in the upper panel, which is obtained by simulating particles of various energies in various realisations of a turbulent magnetic field for a fixed propagation distance $L = 10\,\mathrm{kpc}$ (see footnote 2 for the simulation parameters). The quantity $L\mathcal{D}_0$ is a dimensionless measure defined in eq. (3.72) which quantifies the type of propagation. The exponent is calculated from a linear regression of $\log\left(\langle r^2(L)\rangle\right) = \sigma \log(L) + b$, where b is a constant independent of L (not shown in the plot). The lower panel represents the regression residual indicating how well the fitting function describes the numerical data points. It can be seen that the transition starts at $L\mathcal{D}_0 \approx 1$.

Alternatively, the numerical result can be plotted as follows. The assumption $\langle r^2(L)\rangle \propto L^\sigma$ is taken to compute the linear regression in a $\log - \log$ space in which the exponent σ becomes the slope. The scalar diffusion coefficient, $\mathcal{D}_0$, is derived from the simulation parameters using eq. (3.68). The procedure is repeated for a different set of initial parameters. All retrieved σ versus $L \cdot \mathcal{D}_0$ are plotted in fig. 3.4. As one

can see, both limiting regimes are reproduced: $\sigma \simeq 2$ when $L\mathcal{D}_0 \ll 1$ and $\sigma \simeq 1$ when $L\mathcal{D}_0 \gtrsim 1$. The lower plot of the same figure shows the standardized residual of the linear regression: values bigger than zero indicate that the straight line does not fit the provided data well in some regions of $L\mathcal{D}_0$. These regions are regimes of superdiffusion ($2 > \sigma > 1$) and subdiffusion ($1 > \sigma$). Figure 3.5 illustrates two types of propagation, diffusive and superdiffusive, as an example of two distinct trajectories. One could notice that superdiffusive and diffusive trajectories are best described through Lévy flights which, simply said, combine diffusive motion with rectilinear jumps [151]. The model of Lévy flights is especially important in structured magnetic fields, which are characterized by different field strengths and coherence lengths in different domains. Subdiffusion occurs when particles are trapped within one region of space due to magnetic mirroring cf. described in sec. 3.1.

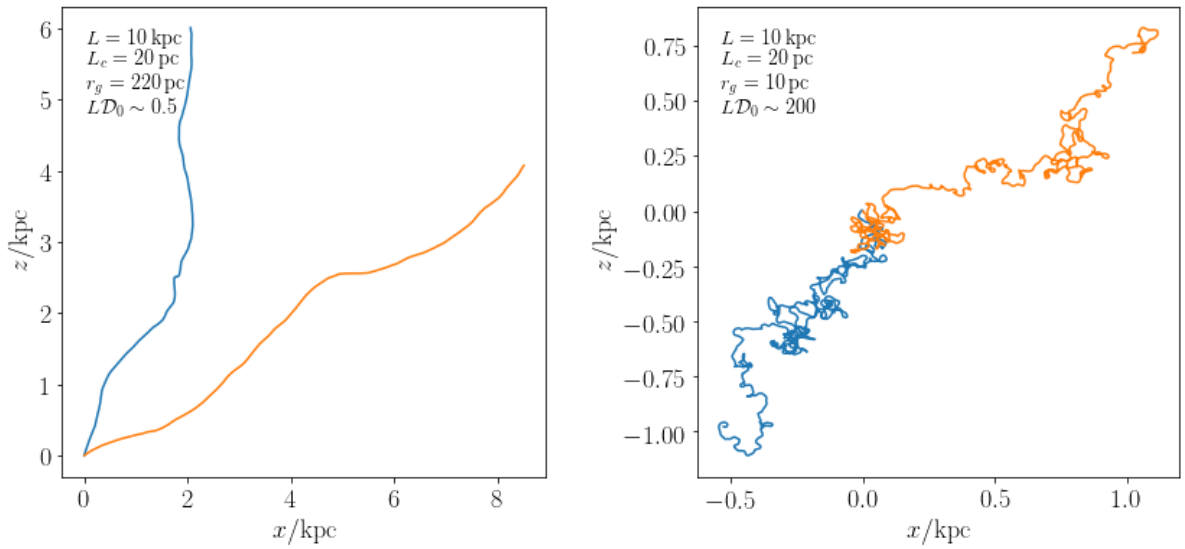

Figure 3.5: An illustration of particle trajectories in two regimes of propagation determined by the value of $L\mathcal{D}_0$: superdiffusive ($L\mathcal{D}_0 \sim 0.5$) on the right panel and diffusive ($L\mathcal{D}_0 \sim 200$) on the left panel.

4 | Anisotropies caused by single source

In this chapter[1], a study of cosmic ray source distributions and how they affect anisotropies in the arrival direction is conducted. Without the inclusion of cosmic magnetic fields, which bend charged particle trajectories, all studies of anisotropies, in essence, can be reduced to geometrical considerations similar to visible-light astronomy, for example. In order not to remain solely on that, a turbulent magnetic field will be included in the study, with some general remarks on structured magnetic fields.

As always with the scientific methodology, the first approach would be to establish the simplest model which can accommodate the already given observations, and systematically study its consequences by trying to find inconsistencies with experimental data or other, more founded, hypotheses. In the case of finding an inconsistency, one would either reject the initial model as insufficient, or upgrade it with additional assumptions, and, thus, make it viable again.

The first plausible assumption in this procedure of building the simplest model is that the cosmic ray flux is dominated by neighbouring sources. This implicitly follows from the fact the intensity of cosmic rays has generally the inverse square dependence with distance. Therefore, one should, at first order at least, focus on potential neighbouring sources. Looking further away, more sources are included in the considered volume and, as the matter distribution in the Universe approaches homogeneity at large scales, these sources have the tendency to contribute isotropically to the flux. On top of that, due to longer paths through intervening magnetic fields with an inevitable turbulent component, the more remote sources tend to spread their arrival directions more widely,

[1] This chapter is based on [1].

which also makes their contribution to the flux isotropic, and thus less interesting in the context of anisotropies.

The topic of cosmic ray propagation in a turbulent field was elaborated in detail in the previous chapter. However, an important consideration of the energy losses is unaccounted. Cosmic ray interactions represent a complex and broad subject on its own right, and cannot be easily covered in this work, so the reader is referred to other literature, such as the textbooks [88, 8, 10]. Nevertheless, one can summarise that cosmic rays lose their energy during the propagation through the Universe depending on their energy both by interacting with photons or, if they are unstable, by decaying. The expansion of the Universe also causes adiabatic energy loss on cosmological length scales. Apart from losing energy, cosmic rays also generate secondary particles, like other cosmic rays, gamma rays and neutrinos. The length scale on which a particular process acts can be illustrated through fig. 4.1 on a proton and on a radioactive isotope of sulfur, from which the main message that can be read out is: energy loss processes can be to some extent neglected below $\sim 10^{20}$ eV on distances shorter than a few megaparsecs.

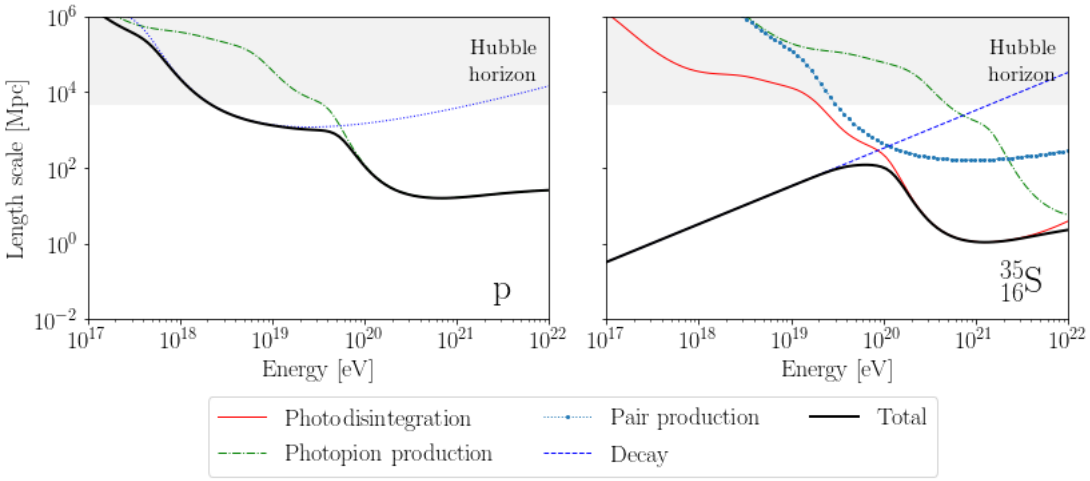

Figure 4.1: Energy loss length on an example of proton and sulfur-35. A proton (right panel) or sulfur nucleus (left panel) in the high energy range interact with photons of cosmic microwave background (CMB) from the early Universe and with infrared photons emitted by the present matter in the Universe (those photons are called the extra-galactic background light, or EBL for short). As radioactive, it also decays with a half-life of 87.5 days. Generated with CRPropa (ch. B).

The benefit of focusing only on neighbouring sources in anisotropy studies is, hence, twofold. On the one hand, the contribution from local sources is dominant in the total

flux, and therefore their relevance for anisotropies. On the other hand, the significance of energy losses is minimised, and thereby the complexity of that subject is to some degree circumvented, making the anisotropy modelling more concrete and, consequently, falsifiable.

The main constraint for anisotropies of ultra-high energy cosmic rays is the dipolar anisotropy detected by the Pierre Auger Observatory, as noted in sec. 2.5.3. Every considered model should be able to reproduce this fact. The dipolar anisotropy basically means more cosmic rays are coming from one side than from the other. Logically, the reason could be an inhomogeneity of sources between the two sides. This inhomogeneity in the simplest case can be caused only by a single neighbouring source.

Centaurus A (Cen A) or the Virgo cluster are the closest candidates that have been studied many times before [152, 153, 154, 155, 156, 157, 158]. Besides those studies focused on specific sources, more general studies of a single source with various approaches and aims were conducted, such as a diffusion model [159, 160, 161], simulated ballistic propagation from a single source [162], a single source in the context of the galactic magnetic field [152], etc. The main problem of these studies is that they are usually very concrete with their assumptions, which depend on a specific position of the source, the injected composition, luminosity, intervening magnetic field properties and similar, and one cannot easily apply the knowledge contained in them to situations when some of the used assumptions alter due to a new experimental evidence or to a contribution from another research field. Their results also cannot be used when constructing scenarios for Monte Carlo simulations in a straightforward sense. For example, before, galactic sources had dominated the interest in the community and papers that investigated them were written under the assumption of diffusional propagation, which is natural to include for the galactic environment, but due to this assumption, their results cannot be applied to extra-galactic contexts.

With that argued, the main work in this chapter is developed around the idea that there exists a neighbouring source that contributes a significant fraction of the total ultra-high energy cosmic ray flux compared to the next significant contribution in flux

source. The goal is to analyse anisotropies from a neighbouring source, without specifying its distance or luminosity, by focusing primarily on properties of an intervening turbulent magnetic field in such a way as to satisfy given experimental constraints. As noted, the experimental constraints exist for large-scale anisotropies only. Therefore, the focus here will also be on them by relying on the angular power spectrum, which is a rotationally invariant observable. That property enables a more general analysis without focusing on specific directions on the sky. Of the most relevance here is the generality of the results, which require analytical tools, but they will be accompanied with Monte Carlo simulations in parts where it will be unavoidable. These results can be used to make predictions and constrain the model's parameters, which will also be shown later in the chapter.

4.1 Single source model

When air shower experiments (see sec. 2.4.1) measure arrival directions of UHECR events, every event is interpreted as one charged particle hitting the earth's atmosphere after arriving from a remote source. In chapter 3 it was shown that a charged particle is scattered on irregularities of intervening magnetic fields, especially on those from turbulent fields. Thereby, the particle undergoes Brownian (random) motion in its flight direction when crossing many coherence lengths of a turbulent magnetic field.

This stochastic motion placed on a unit sphere, in which the particle starts its movement from μ, and it moves in a time κ^{-1}, is described with the Brownian motion distribution denoted as $BM_3(\mu, \kappa)$ where the index 3 stands for three-dimensional case. The Brownian motion distribution which starts from $(\theta, \phi) = (0, 0)$ is given by the formula [163, 164]:

$$f_{BM}(\theta, \phi|\kappa_{BM}) = \sum_{k=1}^{\infty}(2k+1)\mathrm{e}^{-k(k+1)/4\kappa_{BM}}P_k(\cos\theta) \tag{4.1}$$

where P_k are the Legendre polynomials of order k.

This is a good place to introduce a concept from directional statistics - the mean

resultant length which is a measure of the angular spread $\rho = \frac{1}{N}||\sum_{i=1}^{N} \mathbf{x}_i||$ where $\mathbf{x}_i$ is a unit vector of an event, like an arrival direction event of a single cosmic ray and N is the total number of events. For $BM_3(\mu, \kappa_{BM})$, the mean resultant length is $\rho = \mathrm{e}^{-(2\kappa_{BM})^{-1}}$. In the context of Brownian motion in flight directions described in sec. 3.4, one is interested in expressing this quantity in terms of the flight direction unit vector $\hat{\mathbf{n}}$ which is correlated with the unit vector pointing from the observer to the source $\hat{\mathbf{r}}$. Thus, normalized eq. 3.60 gives:

$$\rho = \langle \hat{\mathbf{n}} \cdot \hat{\mathbf{r}} \rangle \ . \tag{4.2}$$

The correlator has a complex form based on equations in sec. 3.4 and will not be listed here, but the limiting values are important for the further analysis: $\langle \hat{\mathbf{n}} \cdot \hat{\mathbf{r}} \rangle \xrightarrow[L\mathcal{D}_0 \ll 1]{} 1 - \frac{2}{3}\mathcal{D}_0^{\mathrm{ql}} L$, and $\langle \hat{\mathbf{n}} \cdot \hat{\mathbf{r}} \rangle \xrightarrow[L\mathcal{D}_0 \gg 1]{} 0$.

Roberts and Ursell [165] showed that $BM_3(\mu, \kappa_{BM})$ can be approximated by the Fisher distribution (or Fisher – von Mises distribution on the $(p-1)$-dimensional sphere where $p = 3$) when they share the same mean resultant length [166, 164]. The Fisher distribution can be seen as a spherical analogy by a normal distribution (in a plane). When considering small angular spreads of data the Fisher distribution is well described with a normal distribution.

Consequently, the arrival direction distribution of cosmic rays that are coming from a single source can be modelled with the Fisher distribution centred around $(\theta, \phi) = (0, 0)$:

$$f_F(\hat{\mathbf{r}}|\kappa) = \frac{\kappa}{4\pi \sinh(\kappa)} \exp(\kappa \hat{\mathbf{r}} \cdot \hat{\mathbf{r}}_{\mathrm{src}}) \ , \tag{4.3}$$

where $\mathbf{r}_{\mathrm{src}}$ is the position of a single source, and $\kappa (\equiv \kappa_F)$ the concentration parameter. Since this distribution by construction shares the same mean resultant length of $BM_3(\mu, \kappa_{BM})$, the diffusion coefficient in flight directions and the total travelled length can be related to κ through:

$$\kappa = A_3^{-1}(\rho) = A_3^{-1}\left(\langle \hat{\mathbf{n}} \cdot \hat{\mathbf{r}} \rangle\right) \ . \tag{4.4}$$

The function $A_3(\kappa)$ relates κ and ρ in the following way

$$\rho = A_3(\kappa) = \coth(\kappa) - \frac{1}{\kappa} \, . \tag{4.5}$$

For $\kappa \ll 1$, $A_3(\kappa) \approx \kappa/3$, while for $\kappa \gg 1$, $A_3(\kappa) \approx 1 - 1/\kappa$ (from Appendix 1 in [164]).

The parameter κ will be called the spread parameter from now on. That is because it encodes everything which influences the angular spread of arrival directions, such as the presence of magnetic fields. κ goes to zero in the limit of extremely high deflections in which the original arrival direction of a particle is totally erased, and so does the source position. For $\kappa = 0$, the Fisher distribution is just a uniform distribution on a sphere. In the absence of deflections, when magnetic fields do not exist, the distribution behaves like a point source, i.e., a delta function.

To accommodate other sources which, by assumption here, contribute to the total flux only isotropically, the Fisher distribution is modified and re-normalised in the following way

$$f_{\mathrm{src+bg}}(\hat{\mathbf{r}}|\eta, \kappa) = \frac{1-\eta}{4\pi} + \eta \frac{\kappa}{4\pi \sinh(\kappa)} \exp(\kappa \hat{\mathbf{r}} \cdot \hat{\mathbf{r}}_{\mathrm{src}}) \tag{4.6}$$

where η is the relative flux $j_{\mathrm{src}}/j_{\mathrm{tot}}$ of a single source.

This approach of modelling the spread of arrival directions from a single source is also used in [167]. The difference between the interpretation of eq. (4.6) here and the one used in [167] needs an elaboration. Harari et al. argue that "the isotropic term arises mostly from particles that diffused long times and made several turns before reaching the observer," while here the isotropic term is due to other sources which contribute only isotropically. The author of this work did not find any grounds for the former interpretation in his investigation. The Fisher distribution, as a good approximation of the Brownian movement distribution, should also take into account multiple turns. In the limit of large spreads, $\kappa \to 0$, the Fisher distribution already gives isotropy. Thereby, placing an additional term by hand rises the question of which underlying mechanism would reproduce a distribution with such constant term. It is worth to be reminded

that a particle locally does not recognise the regime of diffusion when it propagates – it just propagates ballistically, and the concept of diffusion is only our shortcut when the particle motion is analysed globally. Besides that, numerical simulations do not show any disagreement with the assumed distribution, which fits perfectly to any collection of data acquired from trajectory simulations, even when particles enter in a so-called diffusion regime, $\mathcal{D}_0 L \gg 1$. Simulations of cosmic ray propagation in a turbulent field were performed, in terms of the range of parameters. in the same manner as for fig. 3.3 to check this. A few examples of the fit are shown in the left panel of fig. 4.2. The fit is done on a density of colatitude θ for the Fisher distribution, given by the expression:

$$f_F(\theta, \kappa) = \frac{\kappa}{2\sinh(\kappa)} \mathrm{e}^{\kappa\cos(\theta)} \sin(\theta) \ . \tag{4.7}$$

The histograms are created by binning the angle θ of all particles at a certain point during the propagation. The angle θ represents the deviation from the initial flight direction when the particle reached a certain point where it was recorded. The right panel of the same figure shows that the spread parameter κ is a function of $\mathcal{D}_0 L$ as was stated above. The red line shows the analytical expression of $\kappa\left(\mathrm{e}^{-2\mathcal{D}_0 L}\right)$ in the small angle approximation domain where the diffusion parameter, $\mathcal{D}_0$, can be calculated directly from physical parameters. The approximation is valid down to $\kappa \gtrsim A_3^{-1}(1 - 2\mathcal{D}_0 L/3) \approx A_3^{-1}(1 - 2/3) \gtrsim 1.1$. That also agrees with Monte Carlo simulations in fig. 4.2: the overlapping of the red line with the simulation results is down to ~ 1. Below that point, one needs to look for an expression for $\mathcal{D}_0$ in the diffusive regime. This is not done in this work, although $\mathcal{D}_0$ should follow other known diffusive coefficients given, for example, in [150].

In section 4.1.1 the small angle approximation and the parameter space of physical quantities will be inspected in more detail.

Now, to study how the given model corresponds to the anisotropy observables, the angular power spectrum of the distribution (4.6) is derived. The angular power spectrum is rotationally invariant, so without loss of generality the observer can be placed at the origin of the coordinate system and the z-axis can be chosen along the source direction:

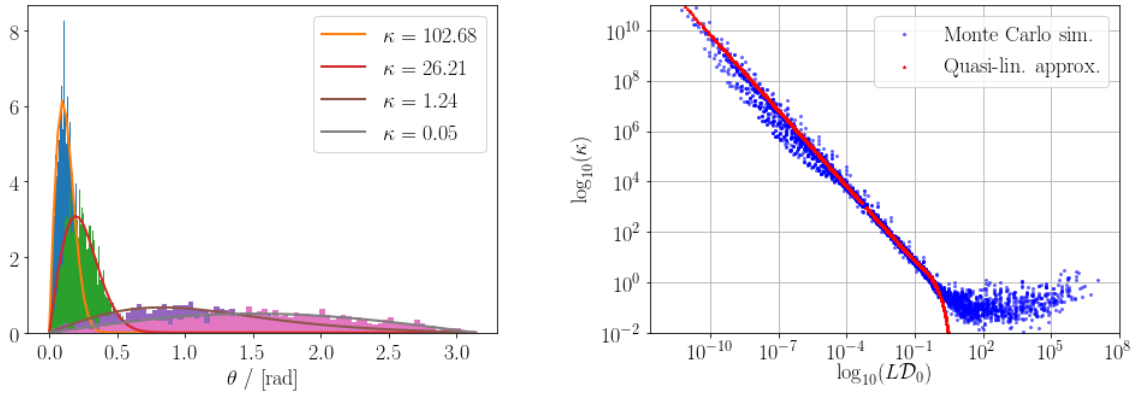

Figure 4.2: A comparison of the density of colatitude θ given by eq. (4.7) of several κ values is shown on the left panel. The right panel demonstrates that the spread parameter κ is indeed a function of $\mathcal{D}_0 L$ without any additional parameters needed. The red line represents the analytically calculated κ for given physical parameters of the simulations when $\mathcal{D}_0$ is described by the small angle approximation.

$\hat{\mathbf{r}} \cdot \hat{\mathbf{r}}_{\text{src}} = \cos(\theta)$. Inserting (4.6) in (A.18) gives:

$$\begin{aligned} a_{\ell m} =& \frac{1-\eta}{4\pi} \int_0^{2\pi} d\varphi \int_0^{\pi} d\theta \, \sin\theta Y_\ell^{m*}(\theta,\varphi) \\ &+ \eta \frac{\kappa}{4\pi \sinh(\kappa)} \int_0^{2\pi} d\varphi \int_0^{\pi} d\theta \, \sin\theta \exp(\kappa\cos(\theta)) Y_\ell^{m*}(\theta,\varphi) \qquad (4.8) \\ =& \delta_{\ell 0} \frac{1-\eta}{4\pi} 2\sqrt{\pi} + \delta_{m0} \sqrt{\frac{2\ell+1}{4\pi}} \int_0^{\pi} d\theta \, \frac{\kappa \sin(\theta)}{2\sinh(\kappa)} \exp(\kappa\cos(\theta)) \, P_\ell(\cos\theta) \, . \qquad (4.9) \end{aligned}$$

The last integral $\mathcal{I}_\ell = \frac{\kappa}{2\sinh(\kappa)} \int_{-1}^{1} du \exp(\kappa u) P_\ell(u)$ can be reduced to a recurrence relation using the property of Legendre polynomials $(2n+1)P_n(u) = \frac{d}{du}\left[P_{n+1}(u) - P_{n-1}(u)\right]$:

$$\mathcal{I}_0 = 1 \, , \quad \mathcal{I}_1 = \coth\kappa - \frac{1}{\kappa} \, , \quad \mathcal{I}_\ell = \mathcal{I}_{\ell-2} - \frac{2\ell-1}{\kappa} \mathcal{I}_{\ell-1} \, . \qquad (4.10)$$

The recurrence yields the final form expressed in terms of the modified Bessel function of the first kind:

$$\mathcal{I}_\ell = \sqrt{\frac{\pi}{2}} \frac{\sqrt{\kappa}}{\sinh\kappa} I_{\ell+\frac{1}{2}}(\kappa) \qquad (4.11)$$

$$a_{\ell 0} = \delta_{\ell 0} \frac{1-\eta}{\sqrt{4\pi}} + \eta \sqrt{\frac{2\ell+1}{4\pi}} \sqrt{\frac{\pi}{2}} \frac{\sqrt{\kappa}}{\sinh(\kappa)} I_{\ell+\frac{1}{2}}(\kappa) \, . \qquad (4.12)$$

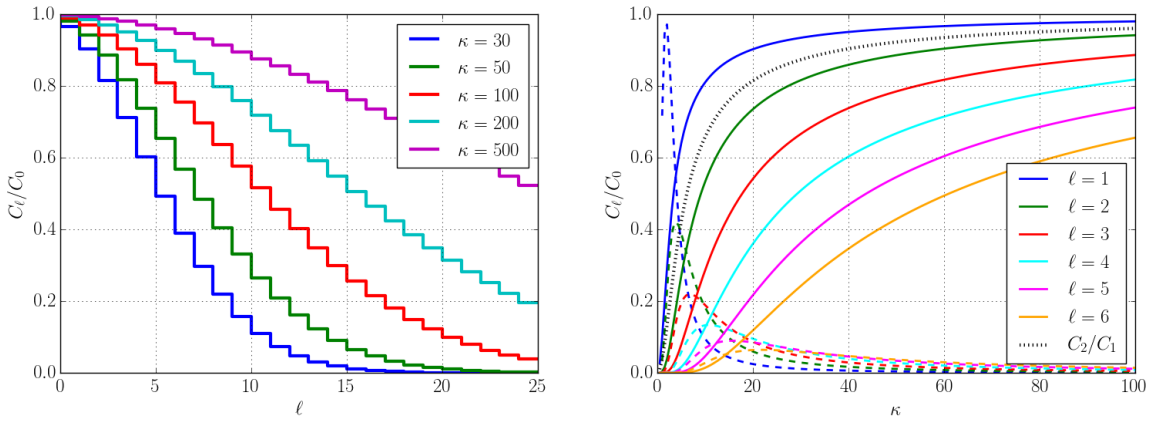

Figure 4.3: These two plots illustrate solutions of the single source model (4.13) without the background contribution ($\eta = 1$). The first one shows the dependence of the normalized power spectrum C_ℓ on the multipole moment ℓ for different parameters κ, while the second one shows the dependence of the power spectrum on κ for the first few moments; the dashed curves are derivatives of solid lines multiplied by a factor 10; the black dotted line represents the ratio $x = C_2/C_1$ versus κ. All figures in this work are plotted using [168].

The final power spectrum reads

$$C_\ell = \begin{cases} \frac{1}{4\pi} & \text{if } \ell = 0 \\ \eta^2 \frac{1}{4\pi} \mathcal{I}_\ell^2 = \eta^2 \frac{\kappa}{8} \sinh^{-2}(\kappa) I^2_{\ell+\frac{1}{2}}(\kappa) & \text{if } \ell > 0 \end{cases} \tag{4.13}$$

where it is advisable for numerical calculations to use the recurrence form (4.10) instead of the last form due to numerical instability around $\kappa \approx 0$.

The solution for $\eta = 1$ is plotted in fig. 4.3 for the first few moments and for several parameters κ. The figure shows consistency in the following limiting cases: when the angular spread is high enough, or the spread parameter is low enough, to erase the position of the source completely, only the monopole component is present ($\forall \ell > 0 \quad \lim_{\kappa \to 0} C_\ell = 0$). In the opposite limit, without any deflections, the source is presented in the form of a delta function and all moments are equal. The parameter η governs the ratio of higher multipoles to the monopole.

The model's parameters, κ and η, can be determined from the ratios of multipoles.

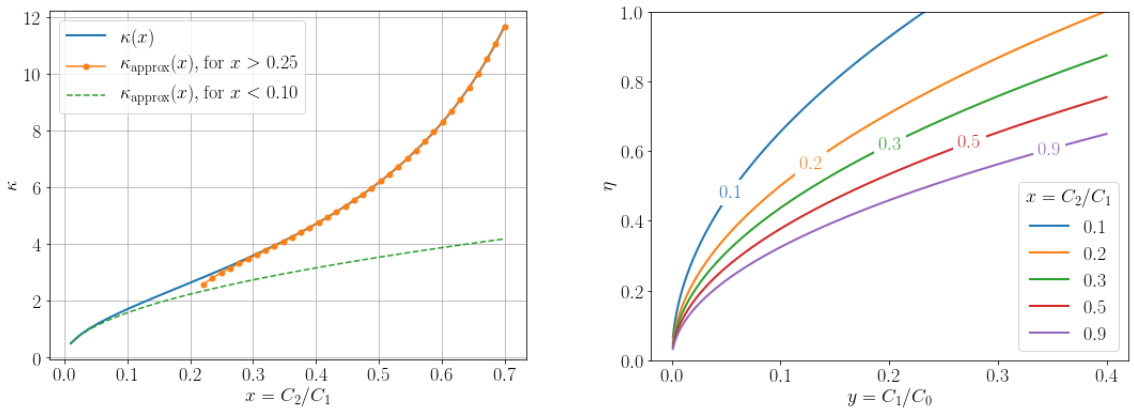

Figure 4.4: The left panel shows how to retrieve parameter κ from the ratio of the quadrupole and the dipole ($x = C_2/C_1$) with the two analytical approximations described in the footnote. The right panel shows how η, which parametrises the flux contribution of the single source, can be determined from $x = C_2/C_1$ and the relative dipole amplitude $y = C_1/C_0$.

In particular, the ratio of the quadrupole and the dipole, $x = C_2/C_1$, is given by:

$$\frac{C_2}{C_1} \equiv x = \left[\left(\coth\kappa - \frac{1}{\kappa}\right)^{-1} - \frac{3}{\kappa}\right]^2 . \tag{4.14}$$

In fig. 4.4, eq. (4.14) has been solved for κ numerically[2]. The derivative of $\mathrm{d}x(\kappa)/\mathrm{d}\kappa$ is always positive, which confirms the monotonous behaviour of the function and implies the existence of a unique solution for κ in the domain of interest. The parameter η is then expressed through $y = C_1/C_0$ and $\kappa(x)$ (fig. 4.4):

$$\eta\,(y, x) = \frac{\sqrt{y}\kappa(x)}{|\kappa(x)\coth\kappa(x) - 1|} . \tag{4.15}$$

The model gives $y = C_1/C_0 \leq 1$, which implies $\eta \geq [\coth(\kappa) - 1/\kappa]^{-1}$. On the right panel of fig. 4.4 this inequality is violated for certain pairs x and y, where η becomes larger than unity, which is nonphysical since it would result in negative flux in certain directions, c.f. eq. (4.6).

[2]Nevertheless, useful analytical expressions in case of low ($x < 0.1$) and high ($x > 0.25$) ratio limits can be obtained:

$$\kappa(x) \approx \kappa_{\rm approx}(x) = \begin{cases} \frac{3-\sqrt{x}+\sqrt{x+6\sqrt{x}-3}}{2-2\sqrt{x}}, & \text{valid for } x \gtrsim 0.25, \\ 5\sqrt{x}, & \text{valid for } x \lesssim 0.1\,. \end{cases}$$

4.1.1 The spread parameter in the small angle approximation

The deflections of cosmic rays in intervening magnetic fields cause blurring to a source image. Interactions can also contribute to the angular spread, but for highly energetic particles their effect can be neglected, as the scattering angle is of the order of the inverse Lorentz factor. Relevant quantities for deflections in magnetic fields are the magnetic rigidity $\mathcal{R} = E/Ze$ and properties of the intervening magnetic field. In the small angle approximation, see sec. 3.4.1, where $\mathcal{D}_0 L \leq 1$, one can approximate eq. 4.4 with the already mentioned expression for A_3:

$$\kappa = A_3^{-1}\left(1 - \frac{2}{3}\mathcal{D}_0^{\mathrm{ql}} L\right) \approx \frac{3}{2}\left(\mathcal{D}_0^{\mathrm{ql}} L\right)^{-1} \quad . \tag{4.16}$$

Inserting eq. (3.70) in the last expression yields:

$$\kappa \approx 2\alpha_{\mathrm{rms}}^{-2} = 12\mathcal{R}^2 B_{\mathrm{rms}}^{-2}\left(L_c L\right)^{-1} \tag{4.17}$$

where θ_{rms} is the root mean square deflection angle, L is the total travelled distance, L_c and B_{rms} are the coherence length and the root mean square strength of a turbulent magnetic field, respectively. One needs to notice that the approximation for large κ in $A_3^{-1}(\rho)$ breaks sooner ($\kappa \sim 2$) when $\kappa \to 0$ than the small angle approximation, described in sec. 3.4.2.

The numerical form, useful in the ultra-high energy cosmic ray context, is given by:

$$\kappa \approx 140.2 \cdot \left(\frac{\mathcal{R}}{\mathrm{EV}}\right)^2 \left(\frac{B_{\mathrm{rms}}}{\mathrm{nG}}\right)^{-2} \left(\frac{L}{\mathrm{Mpc}}\frac{L_c}{100\mathrm{kpc}}\right)^{-1} \quad . \tag{4.18}$$

Cosmic rays that are deflected within a particular realisation of a Kolmogorov-type turbulent field will not generally be consistent with the smeared shape of the Fisher distribution if they are not sufficiently randomized by traversing multiple coherence lengths of the turbulent magnetic field defined in eq. (3.50). That is now going to be checked numerically.

Cosmic rays in a turbulent magnetic field are simulated in CRPropa (appendix B)

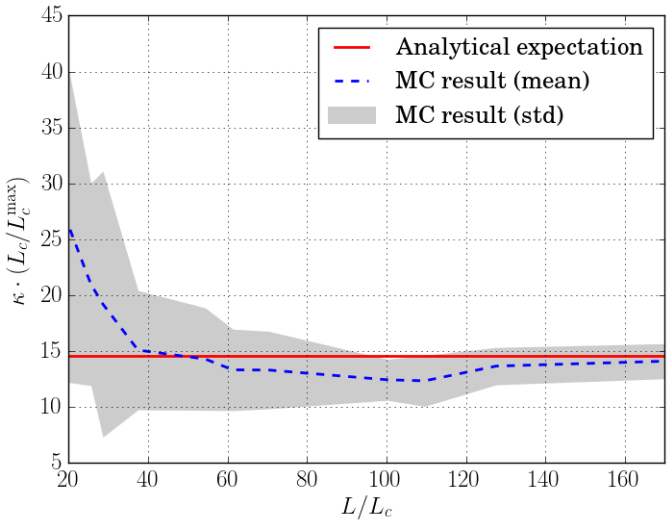

Figure 4.5: It is numerically checked how many coherence lengths cosmic rays need to traverse to be sufficiently randomized to match the predicted value from the Fisher distribution. The analytical expectation follows from equation (4.17), where the result is multiplied by $L_c/L_c^{\max}$ to remove the dependence of κ on L_c to stress the discrepancy; $L_c^{\max} = 256$kpc but it could be any constant length as it serves only as a normalization constant. For less than approx. 40 L_c the parameter κ jumps because the turbulent field on such scales correlates the movement of cosmic rays, which tends to create additional patterns within the source image that appear as smaller inner hot spots.

over the fixed distance of 5 Mpc. The forward propagation method is used to propagate 5 EeV energy protons through different realisations of the turbulent magnetic field given by $B_{\rm rms} = 5\,$nG, $L_{\rm min} = 20\,$kpc, and L_c ranging from 28 to 256 kpc. For every L_c, 30 random realisations of the magnetic field are generated to calculate the mean and the variance. Particles are detected if they hit an observer sphere (later just the observer). The radius of the observer was set to 200 kpc, and it is chosen so to minimise the artificial effect of the finite observer, which affects the angular spread but, at the same time, to register at least a few hundred events (see sec. B.3 for details). Numerically, κ is calculated using eq. (4.4). Figure 4.5 shows the result from which it can be concluded that at least 40 coherence lengths are needed to reproduce the shape of the spread parameter which corresponds to the analytical form.

To verify the dependence on the other parameters in equation (4.17) the same approach is used following in part ref. [169]. The coherence length of the turbulent field is set to 100 kpc and the other parameters are set to $B_{\rm rms} = 5\,$nG, $\mathcal{R} = 5\,$EV, $L = 5\,$Mpc when they are not subject of the check themselves.

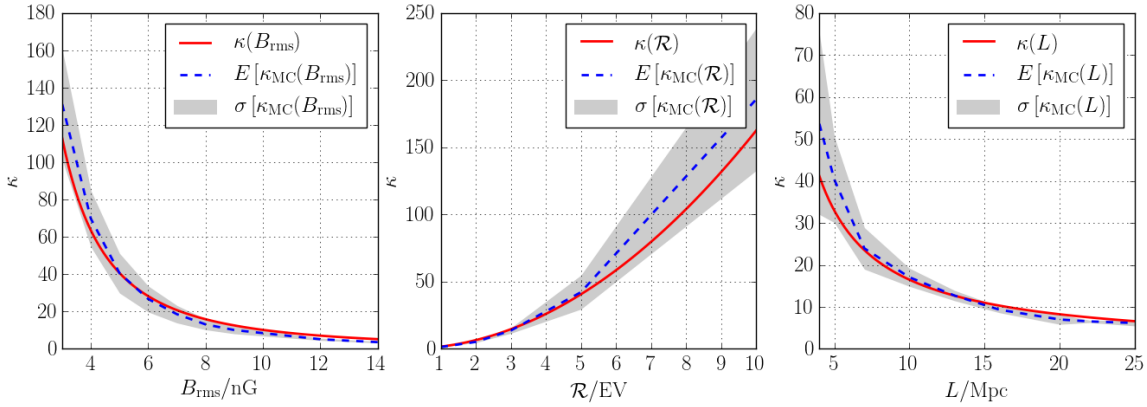

Figure 4.6: The parametrization of equation (4.17) is numerically tested for different parameters of magnetic field strength $B_{\rm rms}$, rigidity $\mathcal{R}$ and distance L separately. The red lines are calculated from the formula, while blue dashed lines are Monte Carlo results.

It is worth to note that small discrepancies and fluctuations for $\kappa > 50$ are of less importance because the anisotropic moments C_ℓ are not changing much for those values and a moderate ℓ, which is expected because large κ values, means a small deflection to which low multipoles are not very sensitive (see the derivatives in the second plot of figure 4.3).

The influence of the second nearest source

Knowing how the spread parameter depends on the distance, one can assess the validity of the starting assumption that distant sources do not sufficiently change the anisotropy created by the closest source. Introducing only two sources in an analogous manner as in equation (4.6) with different distances L_1, $L_2 = \lambda L_1$ and with spread parameters κ_1, $\kappa_2 = \kappa_1(L_1/L_2) = \kappa_1/\lambda$ respectively, the calculation from section 4.1 can be repeated. The fluxes fall as $L_{1,2}^{-2}$, hence the relative flux is $j_2/j_1 = \lambda^{-2}$ when both sources are injecting particles with the same rate. Only the dipole is calculated as the most important moment in any case. Two extreme cases are studied to preserve the axial symmetry, which simplifies the integration: a "constructive" one ($\hat{\mathbf{r}}_1 = \hat{\mathbf{r}}_2$), where the second source is behind the first one, and a "destructive" one ($\hat{\mathbf{r}}_1 = -\hat{\mathbf{r}}_2$), where the

second one is on the opposite side, relative to the observer.

$$\begin{aligned} f_{\mathrm{src}_{1,2}}(\hat{\mathbf{r}}|\lambda,\kappa_1,\kappa_2) =& f_{\mathrm{src}_{1,2}}(\hat{\mathbf{r}}|\lambda,\kappa_1) = \\ & (1-\frac{\lambda^{-2}}{2})\frac{\kappa_1}{4\pi\sinh(\kappa_1)}\exp(\kappa_1\hat{\mathbf{r}}\cdot\hat{\mathbf{r}}_1) \\ & +\frac{\lambda^{-2}}{2}\frac{\kappa_1/\lambda}{4\pi\sinh(\kappa_1/\lambda)}\exp(\kappa_1\hat{\mathbf{r}}\cdot\hat{\mathbf{r}}_2/\lambda) \\ \Rightarrow a_{10} =& \sqrt{\frac{3}{4\pi}}\left[\mathcal{I}_1(\kappa_1)-\frac{1}{2\lambda^2}\left(\mathcal{I}_1(\kappa_1)\pm\mathcal{I}_1(\kappa_1/\lambda)\right)\right] . \end{aligned} \tag{4.19}$$

By requiring $\lim_{\lambda\to\infty} C_1(\lambda,\kappa_1,\kappa_2)/C_1(\kappa_1) = 1$, the deviation from the single discrete source case can be parametrized through a parameter λ. The following solution is plotted in fig. 4.7:

$$\begin{aligned} \frac{C_1^{\mathrm{src}_{1,2}}(\lambda,\kappa_1,\kappa_2)}{C_1^{\mathrm{src}_1}(\eta=1/2\lambda^2,\kappa_1)} =& \left[1\pm\frac{\coth\left(\frac{\kappa}{\lambda}\right)-\frac{\lambda}{\kappa}}{(2\lambda^2-1)\left(\coth(\kappa)-\frac{1}{\kappa}\right)}\right]^2 \\ \approx& 1\pm\frac{1}{3\lambda^3}\left(3+\frac{1}{5}\kappa^2+O(\kappa^4)\right) \end{aligned} \tag{4.20}$$

where the last approximation is valid for $\lambda \gg 1$ and $\kappa \sim 1$.

The influence of the second source on the dipole falls with distance as $\sim \lambda^{-3}$ for a given spread parameter κ, but if the angular spread is larger (smaller κ), the decrease is quicker for both cases. Thus, for stronger magnetic fields and lower rigidities, the single discrete source assumption holds better, as expected, and the assumption is already justified if the second source is at least located at several times the distance of the first one.

Combining multiple rigidities

Up to now, calculations considered only a monoenergetic source which is injecting only a single type of cosmic rays, i.e., a single rigidity. An expansion of the analysis to multiple rigidities can be represented through a single source which is a combination of multiple sources located at the same position with a range of values for the spread parameter κ. This leads to the spectrum expressed analogously as in the previous subsection in eq.

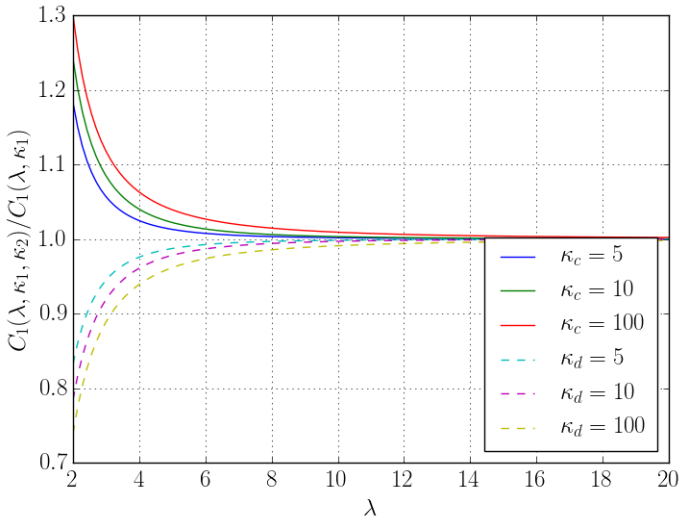

Figure 4.7: This plot shows when the dipole moment converges to the original expression given by (4.13) if there is a second source involved. Parameter λ is the ratio between the distances of the two sources - the more remote the second source is, the less it interferes with the dipole and other moments created by the first source. Two extreme cases are considered, a "constructive" one (solid lines) where the observer, the first source and the second source are located on the same line of sight in that order, and a "destructive" one (dashed lines), where the observer is located between the two sources.

(4.12):

$$C_\ell^{\text{comb}}(\kappa_1, \ldots, \kappa_N) = \frac{1}{8}\left[\sum_i^N \frac{\eta_i \sqrt{\kappa_i}}{\sinh(\kappa_i)} I_{\ell+\frac{1}{2}}(\kappa_i)\right]^2 \tag{4.21}$$

where η_i is the flux weight of the component i.

A form of eq. (4.21), where one could easily see the general behavior of the given scenario is not found but by comparing it with the solution (4.13), an important point can be made: if the two angular power spectra correspond to the same dipole, all higher multipoles of the multiple-rigidity solution will have higher values compared to the original case. Finding the dipole's value directly cannot be done analytically since $\mathcal{I}_1 = \coth(\kappa) - \frac{1}{\kappa}$ is a transcendental equation. The process comes down to finding the root of the equation:

$$\frac{1}{4\pi}\left(\coth(\kappa_0) - \frac{1}{\kappa_0}\right)^2 - C_1^{\text{comb}}(\kappa_1, \ldots, \kappa_N) = 0\ . \tag{4.22}$$

Verifying the above claim is then equal to checking if the following is satisfied:

$$\frac{C_\ell^{\rm comb}(\kappa_1,\ldots,\kappa_N)}{C_1^{\rm comb}(\kappa_1,\ldots,\kappa_N)} \geq \frac{C_\ell^{\rm pure}(\kappa_0)}{C_1^{\rm pure}(\kappa_0)} \tag{4.23}$$

which is numerically confirmed for a wide range of parameters[3], and it can also be understood physically: by knowing that $\mathrm{Min}(\kappa_1,\ldots,\kappa_N) < \kappa_0 \ll \mathrm{Max}(\kappa_1,\ldots,\kappa_N)$ sources with $\kappa_i > \kappa_0$ always exist and they contribute more to smaller scale anisotropies than the source with κ_0 (see the first plot in fig. 4.3), and therefore, the combined spectrum will necessarily have larger higher multipoles than the pure κ_0 case.

4.1.2 Comparison with structured magnetic fields

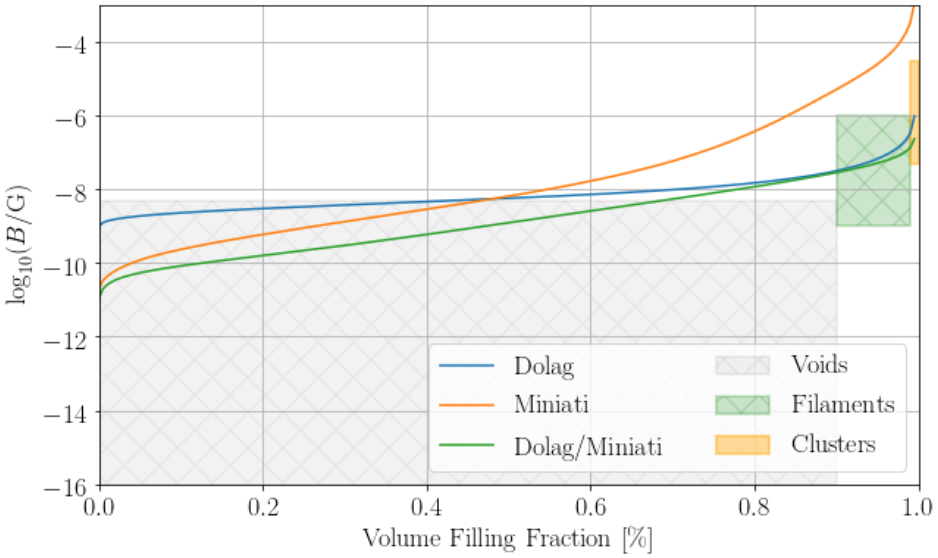

Figure 4.8: The volume filling fraction of structured magnetic field models for Dolag et al. [170], Miniati et al. [171] and the benchmark field [172].

The above-presented model follows a rather naive assumption that magnetic fields in the local Universe are everywhere uniformly turbulent only. Since galaxies, clusters, filaments, and voids contain magnetic fields which differ by several orders of magnitude in strength and other properties, it is more realistic to assume that magnetic fields are

[3]There is no reason that for some other set of parameters the inequality will not be satisfied since all components involved have a monotonic and bounded behavior. For example, see the black dotted line in the second plot of fig. 4.3.

structured, which is also backed by observations. Thus, in this section, the effects of structures on the single source model are investigated.

Nowadays, there are several structured extra-galactic magnetic field models available such as [171, 170, 173, 174]. The magnetic field that is employed, also described in detail in the CRPropa 3 reference paper [172] and referred later as the benchmark field, is constructed on the basis of the work of Dolag et al. [170] and Miniati et al. [171]. It represents a constrained model of the local large-scale structure taken from Dolag et al. on top of which is applied the magnetic field from Miniati et al., by first constructing the correlation density magnetic field within Miniati and then applying it to the Dolag density field. Within uncertainties of the void fraction in the local Universe [175], the chosen model's magnetic field strength in voids comply with the newest upper limits, such as from the ESA Planck experiment [176]. This can be seen in fig. 4.8, in which a volume filling fraction of the mentioned models is displayed. The volume filling fraction represents a binning of volume blocks dV according to their averaged magnetic field strength values. However, the more important component to compare here is the structure of the magnetic field itself, not its strength. The magnetic field structure of the benchmark field in the form of a strength distribution is shown in fig. 4.9. Furthermore, two distinct locations for the observer have been investigated: the first one located within structures, which resembles the local Universe around the Milky Way; and the second one is placed in a void at least 5 Mpc from the nearest structure (fig. 4.9).

The simulation scenario consists of iterating a single source over 80 uniformly distributed locations on a sphere of radius 5 Mpc and 10 Mpc around the observer. The observer sphere has a radius of 400 kpc. The energy range of the particles is chosen such that the angular spread ranges from $\kappa \approx 1$ to $\kappa \approx 10$, which is the range where the effect of the structure in the angular distribution is most easily seen in the context of this investigation, namely around 10 EeV. The other parameters are kept the same as in the turbulent case. At least one thousand events are collected from every source. The results are shown in fig. 4.10 in the form of the retrieved values of κ. The spread

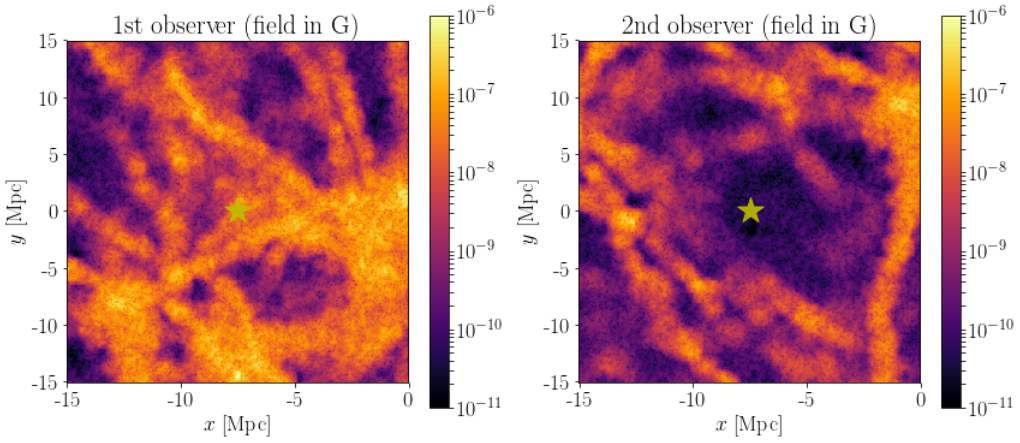

Figure 4.9: Two distinct locations for the observer are chosen: the first one within structures that is also constrained to resemble the local Universe around the Milky Way; and the second one is placed in a void at least 5 Mpc from the nearest structure. The colour scale represents the magnetic field strength. The shown magnetic field comes from the benchmark model described in the text.

parameter of all sources in the first location, within structures, is $\kappa_1^{5\,\mathrm{Mpc}} = 2.9 \pm 0.8$ and $\kappa_1^{10\,\mathrm{Mpc}} = 2.0 \pm 0.5$ for sources at 5 Mpc and 10 Mpc distance, respectively. In the second location, within the void, the values are $\kappa_2^{5\,\mathrm{Mpc}} = 22 \pm 14$ and $\kappa_2^{10\,\mathrm{Mpc}} = 7 \pm 4$.

In a structured magnetic field, it is not possible to unambiguously define physical parameters in the whole space, such as B_{rms} that determines the spread parameter κ, as in the case of a turbulent field, i.e., equation (4.17). However, it is possible to investigate how much the shape of the angular power spectrum is altered compared to the expected analytical solution given by eq. (4.13). To achieve this, the value of κ is determined from the dipolar moment obtained from the simulation, and then, the next most robust large-scale moment, the quadrupole, also obtained from the simulation, is compared against the expected value calculated from κ by eq. (4.13). Therefore, the ratio of these two quadrupole values, the purely turbulent obtained analytically and the one obtained from the simulation with the structured field, can be established by taking the relative difference $(C_2^{\mathrm{MC}} - C_2^{\mathrm{AN}})/C_2^{\mathrm{AN}}$ (figure 4.11). It can be observed in which directions the original pattern expected from equation (4.13) (figure 4.3) is the least affected by the structures. In the void, the pattern is conserved the best, which has been expected, but for larger distances where new domains of the magnetic field emerge this picture is disturbed. For the observer in the structured part of the Universe, the pattern is mostly

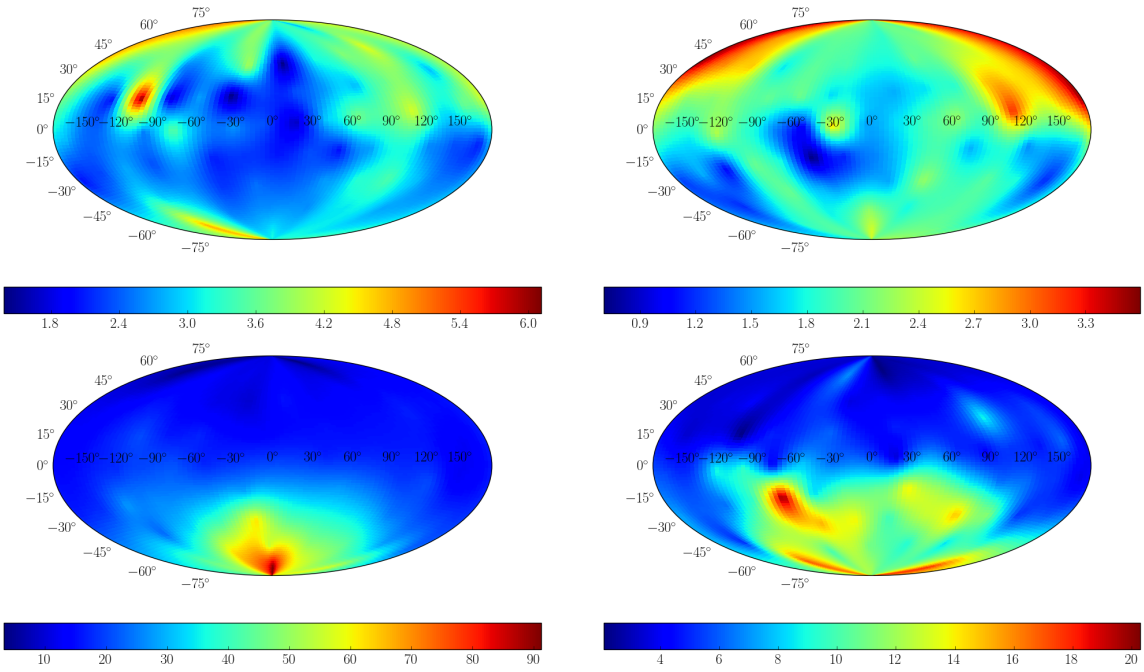

Figure 4.10: These four skymaps interpolate values of κ from 80 uniformly distributed sources in four cases (the colour scale represents the value of κ): the upper two represent skymaps for the first location of the observer (within structures) where sources are at 5 Mpc (left) and 10 Mpc (right), while the bottom two represent skymaps for the second location of the observer (in the void), also at the same distances as the upper two. Average values are $\kappa_1^{5\,\mathrm{Mpc}} = 2.9 \pm 0.8$, $\kappa_1^{10\,\mathrm{Mpc}} = 2.0 \pm 0.5$, $\kappa_2^{5\,\mathrm{Mpc}} = 22 \pm 14$ and $\kappa_2^{10\,\mathrm{Mpc}} = 7 \pm 4$. The angular spread depends on the direction, but generally the same quantitative behavior is preserved: the stronger magnetic field (1st location, upper row) causes the larger angular spread (smaller κ). The same holds for greater distances from the sources (right column). The structure of the magnetic field around these locations is displayed in the previous figure (4.9).

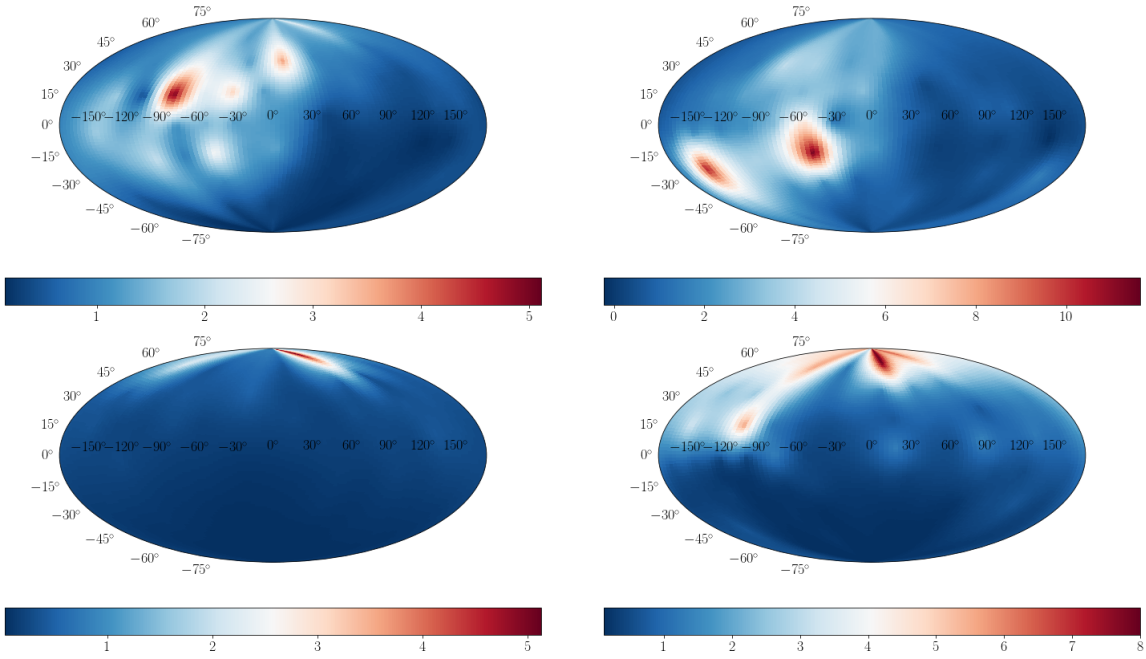

Figure 4.11: This figure describes the same cases as the previous figure 4.9, but it shows the relative difference in the quadrupole component between the simulation and the analytical expression, $(C_2^{\mathrm{MC}} - C_2^{\mathrm{AN}})/C_2^{\mathrm{AN}}$, which is represented by the colour scale. The smaller the difference, the better the original pattern (figure 4.3) reproduced, e.g., the better it resembles the pure turbulent case. Red spots are areas where the structured magnetic field changes the expected ratio between the dipole and quadrupole moment the most. It should be stressed that in all such cases the quadrupole to dipole ratio tends to be larger than predicted for purely turbulent fields.

distorted on the edges between two different domains of high and low angular spread, which can be seen by comparing figures 4.10 and 4.11. In areas where the pattern is distorted, the predicted single source signature is basically lost since different moments are modified differently, yet, it should be stressed that, in all such cases, the effect of structures increased the quadrupole component compared to the dipole component relative to the analytical expectation.

A qualitative description of the phenomena can be phrased in the following way. Generally, a structured magnetic field can be characterized by the existence of separate domains which have different field properties and spatial sizes, therefore, these domains contribute differently to cosmic ray deflection, that is, they have different values of κ. If the source and the observer are located within the same domain, the described pure turbulent field approach can be applied, but if cosmic rays from the source traverse different domains to reach the observer, each domain can be considered as an independent source located at the same position as the real source but with an independent angular spread, which leads to a power spectrum of the same form as eq. (4.21). As was already shown in subsection 4.1.1, the values of higher multipoles will increase when combining sources of different κ compared to the pure turbulent case. Summarizing the argument, the structured magnetic field tends to enhance higher multipoles of the angular power spectrum compared to the analytically obtained reference spectrum, and, hence to increase the ratio $C_{\ell+1}/C_\ell$.

In domains where the assumption of traversing multiple coherence lengths is not fulfilled, cosmic rays can create distinct structured patterns like creating mirror images [149], which will considerably affect the argument. Similar effects will occur if regular components of the magnetic field dominate turbulent ones in those domains. Every systematic shift of the arrival directions caused by the regular components of magnetic fields will distort the Fisher distribution. Considering those scenarios is beyond the scope of this work. It can only be added that smaller structures in the Universe are expected to have a smaller coherence length of their associated turbulent component, like in our Galaxy where $L_c \leq 100\,\mathrm{pc}$ [177]. Smaller coherence lengths of smaller structures

make the systematic shift in the arrival directions less probable, i.e., their directions are in every domain randomised. That makes an objection to not traversing multiple coherence lengths less relevant.

4.1.3 Examining constraints from the measured dipole and quadrupole and potential neighbouring sources

The Pierre Auger Observatory reported a dipolar amplitude of $d = 6.5^{+1.3}_{-0.9}\%$ above 8 EeV [105] while higher moments remain within 99% confidence level of isotropy [105]. To derive values of C_ℓ with the correct normalization in the monopole component C_0 for the Auger data, following the expression from [178], is used: $\Phi(\hat{\mathbf{n}}) = \frac{\Phi_0}{4\pi}(1 + \mathbf{d} \cdot \mathbf{n})$. Putting it in eq. (A.16), one gets $C_1/C_0 = |\mathbf{d}|^2/9 = (0.00047^{+0.00019}_{-0.00013})$. As already noted in section 4.1, equation (4.14) serves to constrain the model's parameters from the dipole amplitude. The result is displayed as the solid blue line, together with the associated uncertainties as the dashed blue lines, in figure 4.12. Employing the estimated value of the quadrupole moment from the Pierre Auger experiment with the upper normalization $C_2/C_0 = (1 \pm 0.5) \times 10^{-4}$ [179], the model gives the solution $\kappa = 2.7^{+1.2}_{-1.1}$, $\eta = 0.03 \pm 0.01$ where uncertainties are obtained from the experimental uncertainties of C_1 and C_2 by integrating out either η or κ. The shaded areas in figure 4.12 (orange for one sigma and yellow for two sigmas) represent the propagated confidence ranges for every η and κ.

Large uncertainties are the consequence of the large derivatives of the solutions from equation (4.14) in the regime of small κ (see the derivatives in the second plot of figure 4.3) combined with the large experimental uncertainties in the large-scale anisotropy sector. The large experimental uncertainties are caused firstly due to low statistics at the highest energies, and secondly due to the limited coherent full-sky coverage [96]. In the current full-sky analysis [97], uncertainties in systematics between the two largest experiments, Telescope Array and Pierre Auger Observatory, prevent more precise results than those obtained by reconstructing the large scale anisotropies from partial sky coverage of a single experiment.

The retrieved κ is bigger than 1, which guarantees that the small angle approxi-

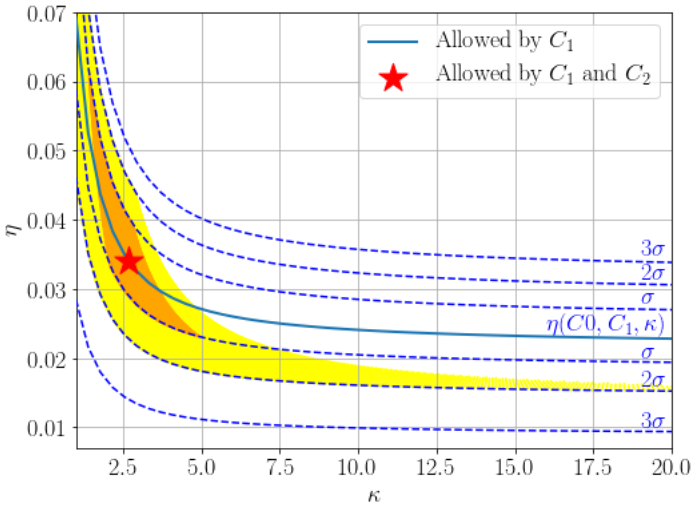

Figure 4.12: The plot shows how the Auger dipole and quadrupole above 8 EeV constrain the space of parameters η and κ. The solid blue line is the result if only the dipole is considered, while dashed lines are the associated uncertainties. If the quadrupole is taken into account, there is one possible solution (given by equations (4.14) and (4.15)) marked with a star and corresponding to one, and two sigmas shaded areas (orange and yellow respectively). From the plot, it can be concluded that, if the anisotropy is caused by a single source, a significant angular spread (small κ) is favoured, which almost completely erases C_ℓ with $\ell > 2$. The significant angular spread also implies larger than expected deflection at the given energies and composition in typical magnetic field models (see equation (4.17) and also the next figure).

mation can be used, thereby, $\mathcal{D}_0^{\rm ql} L$ follows from eq. (4.16) and the root mean square angular spread $\alpha_{\rm rms}$ from (4.17):

$$\mathcal{D}_0^{\rm ql} L = 0.56^{+0.25}_{-0.22} \ , \quad \alpha_{\rm rms} = \left(50^{+11}_{-10}\right)^\circ \ . \tag{4.24}$$

The parameters derived above imply angular spreads considerably larger than what the usually considered physical values in equation (4.17) give. The significant angular spread reinforce the single source approximation as the influence of the second nearest source falls rapidly with distance (see eq. (4.20) and fig. 4.7). However, if one takes into consideration the results from sections 4.1.1 and 4.1.2, which tend to increase higher moments compared to the dipolar moment, and hence to increase the ratio C_2/C_1, the observed dipolar amplitude would impose more stringent conditions on κ and η. If the flux from which the dipole is reconstructed is composed of multiple rigidities – which is almost certainly true – and if cosmic rays traverse domains of a structured

magnetic field – which also is realistic – the single source model would predict an increase of the expected ratio C_2/C_1. This increases the expected value of κ compared to the simpler case, and consequently, the observations realistically require even more significant angular spreads. Or, to put it differently, if the measured anisotropies are originating from a single source and the quadrupole component is increased compared to the dipole component due to a mixed composition and a structured magnetic field, the consequence is that an even smaller κ is required by the observations.

By using the solution (4.13) for $\ell = 1$ and the parametrization (4.17) to express the dipole amplitude $d = \sqrt{9C_1/C_0}$ as a function of rigidity $\mathcal{R}$, one gets:

$$d(\mathcal{R}) = 3\eta \left(\coth \kappa - \kappa^{-1}\right) \approx 3\eta \left[\coth\left(\frac{\kappa_0}{\mathcal{R}_0^2}\mathcal{R}^2\right) - \left(\frac{\kappa_0}{\mathcal{R}_0^2}\mathcal{R}^2\right)^{-1}\right] \tag{4.25}$$

where κ_0 and $\mathcal{R}_0$ are fixed by the dipole measured in the energy bin centered at 11.5 EeV. An immediate consequence is that the dipole amplitude should increase at higher energies. The plot of the function and the Auger dipolar amplitudes for 4-8 EeV and 8+ EeV bins can be seen on fig. 4.13. The measured dipole amplitude in the 4-8 EeV range is in agreement with the derived result. The composition data from the Pierre Auger Observatory [93] suggests a change in the average composition at the end of the spectrum towards heavier nuclei when the fit of the EPOS-LHC hadronic model to the shower data is employed. Here, the composition is simplified to the average $\langle Z \rangle = \sum_{i=\mathrm{p,He,N,Fe}} f_i Z_i$ per energy bin, or approximated with $\langle Z(E) \rangle = 4 + 0.1 \frac{E}{\mathrm{EeV}}$. When this dependence is inserted in $\mathcal{R} = E/\langle Z(E) \rangle$, the dipole amplitude at higher energy bins is slightly suppressed compared to the prediction without this dependence. Other hadronic models from [93] reduce this difference since they predict a more uniform composition in this energy range.

In the field of ultra-high energy cosmic rays, two nearby extra-galactic objects often considered as potential sources of these cosmic rays are Centaurus A [180] and the Virgo cluster [181, 157]. This conclusion comes from the reasoning that if our galaxy does not contain known accelerators which are capable of achieving energies above 8 EeV [180], it

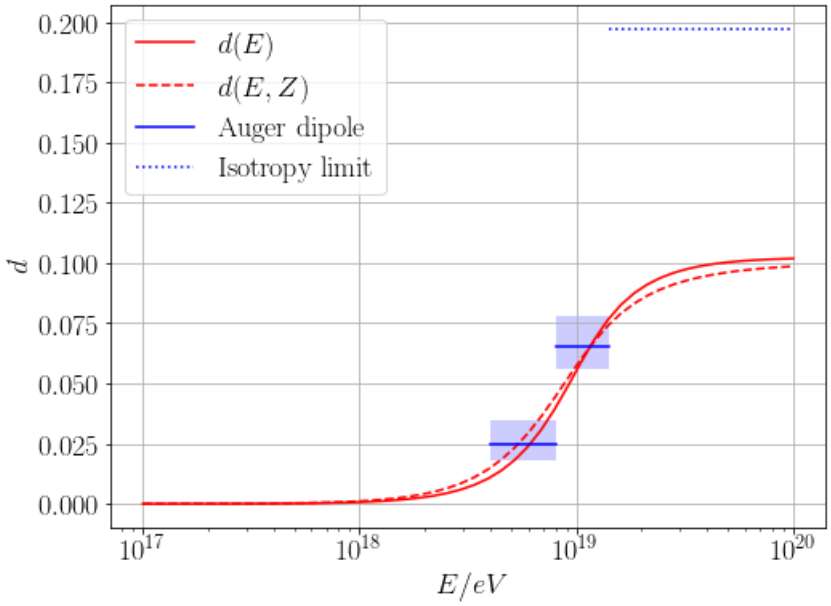

Figure 4.13: This is a comparison of the model's result for the dipole with measured dipole amplitudes at two different energy ranges taken from [105] by using (4.25). Equation (4.25) with κ_0 and η_0 determined by the measurement at 11.5 EeV is plotted as the solid line. The resulting prediction of the dipole at the lower energy range is consistent with the measured dipole in the 4-8 EeV bin. The dashed line represents a correction in the dipole amplitude $d(Z)$ when the changing average composition $\langle Z(E)\rangle$ at higher energies is taken into account. This shows that the measured composition indications slightly suppress the dipole amplitude at the higher energies, while negligibly amplifying it at lower energies. The dotted line is a dipole average of the isotropic distribution in the case of full-sky coverage when roughly the total number of events detected by PAO, $N \approx 200$, above $10^{19.5}$ eV [93] is inserted in $d = \sqrt{9\langle C_1\rangle_{\rm iso}/C_0} = 3N^{-1/2}$ [96].

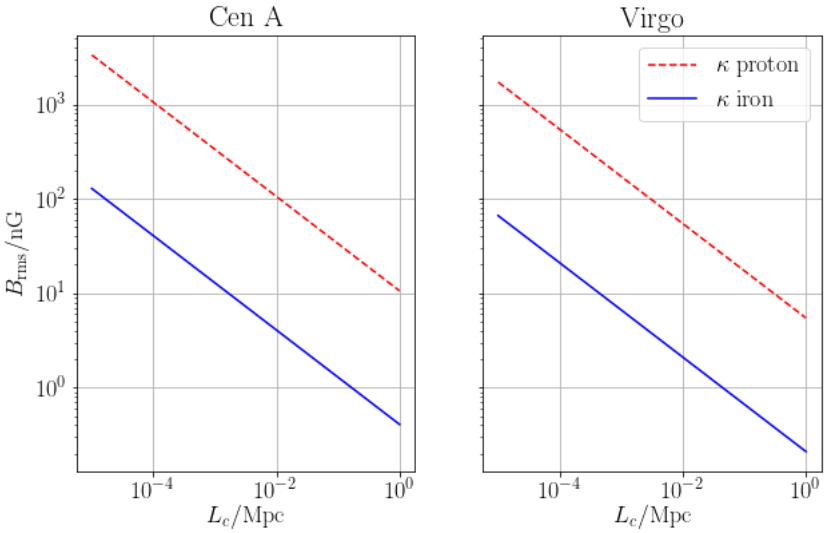

Figure 4.14: For a source of a given distance, the remaining parameters left undetermined are the charge, the magnetic field strength and the coherence length. The plot shows the relation between $B_{\rm rms}$ and L_c following from eq. (4.17) for the fitted value of κ, for proton and iron primaries coming from Centaurus A and the Virgo cluster.

follows that ordinary galaxies cannot produce UHECRs either. Therefore, radio galaxies or rich clusters of galaxies are more likely to contain UHECR sources. The radio galaxy Centaurus A and the Virgo cluster are the two closest of this kind. The distance from Cen A is 3.8 Mpc [182] and from Virgo is 16.5 Mpc [183].

Putting their distances into eq. (4.17) and using the constraints from the previous paragraph, the quantity $Z^{-2}B_{\rm rms}^{-2}(L_c)^{-1}$ is constrained. This can be seen in figure 4.14 where two limiting cases, hydrogen and iron, are shown.

To verify our analytical approximation, a CRPropa simulation was performed based on the obtained parameters from above, η, κ, and the parametrization given in eq. (4.17). The simulation consists of a single source at 4 Mpc distance which injects monoenergetic iron nuclei (Z=26) at 11.5 EeV, a turbulent magnetic field with spatially homogeneous structural properties and coherence length of 30 kpc which fixes the magnetic field strength to $B_{\rm rms} = 2.9\,\text{nG}$. Additional $[(1-\eta)/\eta]\,N_{\rm single}$ events are injected isotropically to represent the background component. In total ~ 17000 events are detected (of which $N_{\rm single} \simeq 1900$ are from the single source) in a series of ten realisations with the observer defined as in sec. 4.1.1. The dipole is fitted to the

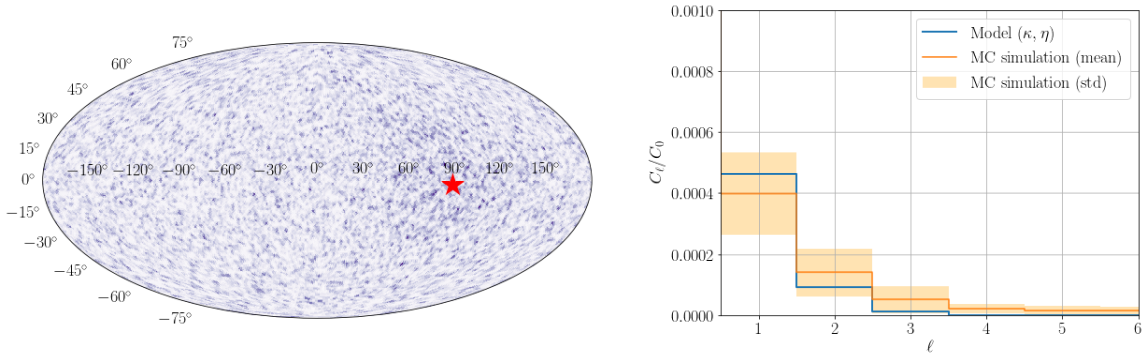

Figure 4.15: The two plots are results of a Monte Carlo simulation, which is set up as described in the text. The sky plot shows the dipole induced by the single source that is placed at 4 Mpc distance from the observer. The direction of the dipole is marked with a star. The other parameters are $Z = 26$, $E = 11.5EeV$, $B_{\rm rms} = 2.9\,{\rm nG}$, $L_c = 30\,{\rm kpc}$, $\eta = 0.03$ where $(1 - \eta)$ is the isotropic contribution from the background. The right panel plot depicts the first few moments of the angular power spectrum where the blue line is the analytically calculated spectrum by using the spread parameter (κ) and the relative flux (η), while the orange line is a fit from the simulation. The orange shaded area represents one sigma fluctuations.

resulting sky map using the healpy library [184] which reproduced the targeted amplitude $d = (0.061 \pm 0.006)\%$ and the corresponding large-scale multipoles, namely $C_1 = 0.005 \pm 0.001$ and $C_2 = 0.0014 \pm 0.0004$, within the numerical fluctuations caused by differences in the realisation of the magnetic field, randomness in the isotropic injection and the variation in picking events from CRPropa's ParticleMap container (see fig. 4.15).

4.2 Clustering of many sources

The Pierre Auger Collaboration in its paper about the dipolar anisotropy [105] suggests that the dipole could originate from the 2MRS[4] dipole [185], although it is shifted by 55° away from it and that could, in principle be due to the galactic magnetic field.

The presented results of the single source model can be roughly re-examined in a new context of multiple sources grouped in a certain part of the sky. For simplicity, this grouping can be depicted as a circle of radius r at a distance L from the observer. The quantity of interest here is only the ratio between the spatial spread r and the

[4]The 2MRS catalogue is a redshift survey from the 2MASS (Two Micron All Sky Survey) catalogue [109] which maps the distribution of galaxies in the local Universe observed in the near infra-red spectrum.

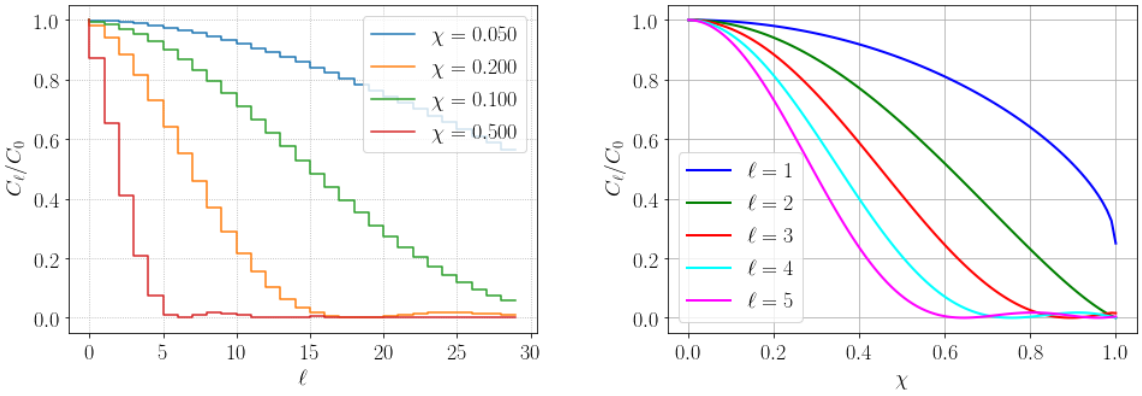

Figure 4.16: Plot of the angular power spectrum given by eq. (4.26), where χ is the ratio between the size of the cluster and the distance from the cluster.

distance $\chi = r/L$. When $\chi \to 0$, the scenario can be approximated as a single source. In the opposite case, the cluster of sources can be interpreted in terms of the finite-size observer problem presented in appendix B.3, although now this is not a technical issue, but rather a physical reality. The angular power spectrum is given by the following expression, calculated in appendix A.1:

$$C_\ell = 2^{2\ell}\pi \left[\sum_{k=0}^{\ell} \binom{\ell}{k} \binom{\frac{\ell+k-1}{2}}{\ell} \frac{1}{k+1} \left(1 - \left(1 - \frac{r^2}{L^2}\right)^{(k+1)/2}\right)\right]^2 . \tag{4.26}$$

This equation is plotted in fig. 4.16 in analogy to fig. 4.3: on the left panel C_ℓ/C_0 versus ℓ for different χ, and on the right panel C_ℓ/C_0 versus χ for some first few ℓ. The behaviour of the angular power spectrum when the angular spreading and the isotropic background are included roughly follows the single source model, which means that the deflections of cosmic rays are lowering higher moments more, thus increasing ratios between multipoles, like the C_2/C_1 considered above. It can be concluded that a spatially extended source, like a cluster of sources, would act in the same way as the deflections in turbulent magnetic fields, and thus relax constraints on the deflections, i.e., when $\chi \to 1$, the requirement for the deflection α_{rms} would be smaller.

4.3 Summary

This chapter analysed a scenario where only a single source of cosmic rays contributes to the anisotropy, while other sources are treated as an isotropic background which gives only a fraction of the total flux given by η. The arrival directions of cosmic rays that originated from a single source are assumed to be distributed following the Fisher distribution with the concentration parameter κ, which encodes the angular spreading. This is argued by recalling from the previous chapter that cosmic rays are performing a random walk in flight directions, which leads to a Brownian motion distribution on a sphere, and it can be approximated with the Fisher distribution. The isotropic background is added as a constant term in the distribution. The distribution, through the analytically obtained angular power spectrum, is then related to physical parameters which are responsible for the deflections in the regime of the small angle approximation introduced in sec. 3.4.1.

A short investigation of the influence of a structured magnetic field is conducted in sec. 4.1.2. Monte Carlo simulations were then performed in which cosmic rays got forward tracked from a single source in different parts of the magnetic field crossing various structures. From the analysis of the results, it was concluded that structured magnetic fields generally tend to increase smaller anisotropies compared to the dipole, reducing the ratio between them that was introduced by a single source.

The single source model is then confronted with observational data. By plugging in the amplitude of the dipolar anisotropy measured by the Pierre Auger Observatory and the estimated value of the quadrupole component, the parameters of the model were obtained, namely, $\kappa = 2.7^{+1.2}_{-1.1}$, $\eta = 0.03 \pm 0.01$, which showed that the ratio of a neighbouring source for the given parameters should be contributing with $\sim 3 \pm 1\%$ compared to the total flux. The value of the concentration parameter, also called the spread parameter, although implying considerable deflections, at the same time guarantees that the propagation still falls under the small angle approximation, thus physical parameters were calculated from it. The obtained root mean square deflection angle is

$\alpha_{\rm rms} = \left(50^{+0.11}_{-0.10}\right)^{\circ}$. The obtained deflections affect other more distant sources as well. If their distance is only ~ 5 times the distance of the first source from the observer, they influence the first source dipole by less than 5%, and higher multipoles even less, thus they contribute to the arrival directions almost isotropically and most of the information about their position is practically lost (see eq. (4.20) and fig. 4.7). In contrast, sources at similar distances from the observer invalidate the starting assumption of a single isolated source, which would require a different analysis. Furthermore, the robustness of the analysis is confirmed in a study of the dipole amplitude dependence on energy 4.25, which shows an agreement with the measured dipole amplitudes at different energies. Finally, by assuming that the source could be Cen A or the Virgo Cluster, the constraints were put on the ratio of the magnetic field strength and its coherence length for the proton and iron composition (fig. 4.14). This suggests that if the magnetic field is weaker than 1 nG in case of iron nuclei, or 10 nG in case of protons, for the coherence length of the field ≤ 1 Mpc, it is likely that there is no single luminous source in the vicinity of the Milky Way, such as Centaurus A or Virgo cluster.

In the last section, a short discussion about a spatially extended source is given. The spatially extended source could be a cluster of galaxies or any other grouping of sources that can be approximated as a wider area that inject sources. The message is that by spatially expanding the size of the source relative to the distance from the observer, the constraints of the original single source model on the deflections are reduced.

5 | Effects of magnetic fields on anisotropies

As it was mentioned in the introduction, in the context of arrival direction anisotropies, one in principle cannot decouple the influence of cosmic ray source distributions from the influence of intervening magnetic fields. Yet, to develop a better understanding of the anisotropy origin, one has to resort to studies of special or limiting case scenarios where the focus is mainly on one aspect of the phenomenon. Unlike the previous chapter, where the emphasis was on source distributions in which magnetic fields played the simple role of spreading the arrival directions, this chapter is devoted to an investigation of how magnetic fields affect anisotropies in a more complex manner. Source distributions are of less importance here.

Unfortunately, due to the vast amount of unknowns, the analysis of a single particle movement in the Universe is not possible, and one cannot hope to find an exact description of the particle's dynamics. Hence, methods of statistical mechanics employed on the particles' trajectories represent a decent compromise, although it is decent only under the assumption that magnetic fields, which shape those trajectories, are predominantly in the stationary state, at least on timescales of propagation.

One of the major pillars of the statistical mechanics' framework is Liouville's theorem. Liouville's theorem has a profound impact on the propagation of cosmic rays through magnetic fields, and the investigation of the theorem's applicability to the cosmic ray propagation and anisotropies has a central role in the study of this chapter. The author of this work finds the subject of Liouville's theorem in some sense complex

and debatable, or at least not easy to comprehend in all aspects. The reason for this is probably due to the non-intuitive consequences that Liouville's theorem imposes on anisotropies, but also to the poorly known soundness of its assumptions in this given context. The common statement of its application is, to cite for example [10], "if the flux of extra-galactic cosmic particles is isotropic outside of the galaxy it has to be isotropic on Earth"; or any equivalent statement that isotropy "outside" means automatically isotropy "inside" since magnetic fields only cannot introduce anisotropies in the first place. The fact that this is not easy to grasp is proved by many dedicated studies and discussions on this issue, especially popular in the physics of the magnetosphere, for example, see discussions in [122] where even experts in the field of geomagnetism dare to ask questions about it, such as "Doesn't the result - that an isotropic equatorial distribution implies isotropy everywhere - have to break down somewhere?" Also recently, some authors tried to find an exception of it in special contexts, like streaming instabilities in the heliosphere [186], while others counter argue them [103].

Under the umbrella of numerical cosmic ray propagation, this question is of great importance, especially in a commonly used method – the backtracking of particles. In the backtracking simulation, anti-particles are propagated backwards to obtain trajectories of *regular* particles that would normally reach the observer. On the opposite to the forward tracking method, the backtracking is far more efficient since only the observed particles are propagated. Moreover, in it, the issue of the finite-size observer (see B.3) does not exist at all. However, the main disadvantage is that it cannot take into account stochastic energy loss processes as they are fundamentally irreversible in time. Therefore, in scenarios where energy losses can be neglected, like in the case of galactic propagation, the backtracking method is frequently the method of choice. The implicit assumption of the backtracking method is that cosmic rays obey Liouville's theorem, and without it the reversibility of the propagation would not hold.

The forward tracking method is also concerned with this theorem, but on a deeper level. Monte Carlo simulations are not a truthful representation of the real Universe as they always suffer from finite event statistics and the finite numerical precision, and

thus, cannot fill particles' phase space in the continuous limit, which would be required for the machinery of statistical ensembles to work. This discrepancy is maybe evident the most in a so-called trapping mechanism, which will be explained later in this chapter.

5.1 Liouville's theorem and cosmic rays

Before stating Liouville's theorem, one additional assumption should be clarified. Besides the magnetic field stationary condition requirement, the next important assumption when employing statistical methods in the trajectory analysis is that particles do not interact with each other. Omitting mutual interactions can be argued by reading off the spatial particle density from the all-particle spectrum shown in section 2.5. The isolated particles imply that every trajectory can be considered as an ensemble member by itself, like in the case of an ideal gas. Consequently, phase space is then just 6-dimensional, that is, three dimensions for the particle's momentum and three dimensions for the particle's position.

If the system in question is Hamiltonian, which a charged particle in a magnetic field under governance of the Lorentz force (3.6) certainly is, as stated in chapter 3, it evidently satisfies the Hamiltonian equations [187]:

$$\dot{q}_i = \frac{\partial H}{\partial p_i}, \quad \dot{p}_i = \frac{\partial H}{\partial q_i} \tag{5.1}$$

where q_i refer to coordinates and p_i to momenta, then the density of the ensemble members defined as $f = \mathrm{d}N/\mathrm{d}q\mathrm{d}p$ in phase space is conserved:

$$\frac{\mathrm{d}f}{\mathrm{d}t} = 0\,. \tag{5.2}$$

Since the same holds when the momentum is substituted with the canonical momentum Π, Liouville's theorem can be applied also in the case of the canonical phase space of a single charged particle $\mathrm{d}f^*/\mathrm{d}t = 0$, where $f^* = \mathrm{d}N/\mathrm{d}q\mathrm{d}\Pi$. Finally, it can be shown that the Jacobian of the transformation to the ordinary phase space is unity [188, 122].

In a more concrete sense, if P and P' denote two points on the dynamical trajectory of one particle, then the theorem states that the density, $f(P) = f(P')$, is conserved along a dynamical trajectory. The total time derivative in eq. (5.2) should be read as the derivative taken at the position of a moving particle.

In practice, that means that a unidirectional detector with an infinitesimal cross-section detects a number of particles per unit time $\mathrm{d}t$, per unit solid angle $\mathrm{d}\Omega$, per unit energy $\mathrm{d}E$, per unit area $\mathrm{d}A$, or just detects the intensity of particles j, and that is obtained from the phase space density f:

$$\begin{aligned} j &= \frac{f(\mathbf{x},\mathbf{p})\mathrm{d}\mathbf{x}\mathrm{d}\mathbf{p}}{\mathrm{d}t\mathrm{d}E\mathrm{d}A\mathrm{d}\Omega} \\ &= f(\mathbf{x},\mathbf{p})\frac{r^2\mathrm{d}r\mathrm{d}\Omega\mathrm{d}p_r p_r^2\mathrm{d}\Omega}{\mathrm{d}t\mathrm{d}E\mathrm{d}A\mathrm{d}\Omega} \\ &= f(\mathbf{x},\mathbf{p})v\frac{r^2\mathrm{d}p_r p_r^2\mathrm{d}\Omega}{\mathrm{d}E r^2\mathrm{d}\Omega} \\ &= f(\mathbf{x},\mathbf{p})p_r^2\frac{v\gamma m}{p} = p_r^2 f(\mathbf{x},\mathbf{p}) \end{aligned} \tag{5.3}$$

where in the last step $\mathrm{d}E = \frac{p}{\gamma m}\mathrm{d}p$ was used. Liouville's theorem states in this case that the intensity j has the same value if one follows a point on a dynamical trajectory. Or if one assumes a constant flow of particles on a given trajectory, the detector can stay in a fixed point of space to detect the constant intensity, or, alternatively, the intensity is constant at each point of the trajectory.

This, however, does not generally apply to a broad angle detector as James Van Allen wrote in [122]: "A practical point to remember in the use of Liouville's theorem is that a detector having an infinitesimal cross-section and solid angle must be used. A broad angle detector will intercept rays with different dynamical traces having come from distinct dynamical regions. Liouville's theorem of course does not apply to a mixture like this and use of the theorem can be a great pitfall."

Originally, the theorem was applied first in the context of cosmic rays and the latitude effect. Lemaître and Vallarta [189] stated that if one assumes a homogeneous and isotropic distribution at infinity, the intensity in all allowed directions at any point is the same. The concept of allowed, and its opposite, forbidden, directions respectively

mean that a magnetic field may allow or prohibit cosmic rays from reaching a certain point from a certain direction. To find out if a direction is allowed or forbidden one would have to trace back the trajectory associated with this direction and look at whether the trajectory ends up at infinity, where the homogeneous and isotropic distribution has been defined, and if does, that would be counted as an allowed direction. In the case of a forbidden direction, the backtracking would reveal that the orbit is periodic. A periodic orbit is obviously forbidden because a single particle that is following this orbit cannot pass through the detector and be detected twice or more.

When Earth's magnetic field, which can be approximated as a magnetic field of a dipole, is considered, some directions are prohibited. These are those whose trajectories can be traced back to the Earth's surface. As Clay and Compton observed [37, 38], the intensity of cosmic rays (of certain energy range) drops sharply on latitudes south of $\sim 34^\circ$ on the north, and north of $\sim 34^\circ$ on the south, and in between is located the magnetic equator where the intensity is minimal. Complete derivations of these phenomena can be found in a pioneering work of Carl Störmer, in his study of charged particle trajectories in the presence of a magnetic dipole, summarised in his book The Polar Aurora [190]. One could illustrate the latitude effect as the shadow of the Earth since the trajectories of forbidden directions are intersected by the planet itself.

If the conclusion of the latitude effect is generalised, the periodic orbits could be looked elsewhere, in other magnetic fields, such as in the solar magnetic field or the galactic magnetic field. Near the solar surface the same argument can apply, due to the shadow of the sun, but looking further away there is no experimental evidence of any forbidden directions and zones without cosmic rays. The reason why cosmic rays are isotropic everywhere else besides in the Earth's case could be given as follows. First, there is no solid obstacle big enough that could shadow a region of space enough to be evident. But should there still be plenty of periodic orbits which could be unpopulated in the first place and which could have the intensity zero? The answer is no if the scattering is brought into the picture. It was described in chapter 3 that due to irregularities in magnetic fields particles are scattered, which also happens if one takes into account

energy losses or the solar wind, or any other mechanism that can change the orbits of particles switching them between the orbits of allowed and forbidden directions. In that way, particles would fill up the periodic orbit, and eventually, the stationary state between the periodic orbits and those that lead to infinity would be established, and isotropy would be restored everywhere. Therefore, there are no forbidden orbits in the solar field, and then probably not at larger scales, like in the galactic field due to all these processes [113]. This is called the isotropisation argument.

5.2 Trapping of cosmic rays

The work of Lemaître and Vallarta has been criticised already by Störmer [191] in 1934 on several points. One of these was an objection to Lemaître and Vallarta making the argument about asymptotic orbits rather trivial, while those asymptotic orbits *require a detailed study of the shape of all the orbits from infinity as a function of their initial conditions*. The point is that orbits never extend simply to infinity, but, depending on which paths they are taking through a magnetic field, some of them could be significantly longer compared to others. Particles that are channelling on those trajectories are trapped in practical terms. In Monte Carlo simulations of propagation, that means that some maximum trajectory length defined within the simulation will be reached and that trajectory will be deleted making, from an allowed direction, a forbidden one. That eventually can cause anisotropies. In the real Universe, particles first do not propagate in infinite time, and secondly, they interact and change their properties, such as energy and composition through energy loss processes (see fig. 4.1). Of course, Liouville's theorem assumes no change in energy; thus if this is violated, it does not apply to this case. However, the argument of isotropisation at a practical "infinity" given above also violates that assumption, although in favour of the argument. Hence, the same assumption is violated, on both sides, for and against the application of Liouville's theorem on conserving the isotropy. The only question is which violation of those two occurs sooner. If the isotropisation is the quicker one, the practical "infinity" will be very close, and no significant trapping will happen. On the other hand, if the trapping

is the dominating process, the anisotropy will appear albeit in "infinity" a homogeneous and isotropic distribution is present.

A rough estimate of the effect can be summarised for the case of a turbulent magnetic field as follows. If the observer is located on the border of two domains of a structured magnetic field with different properties, then, under the small angle approximation, equation (3.71) gives an averaged trajectory difference between similar particles arriving from the same distance across those two domains:

$$\Delta L \approx \frac{1}{3} L^2 \left(\mathcal{D}_0^a - \mathcal{D}_0^b \right) = \frac{1}{24} \mathcal{R}^{-2} L^2 \left[\left(L_c B_{\mathrm{rms}}^2 \right)_a - \left(L_c B_{\mathrm{rms}}^2 \right)_b \right] \tag{5.4}$$

where $\mathcal{D}_0^a$ and $\mathcal{D}_0^b$ are diffusion coefficients in the flight direction associated to the domains a and b. In the parentheses the associated coherence lengths and root mean square strengths of turbulent components in those domains are given.

Here is one case was given to demonstrate the argument.

5.2.1 Structured magnetic field

In a forward tracking simulation of a scenario in which a structured magnetic field is set while 10 EeV mono-energetic iron particles are injected homogeneously and isotropically, the large-scale anisotropies can appear depending mostly on the location of the observer within the structure. The structured magnetic field model used here is already described in sec. 4.1.2, and locations of observers are shown in fig. 4.9. The periodic boundary condition deals with particles that reach the boundary of the box. A scenario does not have to include energy losses, but, consequently, it has to include at least one breaking condition to avoid infinite loops (see appendix B for technical details regarding simulations). The maximum trajectory length is a commonly employed breaking condition, and it is used in this case, with the length of 2 Gpc. It is identified to cause anisotropies in a way like it is described above, in sec. 5.2, on the location at the border of two domains, but not in the location of the void (see the upper row fig. 5.1). The amplitudes of a dipolar moment are $C_1/C_0 = 0.0060$ and $C_1/C_0 = 0.00003$ for the border and the void location, respectively. Two additional sky maps are shown in the same figure with

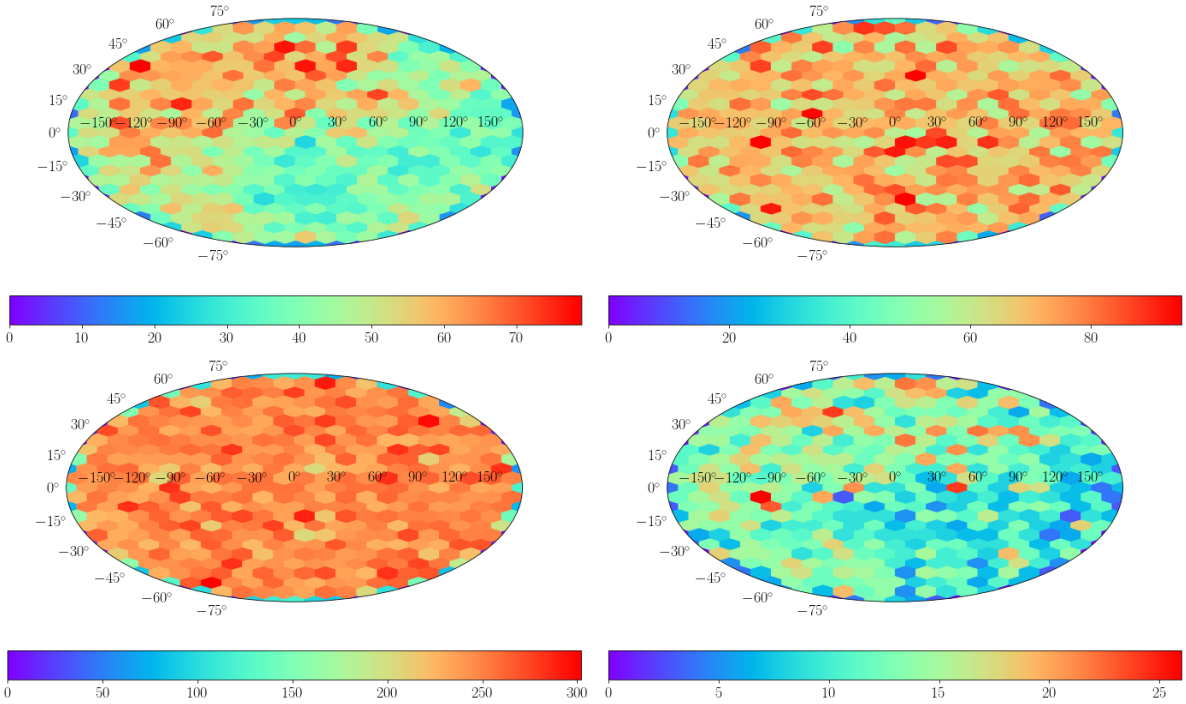

Figure 5.1: These four sky maps shows binned events that are recorded in the four scenarios described in the text. In all four scenarios particles are injected homogeneously and isotropically. The two upper panels show the location at the border between two zones (left) and the location in the void (right). The bottom sky maps are the zero magnetic field case (left) and the first upper left scenario with interactions included (right).

the zero magnetic field scenario on the bottom left panel, and with energy losses and the structured field on the bottom right panel. The associated dipolar moment amplitudes are $C_1/C_0 = 0.0065$ for energy losses included and $C_1/C_0 = 0.000008$ for the zero field case. The zero magnetic field case serves only as a sanity test in which perfect isotropy is expected from the isotropic and homogeneous distribution everywhere.

Now, the scenario at the border location without energy losses is taken and the backtracking procedure is initiated to increase the statistics of arrival directions. Anti-iron particles are propagated isotropically from the observer until the propagation length of 500 Mpc is achieved. At that point, the position of the particle is recorded. Figure 5.2 shows the result in which the dipolar vector of arbitrary length is drawn in the direction of the dipolar anisotropy calculated as $\frac{1}{N}\sum_i^N \hat{n}_i(\omega)$ where the unit vector $\hat{n}_i$ is the direction of ith event from the forward propagated simulation. The direction points to the region of the weaker magnetic field where particles propagated further and that is where the dipolar anisotropy is the forward tracking simulation also points.

The interpretation is already given above, but it is worth to repeat that, at least within the propagation simulations, a magnetic field indirectly can be responsible for the large-scale anisotropies at one should take into account in the process of designing a simulation scenario. In the real Universe, this question is probably not of interest since it is hard to argue that the distribution of cosmic rays would be homogeneous and isotropic in the first place, thus the investigated scenario is not so relevant in such a naive form. However, it can be imagined that the magnetic horizon, which is not uniform in every direction from the observer due to the influence of the large-scale structures, is a cause of the large-scale anisotropies under the assumption that the dominant part of the flux comes from sources that are located enough from the observer that the effect would be noticeable. A further investigation is required for more quantitative estimates of this effect.

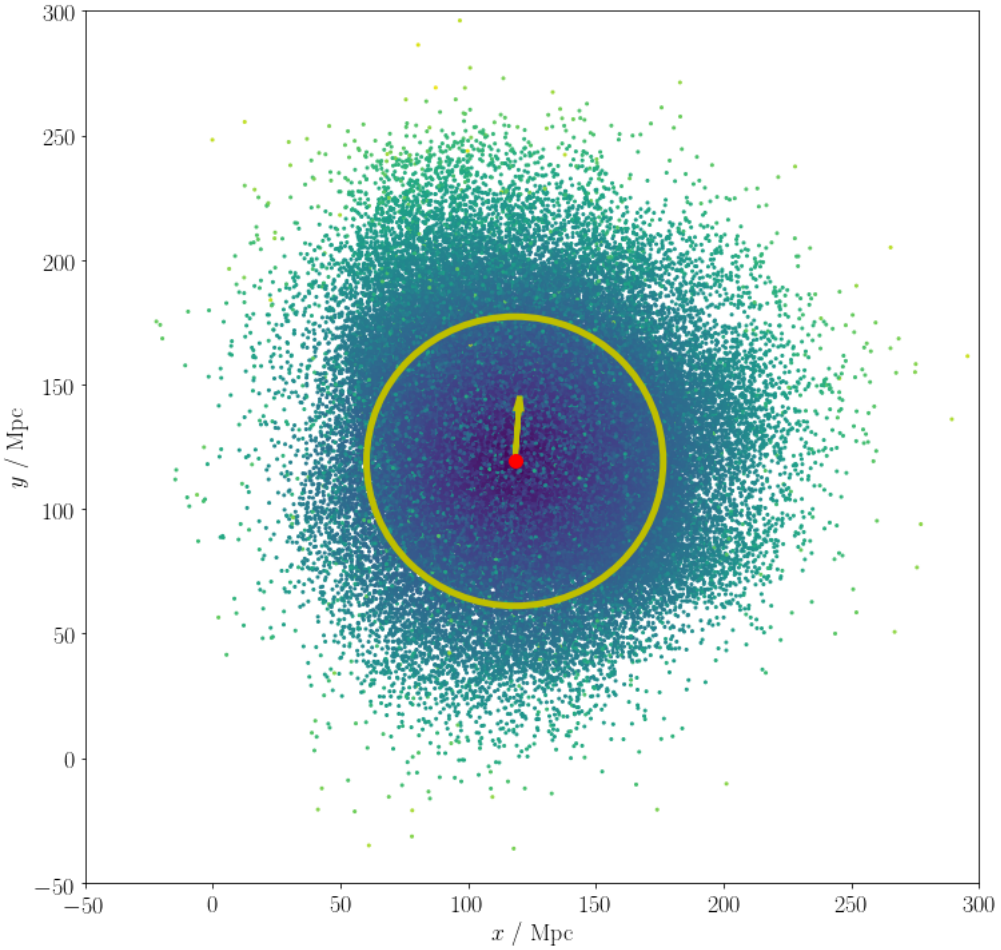

Figure 5.2: On this figure, positions of particles after propagating for 500 Mpc from the observer (the red dot) are plotted. The yellow circle represents an average distance crossed for all particles. The backtracking procedure is performed on the first scenario of the previous figure.

5.3 Summary

This section is dedicated to studying the effects of magnetic fields on anisotropies. The application of Liouville's theorem is reviewed with an emphasis on the assumptions used and on its scope of applicability. It is explained that the usual statement of homogeneous and isotropic distribution at infinity does not mean automatically isotropy in all arrival directions. The statement formally only holds per dynamical trajectory in the stationary state, i.e., requiring that every point along a dynamical trajectory should have the same intensity. Therefore, every trajectory has to be backtracked. If it is backtracked to infinity, then the direction is counted as allowed. If it is periodic,

it does not need to have the same intensity, and is named forbidden direction. It is further argued that various processes such as scatterings, energy losses, etc. are turning forbidden directions into allowed and vice versa, which isotropise everything, thus the application of the theorem holds for all trajectories, although this breaks the assumption when stating the theorem. Here, a trapping mechanism is proposed which can generate anisotropies by using the fact that some particles have longer trajectories than others, which can have an effect on their properties during propagation, such as energy losses. Again, the assumption of the theorem is broken, but formally this does not differ from the isotropisation argument. To demonstrate this, a case with a structured magnetic field is proposed that can generate a dipolar anisotropy which depends on a location of the observer in the large-scale structure.

6 | Conclusions and Outlook

Anisotropies in the arrival directions of ultra-high energy cosmic rays are the main subject of study in this thesis. Observations report no significant correlation with known objects of the celestial sphere and general isotropy on all scales. The only exception is a significant, but rather weak, dipolar anisotropy above 8 EeV, which was officially reported by the Pierre Auger Observatory last year. This dipolar anisotropy points away from the galactic centre that the sources of those cosmic rays probably are not in our galaxy. Since anisotropies can be either due to a particular source distribution, to high spread in arrival directions, or to both, the cause of this observation cannot be easily determined.

The common approach of this research field to account for this situation is through the use of complex propagation simulations, which include an enormous number of assumptions and parameters, ranging from different models of extra-galactic and galactic fields, different injection compositions, different injecting power laws, differently tuned interactions by choosing over several infrared photon field models, various assumptions regarding the source distribution, different propagation codes, etc. The result of this complexity is that many statements and indications are often contradictory, or at least they have an emphasis on different components making different interpretations. Needless to say that most of the results are difficult to reproduce.

In this work, the decision was to study perhaps less realistic cases but to gain in terms of transparency and stability of the results, which would be a basis for more complex works later. Propagation simulations are undeniably necessary tools for the job, especially frameworks such as CRPropa 3, which includes all, so to say, ‘bells

and whistles' one can ask for, but without advancements in the analytical department, unfortunately, those powerful tools can hardly be used productively.

The results of this work can be summarised as follows.

An approach using stochastic differential equations to model the propagation in a turbulent field is reviewed, and a criterion for the transition from the rectilinear motion to diffusion in this magnetic field is proposed and demonstrated using propagation simulations.

A single source model in the presence of deflections is then studied. Other sources in this model are considered to contribute only to isotropy. Besides deflections in turbulent fields, the effects of a structured magnetic field are investigated, where it is shown that structured magnetic fields tend to rise smaller scale anisotropies compared to the large-scale ones, such as a dipole. Finally, the model is confronted with the experimental data in which parameters of the model are determined. To explain the observed dipolar anisotropy and insignificant quadrupole, strong deflections are required, expressed in the form of a deflection angle along the line of sight with the source of $\left(50^{+11}_{-10}\right)^{\circ}$. Additionally, the contribution from a single source to the total flux should be $(3 \pm 1)\%$ to match the dipolar amplitude. Furthermore, if Cen A or the Virgo cluster are considered as the closest source, the constraints on a turbulent magnetic field can be given.

In the last part, the influence of magnetic fields on anisotropies is covered. The application of Liouville's theorem to cosmic ray anisotropies is reviewed and elaborated since debates still exist around it. It is identified that propagation simulations can generate anisotropies from isotropy and homogeneity only due to the presence of magnetic fields. That is explained, and a case with a structured magnetic field is demonstrated in which the dipolar anisotropy is obtained.

The further work would focus on cases which exploit the ability of new observatories to discriminate the particle composition per event basis. That would enable to constrain much better the intervening magnetic fields since the arrival directions would be correlated with rigidities, and not with energies as the case is nowadays.

A | Spherical harmonics

The analysis of anisotropies in the arrival directions of cosmic rays, which is the main topic of study in this work, heavily relies on different mathematical tools which deal with spherical geometry. The reason for this is obvious: all available experimental results, especially those regarding the ultra-high energy cosmic rays, are measured from the Earth or from the near vicinity of the Earth. Potential sources of cosmic rays, on the other hand, are assumed to be much farther away compared to distances available for the experiments. Therefore, acquired data is tied to the celestial sphere and expressed in terms of spherical geometry where the dominant role play spherical harmonics.

Spherical harmonics are obtained as a solution of Laplace's equation in spherical coordinates [192]:

$$\nabla^2 f = \frac{1}{r^2}\left[\frac{\partial}{\partial r}\left(r^2\frac{\partial f}{\partial r}\right) + \frac{1}{\sin\theta}\frac{\partial}{\partial\theta}\left(\sin\theta\frac{\partial f}{\partial\theta}\right) + \frac{1}{\sin^2\theta}\frac{\partial^2 f}{\partial\varphi^2}\right] = 0 \ . \tag{A.1}$$

They are defined as:

$$Y_\ell^m(\theta,\varphi) \equiv (-1)^m\sqrt{\frac{2\ell+1}{4\pi}\frac{(\ell-m)!}{(\ell+m)!}}\,P_\ell^m(\cos\theta)\,e^{im\varphi} \ . \tag{A.2}$$

where P_ℓ^m are associated Legendre polynomials.

Some of properties of Y_ℓ^m are:

$$Y_\ell^m(\theta,\varphi)^* = (-1)^m \sqrt{\frac{(2\ell+1)}{4\pi}\frac{(\ell-m)!}{(\ell+m)!}}\, P_\ell^m(\cos\theta)\, e^{-im\varphi} \tag{A.3}$$

$$Y_\ell^{-m}(\theta,\varphi) = (-1)^m Y_\ell^m(\theta,\varphi)^* \tag{A.4}$$

$$\int_{\theta=0}^{\pi}\int_{\varphi=0}^{2\pi} Y_\ell^m\, Y_{\ell'}^{m'*}\, \mathrm{d}\varphi \mathrm{d}\theta = \delta_{\ell\ell'}\,\delta_{mm'} \tag{A.5}$$

$$\sum_{m=-\ell}^{\ell} Y_{\ell m}^*(\theta,\varphi)\, Y_{\ell m}(\theta,\varphi) = \frac{2\ell+1}{4\pi} \tag{A.6}$$

Here expressions for the first few orthonormalised spherical harmonics (with the Condon-Shortley phase convention) are given:

$$Y_0^0(\theta,\varphi) = \frac{1}{2}\sqrt{\frac{1}{\pi}} \tag{A.7}$$

$$Y_1^{-1}(\theta,\varphi) = \frac{1}{2}\sqrt{\frac{3}{2\pi}}\,\sin\theta\, e^{-i\varphi} \tag{A.8}$$

$$Y_1^0(\theta,\varphi) = \frac{1}{2}\sqrt{\frac{3}{\pi}}\,\cos\theta \tag{A.9}$$

$$Y_1^1(\theta,\varphi) = \frac{-1}{2}\sqrt{\frac{3}{2\pi}}\,\sin\theta\, e^{i\varphi} \tag{A.10}$$

$$Y_2^{-2}(\theta,\varphi) = \frac{1}{4}\sqrt{\frac{15}{2\pi}}\,\sin^2\theta\, e^{-2i\varphi} \tag{A.11}$$

$$Y_2^{-1}(\theta,\varphi) = \frac{1}{2}\sqrt{\frac{15}{2\pi}}\,\sin\theta\,\cos\theta\, e^{-i\varphi} \tag{A.12}$$

$$Y_2^0(\theta,\varphi) = \frac{1}{4}\sqrt{\frac{5}{\pi}}\,(3\cos^2\theta - 1) \tag{A.13}$$

$$Y_2^1(\theta,\varphi) = \frac{-1}{2}\sqrt{\frac{15}{2\pi}}\,\sin\theta\,\cos\theta\, e^{i\varphi} \tag{A.14}$$

$$Y_2^2(\theta,\varphi) = 14\sqrt{\frac{15}{2\pi}}\,\sin^2\theta\, e^{2i\varphi}\ . \tag{A.15}$$

Since spherical harmonics form an orthonormal basis, an expansion of a function

$f(\theta, \varphi)$ to spherical harmonics is possible:

$$f(\theta, \varphi) = \sum_{\ell=0}^{\infty} \sum_{m=-\ell}^{\ell} a_{\ell m}\, Y_\ell^m(\theta, \varphi) \tag{A.16}$$

where the coefficients of the expansion are:

$$a_{\ell m} = \int_\Omega f(\theta, \varphi)\, Y_\ell^{m*}(\theta, \varphi)\, d\Omega = \int_0^{2\pi} d\varphi \int_0^{\pi} d\theta\, \sin\theta f(\theta, \varphi) Y_\ell^{m*}(\theta, \varphi) \tag{A.17}$$

in analogy with a Fourier series.

The angular power spectrum C_ℓ is defined through an expansion of some function f in spherical harmonics:

$$C_\ell \equiv \langle |a_{\ell m}|^2 \rangle = \frac{1}{2\ell + 1} \sum_{m=-\ell}^{\ell} |a_{\ell m}|^2 \ . \tag{A.18}$$

where

$$\langle a_{\ell m} a^*_{\ell' m'} \rangle = \int_0^{2\pi} d\varphi \int_0^{\pi} d\theta\, \sin\theta f(\theta, \varphi) f(\theta, \varphi) Y_\ell^{m*}(\theta, \varphi) Y_{\ell'}^{m'}(\theta, \varphi) \ . \tag{A.19}$$

A.1 Circular shape distribution

A circular shape can be also defined as a spherical cap and on a sphere this is described as:

$$f(\vartheta, \varphi) = \Theta(\theta - \vartheta) \tag{A.20}$$

where Θ is the Heaviside step function and the θ is the angular size of the circle. Now, C_ℓ can be calculated:

$$a_{\ell m} = \int_0^{2\pi} d\varphi \int_0^{\pi} d\vartheta\, \sin\vartheta \Theta(\theta - \vartheta) Y_\ell^{m*}(\vartheta, \varphi)$$

$$a_{\ell m} = \int_0^{2\pi} d\varphi \int_0^{\theta} d\vartheta\, \sin\vartheta Y_\ell^{m*}(\vartheta, \varphi) = 2\pi \sqrt{\frac{2\ell + 1}{4\pi}} \int_{\cos(\theta)}^{1} dx\, P_\ell^0(x)$$

$$\int_{\cos(\theta)}^{1} dx\, P_\ell^0(x) = \int_{\cos(\theta)}^{1} dx\, P_\ell(x) = 2^\ell \cdot \sum_{k=0}^{\ell} \binom{\ell}{k} \binom{\frac{\ell+k-1}{2}}{\ell} \int_{\cos(\theta)}^{1} x^k\, dx$$

$$= 2^\ell \cdot \sum_{k=0}^{\ell} \binom{\ell}{k} \binom{\frac{\ell+k-1}{2}}{\ell} \frac{1}{k+1} \left(1 - \cos(\theta)^{k+1}\right)$$

$$(...)$$

$$\Rightarrow C_\ell = 2^{2\ell}\pi \left[\sum_{k=0}^{\ell} \binom{\ell}{k} \binom{\frac{\ell+k-1}{2}}{\ell} \frac{1}{k+1} \left(1 - \cos(\theta)^{k+1}\right)\right]^2$$

A.2 Fisher distribution

The derivation and the solution for the Fisher distribution is given in sec. 4.1.

B | CRPropa

Many results in this thesis could not be possible without the support of numerical tools. CRPropa 3 is a cosmic ray propagation framework which has a central role in this context, and as such, deserves a detailed description.

CRPropa was originally started by G. Sigl and later developed into a publicly-available[1] numerical package for the propagation of ultra-high energy protons by the work of several people [193]. Adding the capability to propagate heavier nuclei led to the 2.0 version [194], and the current version 3 represents a major rewrite, which is based on a modular architecture enabling multiple new use cases [172, 195, 196]. The code is licensed under the GNU General Public License 3 which means that it can be freely re-used and modified, but the derived works, if shared with others, have to be released under a compatible license. Only the latest version will be described here[2].

B.1 Design and modules

CRPropa is designed to propagate highly relativistic cosmic rays only, and that is why it approximates the speed of cosmic rays with the speed of light and does not support lower velocities. The code design is abstractly divided between mutable data containers called `Candidate(s)`, which represent particles of different types and carry all information about the particle's physical state, and stateless modules which change properties of candidates during the simulation. That design provides an easy way to exploit the

[1] `https://crpropa.desy.de`

[2] Identified by the following Git commit hash: `f01ad2ee04a553ae051c9ae237ae50da5597e733` (27-02-2018).

thread based parallelism of modern multi-core CPU architectures, in this case, by using OpenMP, so that each particle can be distributed in a separated CPU thread and independently processed, while efficiently sharing the modules and their memory content. The advantage of sharing modules is especially noticed when storing huge amounts of data in memory, such as large magnetic field grids. Of course, the assumption here is that candidates do not mutually interact; otherwise, a parallelisation of this kind would not be possible.

An ordinary simulation in CRPropa is executed by a main loop implemented as a class `ModuleList` which sequentially iterates `Candidate(s)` through the list of modules until some breaking condition is met. Internally, the candidate iteration stops if the candidate's property `isActive` is set to false by a module. The `ModuleList` is fed with candidates by a candidate generator called `Source`. There is also an option that the user inserts candidates into the `ModuleList` individually. As CRPropa is primarily a propagation code, the most important modules are, naturally, propagation modules and so the crucial breaking criteria are triggered by reaching the total propagation length of a candidate or by reaching some spatial coordinates, for example, when a certain geometrical boundary, such as the boundary of the observer, is crossed. Possible propagation modules are `SimplePropagation`, which provides for rectilinear propagation and `PropagationCK`, which serves for three-dimensional propagation in magnetic fields. Additionally, there is a diffusional propagation module, called `DiffusionSDE`, which solves the transport equation using stochastic differential equations [197].

Energy-loss processes of cosmic rays are handled by a set of interaction modules that change the states of candidates. In the case of simulating cosmic rays, the most important modules are `ElectronPairProduction` for electron-pair production of charged nuclei when interacting with background photons, `NuclearDecay` for decaying unstable nuclei, `PhotoDisintegration` for photo-disintegration of nuclei by background photons, `PhotoPionProduction` for photo-pion interactions of nuclei with background photons, and `Redshift` for an adiabatic energy loss due to the expansion of the universe. The interaction modules can generate secondary particles which are treated as ordinary can-

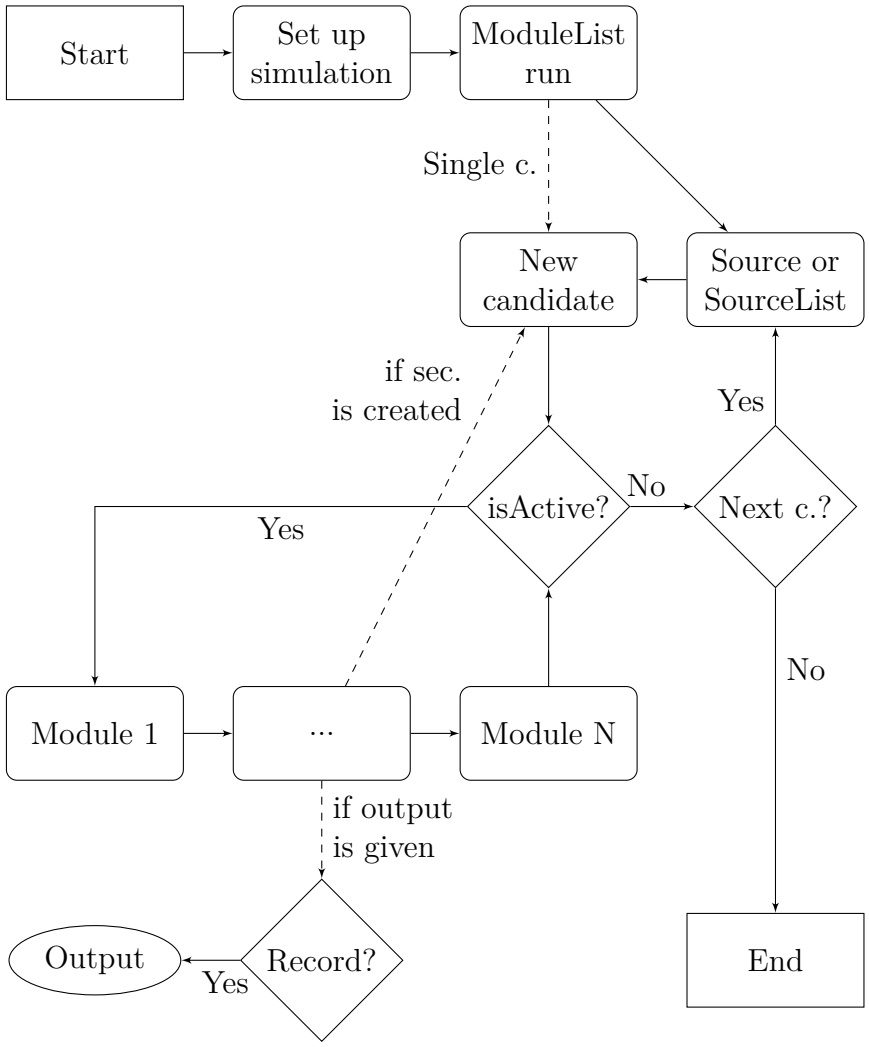

Figure B.1: The flowchart diagram of a typical CRPropa simulation. After the specification of a simulation is given, where all modules were defined and added to `ModuleList`, the main loop is started. Providing a source is optional since `ModuleList` can accept individual candidates prepared by the user. In case `Source` (or `SourceList`) is specified, which consists of `SourceFeature` such as position(s), composition, emission direction, redshift and so on, `ModuleList` gets new candidates from `Source` (or `SourceList`). Every new candidate is iterated through the list of modules until one of them deactivates it, then the next candidate is taken if there is a next candidate. The total number of candidates which will be iterated may be specified in the beginning, e.g., in the source modules. The candidate will be forwarded to output if the condition for recording it is fulfilled.

didates. The secondary particles can be iterated either immediately after their creation or after the iteration of their parent candidate is finished.

Other modules are mostly technical in nature. The `Observer` module enables the detection of candidates in a certain part of the simulation box based on their position, which can be specified as a geometric shape, e.g., sphere. The `Output` modules can be plugged in the observer module and then they are in charge of recording detected candidates in different output streams, such as text (`TextOutput`), HDF5 (`HDF5Output`), shell (`ShellOutput`) or in-memory (`ParticleCollector`). The boundaries and conditions modules can activate an action if a certain condition is fulfilled, like crossing the boundary of the simulation box or reaching an energy threshold.

Data objects form the third component of the core functionality. The data objects can be, for example, different magnetic fields, which are passed as an argument to the `PropagationCK` module, or photon fields, mass and decay tables, which serve as an input for the above-mentioned interaction modules.

CRPropa is written in the C++ programming language, where SOPHIA, an external library used by `PhotoPionProduction`, is the only exception. SOPHIA is a FORTRAN Monte Carlo code for photohadronic interactions of relativistic nucleons with an ambient photon radiation field [198]. CRPropa is meant to be used either directly through C++ or, preferably, through the interface for the Python programming language that is accomplished with SWIG. SWIG is an automatic code generator of the interface code which allows other high-level programming languages to access C/C++ functions and data types.

In the following sections, components that are predominately used in this work will be covered.

B.2 Three-dimensional propagation

The three-dimensional propagation in CRPropa works through the `PropagationCK` module which is based on solving the equations of motion of a relativistic charged

particle in a magnetic field (see chapter 3):

$$\frac{\mathrm{d}y}{\mathrm{d}t} = \frac{\mathrm{d}}{\mathrm{d}t}\begin{pmatrix}\mathbf{x}\\ \mathbf{u}\end{pmatrix} = \begin{pmatrix}\mathbf{u}\\ \frac{qc}{E}\mathbf{u}\times\mathbf{B}(\mathbf{x})\end{pmatrix}, \quad y(t_0) = y_0 = \begin{pmatrix}\mathbf{x}_0\\ \mathbf{u}_0\end{pmatrix} \tag{B.1}$$

where q, $\mathbf{u}$ and E are the particle's charge, velocity and energy, respectively, while $\mathbf{B}(\mathbf{x})$ is the magnetic field at the particle's position. Values with subscript 0 are the initial values.

Generally, the differential equation (B.1) does not have an exact solution for every initial-value problem, so in most cases it is solved numerically, and, commonly today, this is done by employing the Runge-Kutta class of methods. As always, any numerical method requires a conversion of a differential equation to a discrete analogy, i.e., to a difference equation, first presented by Leonhard Euler back in the 18th century [199]. The conversion relies on the Taylor series expansion where higher terms of the expansion are truncated. Various techniques then look how to minimise the local truncation error to make the solution of the difference equation as close as possible to the solution of the initial-value problem. For the initial value problem $y'(t) = f(t, y(t))$, $y(t_0) = y_0$, Euler's method, starting from $y(t_0)$, iteratively approximates the value of $y(t_n)$ in the nth step:

$$y_{n+1} = y_n + hf(t_n, y_n) \tag{B.2}$$

where h is the step size defined by $t_n = t_0 + nh$, and thus roughly solves $y(t)$.

In that sense, the Runge-Kutta class of methods shares the same background as the original Euler's method, which is also sometimes referred as the simplest Runge-Kutta method. For a description of the Runge-Kutta based algorithms see, for example, [200].

CRPropa also uses the Runge-Kutta method, however, with a more refined approach from the subclass of adaptive Runge-Kutta methods originally developed by Fehlberg [201]. In these methods, an adaptive step size is controlled by estimating the local truncation error. Specifically in CRPropa, the Cash-Karp method [202] is adopted,

which is defined by the following Butcher tableau:

$$
\begin{array}{c|cccccc}
0 & & & & & & \\
\frac{1}{5} & \frac{1}{5} & & & & & \\
\frac{3}{10} & \frac{3}{40} & \frac{9}{40} & & & & \\
\frac{3}{5} & \frac{3}{10} & -\frac{9}{10} & \frac{6}{5} & & & \\
1 & -\frac{11}{54} & \frac{5}{2} & -\frac{70}{27} & -\frac{35}{27} & & \\
\frac{7}{8} & \frac{1631}{55296} & \frac{175}{512} & \frac{575}{13824} & \frac{44275}{110592} & \frac{253}{4096} & \\
\hline
 & \frac{37}{378} & 0 & \frac{250}{621} & \frac{125}{594} & 0 & \frac{512}{1771} \\
 & \frac{2825}{27648} & 0 & \frac{18575}{48384} & \frac{13525}{55296} & \frac{277}{14336} & \frac{1}{4}
\end{array}
\tag{B.3}
$$

where the first column are c_j coefficients, a_{ij} are given in the triangle part and the last two rows are b_i and b_i^* coefficients for the fifth order and the fourth order accurate solution, respectively. This method is especially designed to keep the algorithm efficient in case of rapidly varying functions such as those dependent on cosmic magnetic fields.

The CRPropa implementation does not use c_j coefficients since the equation of motion does not hold an explicit time dependence, $\mathrm{d}y/\mathrm{d}t = f(y)$. Thus, the equation is calculated with:

$$
y_{n+1} = y_n + h\sum_{i=1}^{6} b_i^* k_i(y_n), \quad e_{n+1} = h\sum_{i=1}^{6}(b_i - b_i^*)k_i(y_n) \tag{B.4}
$$

where the RK coefficients are:

$$
k_1 = f(y_n), \quad k_{i=2,\ldots 6} = f\left(y_n + h\sum_{j=1}^{i-1} a_{ij}k_j\right). \tag{B.5}
$$

The calculation is iterated as long as the ratio between the direction error $e_{n+1} \to |u|$ and the tolerance is bigger than 1, or as long as the minimum step size is not reached. The tolerance is by default 10^{-4} but can also be specified by the user. One of the consequences of this numerical method is that the computation time depends on the cosmic ray deflection in the magnetic field, e.g., the stronger the field for a given particle the more computation time needed for the solution to converge. In that case, specifying

the maximum step size can help, which is the last argument that can be passed to `PropagationCK` besides the magnetic field, the tolerance, and the minimum step.

In the case of neutral particles, the method reduces to a rectilinear propagation and the maximum step size is proposed as the next step.

B.2.1 Magnetic fields

The `PropagationCK` module accepts magnetic field models that can be defined in multiple ways. The only property that they are required to provide is the `getField` method, which is a function of the three-dimensional position and which returns a field vector in that point of space. The most versatile method of providing a magnetic field model is by loading it as a three-dimensional grid lattice. If the value in-between grid points is requested, a trilinear interpolation of the eight neighboring grid points is performed.

Then loading a grid to CRPropa, the expected file format of the grid is a binary file that contains a $N_x \times N_y \times N_z$ array of float point numbers. The grid can be saved and loaded with CRPropa's `dumpGrid` and `loadGrid`, respectively. Or independently of CRPropa, to load such a grid in NumPy's ndarray, the following function is sufficient:

```
import numpy
import struct
def load_grid(filename, Nx, Ny, Nz):
    dim = 1 # 3 for vector, 1 for scalar
    fsize = struct.calcsize('f')
    grid = numpy.zeros((Nx*Ny*Nz,dim), dtype=float)
    with open(filename, 'rb') as f:
        for i in range(Nx*Ny*Nz):
            grid[i] = struct.unpack('f'*dim, f.read(dim*fsize))

    return grid.reshape((Nx, Ny, Nz, dim))
```

where `filename` is the file system path to the grid file. A saving grid function can be implemented analogously.

Some fields, like a homogeneous isotropic turbulent magnetic field, can be generated

on the fly. The isotropic turbulent magnetic field is theoretically described in sec. 3.3.1, eq. (3.30). For similar implementations see [203, 204]. Firstly, the k-space $\mathbf{B}(\mathbf{k})$ is constructed by drawing for each grid point (in total N^3) a random amplitude from following the power spectrum $\mathbf{B}^2(k) = k^\alpha$ where the default value $\alpha = -11/3$ represents a Kolmogorov spectrum[3]. The random amplitude is modulated by a random complex phase, and a random orientation with $\mathbf{k} \cdot \mathbf{B} = 0$ to satisfy $\nabla \cdot \mathbf{B} = 0$ approximately. All $\mathbf{B}(\mathbf{k})$ outside of $[k_{\min} \equiv \text{spacing}/L_{\max}, k_{\max} \equiv \text{spacing}/L_{\min}]$ are set to zero. In $k_{\min}$ and $k_{\max}$, `spacing` is the physical distance between two nearest grid points. After that, the field is transformed into real space with a Fast Fourier Transform method provided from the FFTW software package [205]. In-place complex to real Fourier transform follows to retrieve only the real components. Finally, the grid is normalised to B_{rms}. It is worth to notice that by this prescription, the resulted turbulent field has periodic boundary conditions. The prescription can be sketched also by the following formulas:

$$\begin{aligned} \mathbf{B}(\mathbf{x}) &= \text{Re}\left\{\text{FFT}\left[\hat{\mathbf{n}}|\mathbf{k}|^{\alpha/2}\left(\hat{\mathbf{e}}_1\cos(\theta) + \hat{\mathbf{e}}_2\sin(\theta)\right)\mathrm{e}^{\mathrm{i}\phi}\right]\right\} \\ \mathbf{B}(\mathbf{x})_{\text{norm}} &= \frac{B_{\text{rms}}}{\sqrt{\frac{1}{N^3}\sum^{N^3}\mathbf{B}^2(\mathbf{x})}}\mathbf{B}(\mathbf{x}) \end{aligned} \tag{B.6}$$

where $\hat{\mathbf{n}}$ is a random unit vector, $\hat{\mathbf{e}}_1$ and $\hat{\mathbf{e}}_2$ are unit vectors which with $\mathbf{k}$ form an orthogonal basis, while θ and ϕ are random angles from 0 to 2π.

The turbulent field can be modulated with a scalar grid to mimic a large scale structure distribution (LSS), e.g., filaments, voids and clusters. The advantage is that the provided scalar grid does not need to match the size of a turbulent grid, which enables a high resolution of the vector field, but at the same time covers a large portion of space with that scalar one.

It is expected that the galactic magnetic field is at least equally important as extra-galactic magnetic fields for ultra-high energy cosmic rays, thus CRPropa provides implementations of two galactic field models: Jansson & Farrar (JF12) [177] and Pshirkov et al. (PT11) [206]. Although significantly stronger compared to extra-galactic mag-

[3]Note that the difference from canonical $n = 5/3$ is due to additional k^{-2} in three dimensions (see eq. (3.43)) which gives $\alpha = -n - 2$.

netic fields, galactic fields extend only to a small portion of space of order $\sim 10\,\mathrm{kpc}$. On such propagation lengths energy-loss processes are mostly negligible. Therefore, only deflections should be considered and that is the basis for the notion of "lensing". The "lensing" technique maps the arrival directions on the Earth with directions where cosmic rays enter the galaxy. After the mapping is generated by backtracking simulations, it is much faster to apply lensing to retrieve the deflections caused by the galactic magnetic field than to simulate the propagation through it. The "lensing" in CRPropa is initially based on the PARSEC implementation [207].

B.2.2 Performance of `PropagationCK`

Statistical uncertainties in every Monte Carlo analysis depend on the number of simulated experiments, thus, "the more the better" is the main idea behind this approach. Unfortunately, this is limited by the capabilities of computers, both in terms of software and hardware. Simulating the propagation of cosmic rays in CRPropa is generally a CPU intensive task and it is worth to estimate the time required for a simulation with N simulated particles to finish. The simulation time is affected by all modules, some of them having a considerable impact while others execute in no time. One can use `PerformanceModule` instead of `ModuleList` to monitor the simulation performance of every employed module. CRPropa can simulate numerous different scenarios and can be used on various hardware which can lead to completely different run times for each case. Nevertheless, certain "invariant" estimates can be inferred. First of all, in theory, the simulation performance scales linearly with the number of CPU threads. Hence, the total performance estimation can be calculated from the performance per thread. In practice, the scaling saturates around 8 threads [172] due to PhotoPionProduction, which rely on external libraries not optimised for parallel computing (SOPHIA [198]).

Since this work revolves around the propagation of cosmic rays in magnetic fields, the knowledge of the `PropagationCK` performance is relevant. As already noted above, the larger the deflections of cosmic rays in a magnetic field, the more time needed for the calculation of the next propagation step to converge resulting with a smaller step

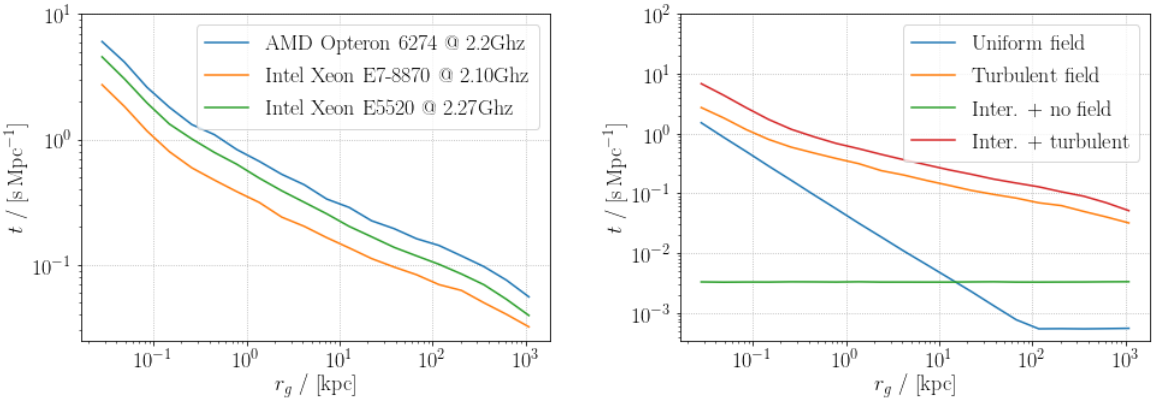

Figure B.2: These two plots show the performance of the `PropagationCK` module: the propagation time of 1000 particles per Mpc versus the Larmor radius r_g as a measure of the average deflection of cosmic rays. The left panel compares different CPUs in the case of a turbulent field. On the right panel the comparison between the performance of various scenarios in the same measure quantity (propagation time) on the same computer (Intel® Xeon® E7-8870). The various scenarios of propagation are: the turbulent field with and without interactions included, the uniform field of the same magnitude as the turbulent one, and 1D propagation with interactions included.

size. The small step size means more iterations of all modules per physical length which consequently requires more total CPU time per cosmic ray trajectory. In this case, to some extent, an invariant unit of performance can be chosen as the time needed to propagate 1000 particles per thread per mega-parsec based on their Larmor radius $r_g = \frac{E}{c|q|B}$ (see sec. 3.2). Figure B.2 shows test results for three different CPUs when particles are propagated in a turbulent or uniform magnetic field. The test consists of injecting 1000 protons with energy 1 EeV isotropically for 20 different magnetic field strengths ranging from 1 nG to 30 μG. The used turbulent field is defined with the following parameters: $L_{\text{min}} = 1.5\,\text{kpc}$ and $L_{\text{max}} = 90\,\text{kpc}$ which, by 3.50, gives $L_c = 19.2\,\text{kpc}$.

B.3 The finite-size observer problem

The total number of particles that can be propagated are limited by the processing power of computers. Thus, in the forward tracking propagation mode, a problem of collecting a sufficient number of events detected by the small-size observer, occurs. If the observer would be of the size of the Earth as in the real Universe, an injection of $N_{\text{inject}} = N_{\text{Earth}}(d_{\text{src}}/r_{\text{Earth}})^2 \sim (\text{Mpc}/10^6\text{m})^2 = 10^{33}$ particles would be necessary to

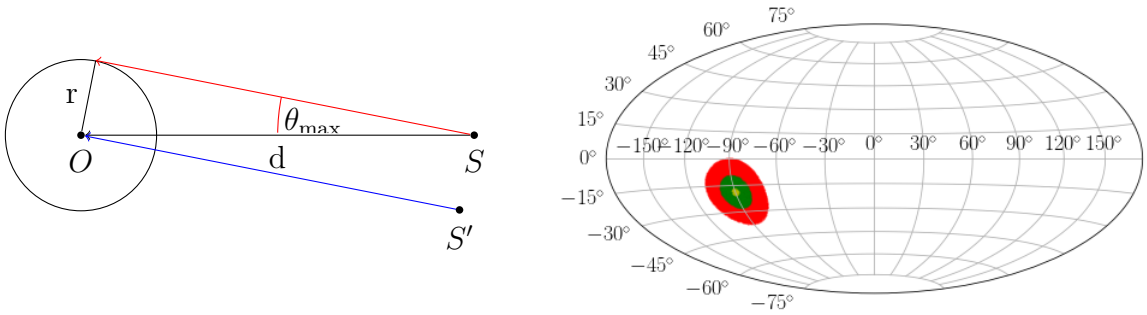

Figure B.3: On the left panel: the particle that arrived from S and hit the edge of the observer O (the red vector) is seen as a particle that came from the source S' from the perspective of a point-like observer (the blue vector). Due to its finite-size, the observer O creates a virtual source S', which is displaced at most by the radius r of observer's sphere. Hence, the finite-size observer transforms a point-like source S into a circular area around S. On the right panel: the sky plot of the described scenario where the yellow, green and red circle correspond to the arrival directions area of cosmic rays coming from a 3 Mpc distant source for a 0.1 Mpc, 0.5 Mpc and 1 Mpc observer size, respectively.

have just a few events from a nearby source that is within a megaparsec. Simulating these scales of interest is practically impossible since CRPropa3 optimally, without any interactions, can process $\sim 10^5$ particles/s/thread on modern hardware. That is the reason why the observer size is typically much larger than the size of the Earth.

However, by over-sizing the observer unwanted artifacts appears, especially in studies of anisotropies. From geometrical considerations alone, without deflections, it can be seen (fig. B.3) that a point-like source becomes a disk shape on the sky plot of the arrival directions, which artificially changes anisotropy. The maximum angle of the artificial deflection is given by $\theta_{\max} = \arcsin\left(\frac{r}{d}\right)$, where r is the observer radius and d is the distance from the source.

To compute the angular power spectrum of a point source seen by a spherical observer, we approximate the source image as a homogeneous circle, although it is not perfectly homogenous but has a radial distribution. A spherical cap is then a suitable model for the case: $f(\vartheta, \varphi) = \Theta(\theta - \vartheta)$ where Θ is the Heaviside step function and θ is the angular size of the circle. The calculation of C_ℓ for the circular shape is given in the previous appendix, subsection A.1. By inserting $\theta_{\max} = \arcsin\left(\frac{r}{d}\right)$ and $\cos(\arccos(x)) = \sqrt{1 - x^2}$ into the calculated C_ℓ, the angular power spectrum becomes:

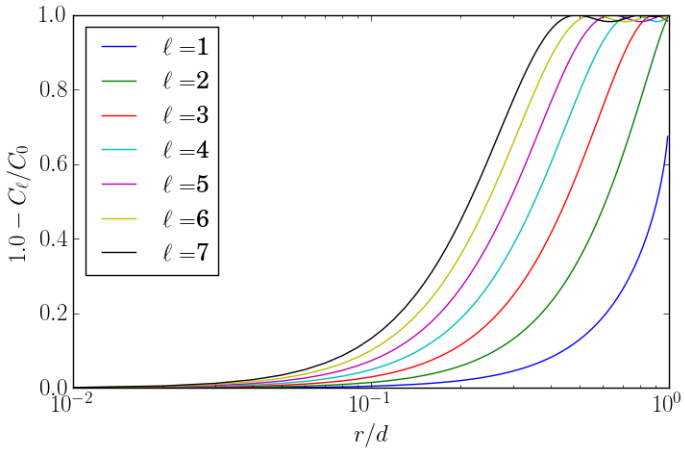

Figure B.4: The plot shows how the finite size observer or radius r affects the angular power spectrum of a nearby source at a distance d. The spectrum without deflections, i.e., when arrival directions have a $\delta-$distribution, should be $C_\ell/C_0 = 1$ without deflections (where C_0 is the monopole component), but as the ratio r/d grows to unity multiple moments, starting from higher ones, reduce their values in the angular power spectrum. For example, the ratio $r/d \sim 0.1$ will not influence the dipole significantly, but will deform $\ell = 7$ by more than 10%.

$$C_\ell = 2^{2\ell}\pi \left[\sum_{k=0}^{\ell} \binom{\ell}{k} \binom{\frac{\ell+k-1}{2}}{\ell} \frac{1}{k+1} \left(1 - \left(1 - \frac{r^2}{d^2}\right)^{(k+1)/2}\right)\right]^2 . \tag{B.7}$$

which is plotted in fig. B.4 for the first lowest multipole moments. Every moment is expressed relative to the monopole $C_0 = \pi\left(1 - \sqrt{1 - \frac{r^2}{d^2}}\right)^2$. From the result one can estimate that for a study of multipoles below $\ell = 5$, while keeping the artificial angular spread below 10%, the observer size should always be below 10% of the total distance from the nearest source.

Bibliography

[1] A. Dundović and G. Sigl, "Anisotropies of Ultra-high Energy Cosmic Rays Dominated by a Single Source in the Presence of Deflections," *Submitted to JCAP*, 2017. vii, 51

[2] Euclid, *Euclid's Elements*. Green Lion Press, 2002. 5

[3] I. Newton, *The Principia: The Authoritative Translation and Guide*. University of California Press, 2016. 5

[4] J. C. Maxwell, *A Treatise on Electricity and Magnetism*. Dover Publications, 1954. 5, 7, 26

[5] A. Galindo and P. Pascual, *Quantum Mechanics I*. Springer, 1st ed., Jan. 1990. 5

[6] G. Auletta *et al.*, *Quantum Mechanics*. Cambridge University Press, 1 ed., Apr. 2009. 5

[7] J. Butterfield and J. Earman, eds., *Philosophy of Physics (Handbook of the Philosophy of Science) 2 volume set*. North Holland, 1 ed., Dec. 2006. 5

[8] T. Stanev, *High Energy Cosmic Rays*. Springer Science & Business Media, 2010. 5, 52

[9] V. L. G. Veniamin Sergeevich Berezinskiĭ, *Astrophysics of cosmic rays*. North-Holland, 1990. 6

[10] R. E. Thomas K. Gaisser and E. Resconi, *Cosmic Rays and Particles Physics (2nd ed.)*. Cambridge University Press, 2016. 6, 30, 52, 82

[11] P. Biermann and G. Sigl, "Introduction to cosmic rays," *Lect. Notes Phys.*, vol. 576, p. 1–26, 2001. [,1(2002)]. 6

[12] A. R. Choudhuri, *Astrophysics for Physicists*. Cambridge University Press, 2010. 6

[13] A. Aab *et al.*, "Searches for anisotropies in the arrival directions of the highest energy cosmic rays detected by the Pierre Auger Observatory," *The Astrophysical Journal*, vol. 804, no. 1, p. 15, 2015. 6, 24

[14] A. Aab *et al.*, "Search for photons with energies above 10^{18} eV using the hybrid detector of the Pierre Auger Observatory," *JCAP*, vol. 1704, no. 04, p. 009, 2017. 6

[15] P. Abreu *et al.*, "A Search for Ultra-High Energy Neutrinos in Highly Inclined Events at the Pierre Auger Observatory," *Phys. Rev.*, vol. D84, p. 122005, 2011. [Erratum: Phys. Rev.D84,029902(2011)]. 6

[16] I. Lakatos, *Proofs and Refutations*. Cambridge University Press, 2015. 6

[17] C. A. Coulomb, *Mémoires sur l'électricité et la magnétisme*. 1789. 7, 8

[18] L. Jánossy, *Cosmic Rays and Nuclear Physics*. The Pilot Press Ltd., 1948. 8

[19] B. Newhall, *The history of photography*. Museum of Modern Art, 1982. 8

[20] M. S. Longair, *The Cosmic Century*. Cambridge University Press, 2006. 8

[21] O. Glasser, *Wilhelm Conrad Röntgen and the Early History of the Roentgen Rays*. Norman Publishing, 1993. 8

[22] *Nobel Lectures In Physics, Vol 1 (1901-1921)*. World Scientific, 1998. 8

[23] A. De Angelis, "Spontaneous ionization to subatomic physics: Victor Hess to Peter Higgs," *Nuclear Physics B-Proceedings Supplements*, vol. 243, p. 3–11, 2013. 9, 10

[24] N. Tesla, *Lectures and Patents*. Discovery Publisher, 2015. 9

[25] J. Elster and H. Geitel, "Ueber Elektricitätszerstreuung in der Luft," *Annalen der Physik*, vol. 307, no. 7, p. 425–446, 1900. 9

[26] C. T. R. Wilson, "On the Ionisation of Atmospheric Air," *Proceedings of the Royal Society of London*, vol. 68, p. 151–161, 1901. 9

[27] D. A. S. A. M. Hillas, Robert Robinson and D. H. ter (Auth.), *Cosmic Rays.* , Pergamon Press, 1st ed., 1972. 9, 10, 11

[28] T. Wulf, "On the radiation of high penetrating power that exists in the atmosphere," *Phys. Zeit*, vol. 1, no. 152-157, p. 124, 1909. 9

[29] T. Wulf, "Beobachtungen über Strahlung hoher Durchdringungsfähigkeit auf dem Eiffelturm," *Physikalische Zeitschrift*, vol. 11, p. 811–813, 1910. 9

[30] D. Pacini, "La radiazione penetrante alla superficie ed in seno alle acque," *Il Nuovo Cimento (1911-1923)*, vol. 3, no. 1, p. 93–100, 1912. 9

[31] A. Gockel and T. Wulf, "Beobachtungen über die Radioaktivität der Atmosphäre im Hochgebirge," *Phys. Z*, vol. 9, p. 907–911, 1908. 10

[32] V. Hess, "Penetrating radiation in seven free ballon flights," *Physics Zeits*, vol. 13, no. 1084, p. 1–4, 1912. 10

[33] V. F. Hess, "The origins of penetrating radiation," *Phys. Zeit*, vol. 14, p. 612–617, 1913. 10

[34] W. Kolhörster, "Measurements of the penetrating radiation in the free balloon at high altitudes (Aero-physical developments Halle, Essay 6)," *Phys. Zeit*, vol. 14, p. 1153–1156, 1913. 10

[35] R. A. Millikan and G. H. Cameron, "High frequency rays of cosmic origin III. Measurements in snow-fed lakes at high altitudes," *Physical review*, vol. 28, no. 5, p. 851, 1926. 11

[36] W. Bothe and W. Kolhörster, "Das wesen der höhenstrahlung," *Zeitschrift für Physik*, vol. 56, no. 11-12, p. 751–777, 1929. 11

[37] J. Clay, "Results of the dutch cosmic ray expedition 1933 VI. The variation of the penetrative power of the radiation with magnetic latitude. The energy distribution of the particles," *Physica*, vol. 2, no. 1-12, p. 299–308, 1935. 11, 85

[38] A. H. Compton, "A geographic study of cosmic rays," *Physical Review*, vol. 43, no. 6, p. 387, 1933. 11, 85

[39] A. H. Compton, "Recent developments in cosmic rays," *Review of Scientific Instruments*, vol. 7, no. 2, p. 71–81, 1936. 11

[40] L. Alvarez and A. H. Compton, "A positively charged component of cosmic rays," *Physical Review*, vol. 43, no. 10, p. 835, 1933. 11

[41] B. Rossi, "Directional measurements on the cosmic rays near the geomagnetic equator," *Physical Review*, vol. 45, no. 3, p. 212, 1934. 11

[42] K.-H. Kampert and A. A. Watson, "Extensive air showers and ultra high-energy cosmic rays: a historical review," *The European Physical Journal H*, vol. 37, no. 3, p. 359–412, 2012. 11, 13

[43] P. Auger, P. Ehrenfest, R. Maze, J. Daudin, and R. A. Fréon, "Extensive cosmic-ray showers," *Reviews of modern physics*, vol. 11, no. 3-4, p. 288, 1939. 12

[44] M. Schein, W. P. Jesse, and E. O. Wollan, "The nature of the primary cosmic radiation and the origin of the mesotron," *Physical Review*, vol. 59, no. 7, p. 615, 1941. 12

[45] C. D. Anderson, "The positive electron," *Physical Review*, vol. 43, no. 6, p. 491, 1933. 12

[46] S. H. Neddermeyer and C. D. Anderson, "Note on the nature of cosmic-ray particles," *Physical Review*, vol. 51, no. 10, p. 884, 1937. 12

[47] H. Bethe and W. Heitler, "On the stopping of fast particles and on the creation of positive electrons," in *Proc. R. Soc. Lond. A*, vol. 146, p. 83–112, The Royal Society, 1934. 12

[48] H. J. Bhabha and W. Heitler, "The passage of fast electrons and the theory of cosmic showers," in *Proc. R. Soc. Lond. A*, vol. 159, p. 432–458, The Royal Society, 1937. 12

[49] J. Carlson and J. Oppenheimer, "On multiplicative showers," *Physical Review*, vol. 51, no. 4, p. 220, 1937. 12

[50] E. Fermi, "On the origin of the cosmic radiation," *Physical Review*, vol. 75, no. 8, p. 1169, 1949. 13, 30

[51] G. Kulikov and G. Khristiansen, "On the size spectrum of extensive air showers," *SOVIET PHYSICS JETP-USSR*, vol. 8, no. 3, p. 441–444, 1959. 13

[52] J. Linsley, "Evidence for a primary cosmic-ray particle with energy 10 20 eV," *Physical Review Letters*, vol. 10, no. 4, p. 146, 1963. 13

[53] J. Linsley, "Primary cosmic rays of energy 10**17 to 10**20-eV: The energy spectrum and arrival directions," in *8th International Cosmic Ray Conference (ICRC 1963) Jaipur, India, 1963*, vol. 4, p. 77, 1963. 13

[54] A. A. Penzias and R. W. Wilson, "A measurement of excess antenna temperature at 4080 Mc/s.," *The Astrophysical Journal*, vol. 142, p. 419–421, 1965. 13

[55] K. Greisen, "End to the cosmic-ray spectrum?," *Physical Review Letters*, vol. 16, no. 17, p. 748, 1966. 13

[56] G. T. Zatsepin and V. A. Kuz'min, "Upper limit of the spectrum of cosmic rays," *JETP Lett.(USSR)(Engl. Transl.)*, vol. 4, 1966. 13

[57] B. Peters, "Primary cosmic radiation and extensive air showers," *Il Nuovo Cimento (1955-1965)*, vol. 22, no. 4, p. 800–819, 1961. 14

[58] T. Antoni, W. Apel, A. Badea, K. Bekk, A. Bercuci, J. Blümer, H. Bozdog, I. Brancus, A. Chilingarian, K. Daumiller, *et al.*, "KASCADE measurements of energy spectra for elemental groups of cosmic rays: Results and open problems," *Astroparticle physics*, vol. 24, no. 1-2, p. 1–25, 2005. 14, 21

[59] W. Apel, J. Arteaga-Velázquez, K. Bekk, M. Bertaina, J. Blümer, H. Bozdog, I. Brancus, E. Cantoni, A. Chiavassa, F. Cossavella, *et al.*, "KASCADE-Grande measurements of energy spectra for elemental groups of cosmic rays," *Astroparticle Physics*, vol. 47, p. 54–66, 2013. 14, 21

[60] J. Abraham *et al.*, "Properties and performance of the prototype instrument for the Pierre Auger Observatory," *Nuclear Instruments and Methods in Physics Research Section A: Accelerators, Spectrometers, Detectors and Associated Equipment*, vol. 523, no. 1-2, p. 50–95, 2004. 14, 15

[61] A. Aab *et al.*, "The Pierre Auger cosmic ray observatory," *Nuclear Instruments and Methods in Physics Research Section A: Accelerators, Spectrometers, Detectors and Associated Equipment*, vol. 798, p. 172–213, 2015. 14, 15

[62] H. Kawai, S. Yoshida, H. Yoshii, K. Tanaka, F. Cohen, M. Fukushima, N. Hayashida, K. Hiyama, D. Ikeda, E. Kido, *et al.*, "Telescope array experiment," *Nuclear Physics B Proceedings Supplements*, vol. 175, p. 221–226, 2008. 14

[63] I. Allekotte *et al.*, "The surface detector system of the Pierre Auger Observatory," *Nuclear Instruments and Methods in Physics Research Section A: Accelerators, Spectrometers, Detectors and Associated Equipment*, vol. 586, no. 3, p. 409–420, 2008. 15

[64] J. Abraham *et al.*, "The Fluorescence Detector of the Pierre Auger Observatory," *Nucl. Instrum. Meth.*, vol. A620, p. 227–251, 2010. 15, 16

[65] M. J. Tueros, "Estimate of the non-calorimetric energy of showers observed with the fluorescence and surface detectors of the Pierre Auger Observatory," 2013. 15

[66] B. R. Dawson *et al.*, "Hybrid Performance of the Pierre Auger Observatory," *arXiv preprint arXiv:0706.1105*, 2007. 15

[67] "Instituto Nacional de Estadística y Censos de la Republica Argentina," 2010. 15

[68] "Statistisches Bundesamt Deutschland," 2017. 15

[69] T. K. Gaisser and A. M. Hillas, "Reliability of the method of constant intensity cuts for reconstructing the average development of vertical showers," in *International Cosmic Ray Conference*, vol. 8, p. 353–357, 1977. 17

[70] F. Suarez, "The AMIGA muon detectors of the Pierre Auger Observatory: overview and status," 2013. 18

[71] P. Abreu *et al.*, "Results of a self-triggered prototype system for radio-detection of extensive air showers at the Pierre Auger Observatory," *Journal of Instrumentation*, vol. 7, no. 11, p. P11023, 2012. 18

[72] A. Aab *et al.*, "The Pierre Auger Observatory Upgrade - Preliminary Design Report," 2016. 18

[73] E.-S. Seo, "Measurement of Galactic Cosmic Ray Proton and Helium Spectra During the 1987 Solar Minimum.," 1991. 20

[74] I. Ivanenko, V. Y. Shestoperov, L. Chikova, I. Fateeva, L. Khein, D. Podoroznyi, I. Rapoport, G. Samsonov, V. Sobinyakov, A. Turundaevskyi, *et al.*, "Energy spectra of cosmic rays above 2 TeV as measured by the'SOKOL'apparatus," in *International Cosmic Ray Conference*, vol. 2, p. 17, 1993. 20

[75] M. Amenomori, Z. Cao, B. Dai, L. Ding, Y. Feng, Z. Feng, K. Hibino, N. Hotta, Q. Huang, A. Huo, *et al.*, "Primary Cosmic Rays at The" Knee" Energy Region Observed with the Tibet Air Shower Array," in *International Cosmic Ray Conference*, vol. 2, p. 736, 1995. 20

[76] W. Apel, J. Arteaga-Velázquez, K. Bekk, M. Bertaina, J. Blümer, H. Bozdog, I. Brancus, P. Buchholz, E. Cantoni, A. Chiavassa, *et al.*, "The spectrum of high-energy cosmic rays measured with KASCADE-Grande," *Astroparticle Physics*, vol. 36, no. 1, p. 183–194, 2012. 20, 21

[77] T. K. Gaisser, I. Collaboration, *et al.*, "Primary spectrum and composition with IceCube/IceTop," *Nuclear and Particle Physics Proceedings*, vol. 279, p. 47–55, 2016. 20

[78] A. Aab *et al.*, "The Pierre Auger Observatory: Contributions to the 35th International Cosmic Ray Conference (ICRC 2017)," in *Proceedings, 35th International Cosmic Ray Conference (ICRC 2017): Bexco, Busan, Korea, July 12-20, 2017*, 2017. 20, 24

[79] M. S. Longair, *High energy astrophysics*. cambridge university Press, 2011. 19, 28

[80] J. Abraham *et al.*, "Observation of the suppression of the flux of cosmic rays above 4×10^{19}eV," *Phys. Rev. Lett.*, vol. 101, p. 061101, 2008. 19

[81] T. Abu-Zayyad, R. Aida, M. Allen, R. Anderson, R. Azuma, E. Barcikowski, J. Belz, D. Bergman, S. Blake, R. Cady, *et al.*, "The cosmic-ray energy spectrum observed with the surface detector of the telescope array experiment," *The Astrophysical Journal Letters*, vol. 768, no. 1, p. L1, 2013. 19

[82] R. U. Abbasi, T. Abu-Zayyad, M. Allen, J. F. Amman, G. Archbold, K. Belov, J. W. Belz, S. Y. Ben Zvi, D. R. Bergman, S. A. Blake, O. A. Brusova, G. W. Burt, C. Cannon, Z. Cao, B. C. Connolly, W. Deng, Y. Fedorova, C. B. Finley, R. C. Gray, W. F. Hanlon, C. M. Hoffman, M. H. Holzscheiter, G. Hughes, P. Hüntemeyer, B. F. Jones, C. C. H. Jui, K. Kim, M. A. Kirn, E. C. Loh, M. M. Maestas, N. Manago, L. J. Marek, K. Martens, J. A. J. Matthews, J. N. Matthews, S. A. Moore, A. O'Neill, C. A. Painter, L. Perera, K. Reil, R. Riehle, M. Roberts, D. Rodriguez, N. Sasaki, S. R. Schnetzer, L. M. Scott, G. Sinnis, J. D. Smith, P. Sokolsky, C. Song, R. W. Springer, B. T. Stokes, S. B. Thomas,

J. R. Thomas, G. B. Thomson, D. Tupa, S. Westerhoff, L. R. Wiencke, X. Zhang, and A. Zech, "First Observation of the Greisen-Zatsepin-Kuzmin Suppression," *Phys. Rev. Lett.*, vol. 100, p. 101101, Mar 2008. 19

[83] J. Abraham *et al.*, "Measurement of the energy spectrum of cosmic rays above 10^{18} eV using the Pierre Auger Observatory," *Phys. Lett.*, vol. B685, p. 239–246, 2010. 19

[84] A. Aab *et al.*, "Measurement of the cosmic ray spectrum above 4×10^{18} eV using inclined events detected with the Pierre Auger Observatory," *JCAP*, vol. 1508, p. 049, 2015. 19

[85] B. Ruzybayev, "Measuring the cosmic ray energy spectrum and composition with IceCube," *Physics Procedia*, vol. 61, p. 443–449, 2015. 21

[86] V. Prosin, S. Berezhnev, N. Budnev, A. Chiavassa, O. Chvalaev, A. Dyachok, S. Epimakhov, O. Gress, T. Gress, N. Kalmykov, *et al.*, "Primary CR energy spectrum and mass composition by the data of Tunka-133 array," in *EPJ Web of Conferences*, vol. 99, p. 04002, EDP Sciences, 2015. 21

[87] J. George, K. Lave, M. Wiedenbeck, W. Binns, A. Cummings, A. Davis, G. De Nolfo, P. Hink, M. Israel, R. Leske, *et al.*, "Elemental composition and energy spectra of galactic cosmic rays during solar cycle 23," *The Astrophysical Journal*, vol. 698, no. 2, p. 1666, 2009. 21

[88] G. Sigl, *Astroparticle Physics: Theory and Phenomenology.* Springer, 2016. 21, 30, 52

[89] D. Heck, G. Schatz, T. Thouw, J. Knapp, and J. N. Capdevielle, "CORSIKA: A Monte Carlo code to simulate extensive air showers," 1998. 21

[90] R. Abbasi, T. Abu-Zayyad, M. Al-Seady, M. Allen, J. Amman, R. Anderson, G. Archbold, K. Belov, J. Belz, D. Bergman, *et al.*, "Indications of proton-

dominated cosmic-ray composition above 1.6 EeV," *Physical Review Letters*, vol. 104, no. 16, p. 161101, 2010. 21

[91] C. C. Jui, T. A. Collaboration, *et al.*, "Results from the Telescope Array Experiment," *Nuclear and Particle Physics Proceedings*, vol. 273, p. 440–445, 2016. 21

[92] J. Abraham, P. Abreu, M. Aglietta, E. Ahn, D. Allard, I. Allekotte, J. Allen, J. Alvarez-Muniz, M. Ambrosio, L. Anchordoqui, *et al.*, "Measurement of the depth of maximum of extensive air showers above 10 18 eV," *Physical review letters*, vol. 104, no. 9, p. 091101, 2010. 21

[93] A. e. a. Aab *et al.*, "Depth of maximum of air-shower profiles at the Pierre Auger Observatory. II. Composition implications," *Phys. Rev.*, vol. D90, no. 12, p. 122006, 2014. 21, 74, 75

[94] R. Abbasi *et al.*, "Report of the Working Group on the Composition of Ultra High Energy Cosmic Rays," *JPS Conf. Proc.*, vol. 9, p. 010016, 2016. 21

[95] C. Bonifazi *et al.*, "The angular resolution of the Pierre Auger Observatory," *Nuclear Physics B-Proceedings Supplements*, vol. 190, p. 20–25, 2009. 22

[96] P. Sommers, "Cosmic ray anisotropy analysis with a full-sky observatory," *Astroparticle Physics*, vol. 14, no. 4, p. 271–286, 2001. 23, 72, 75

[97] A. Aab *et al.*, "Searches for Large-Scale Anisotropy in the Arrival Directions of Cosmic Rays Detected above Energy of 10^{19} eV at the Pierre Auger Observatory and the Telescope Array," *Astrophys. J.*, vol. 794, no. 2, p. 172, 2014. 23, 72

[98] M. G. Aartsen *et al.*, "Observation of Cosmic Ray Anisotropy with the IceTop Air Shower Array," *Astrophys. J.*, vol. 765, p. 55, 2013. 23

[99] M. Aglietta, V. Alekseenko, B. Alessandro, P. Antonioli, F. Arneodo, L. Bergamasco, M. Bertaina, R. Bonino, A. Castellina, A. Chiavassa, *et al.*, "Evolution

of the cosmic-ray anisotropy above 1014 eV," *The Astrophysical Journal Letters*, vol. 692, no. 2, p. L130, 2009. 23

[100] A. Abdo, B. Allen, T. Aune, D. Berley, S. Casanova, C. Chen, B. Dingus, R. Ellsworth, L. Fleysher, R. Fleysher, *et al.*, "The large-scale cosmic-ray anisotropy as observed with Milagro," *The Astrophysical Journal*, vol. 698, no. 2, p. 2121, 2009. 23

[101] M. Amenomori, "Anisotropy and Corotation of Galactic Cosmic Rays," *Science*, vol. 314, p. 439–443, 2006. 23

[102] T. Antoni *et al.*, "Large scale cosmic - ray anisotropy with KASCADE," *Astrophys. J.*, vol. 604, p. 687–692, 2004. 23

[103] M. Ahlers and P. Mertsch, "Origin of Small-Scale Anisotropies in Galactic Cosmic Rays," *Prog. Part. Nucl. Phys.*, vol. 94, p. 184–216, 2017. 23, 82

[104] S. Mollerach and E. Roulet, "Progress in high-energy cosmic ray physics," *Progress in Particle and Nuclear Physics*, 2017. 23

[105] A. Aab *et al.*, "Observation of a large-scale anisotropy in the arrival directions of cosmic rays above 8 x 1018 eV," *Science*, no. 6357, p. 1266–1270, 2017. 23, 72, 75, 77

[106] M. J. Reid and A. Brunthaler, "The Proper motion of Sgr A*. 2. The Mass of Sgr A*," *Astrophys. J.*, vol. 616, p. 872–884, 2004. 23

[107] NASA/IPAC Extragalactic Database. Accessed Dec. 10, 2012. 24

[108] P. Tinyakov *et al.*, "TA Anisotropy Summary," *PoS*, vol. ICRC2015, p. 326, 2016. 24

[109] J. P. Huchra, L. M. Macri, K. L. Masters, T. H. Jarrett, P. Berlind, M. Calkins, A. C. Crook, R. Cutri, P. Erdoğdu, E. Falco, *et al.*, "The 2MASS Redshift Survey—description and data release," *The Astrophysical Journal Supplement Series*, vol. 199, no. 2, p. 26, 2012. 24, 77

[110] W. Baumgartner, J. Tueller, C. Markwardt, G. Skinner, S. Barthelmy, R. Mushotzky, P. Evans, and N. Gehrels, "The 70 month swift-BAT all-sky hard X-ray survey," *The Astrophysical Journal Supplement Series*, vol. 207, no. 2, p. 19, 2013. 24

[111] S. van Velzen, H. Falcke, P. Schellart, N. Nierstenhöfer, and K.-H. Kampert, "Radio galaxies of the local universe-All-sky catalog, luminosity functions, and clustering," *Astronomy & Astrophysics*, vol. 544, p. A18, 2012. 24

[112] K. Kawata *et al.*, "Ultra-High-Energy Cosmic-Ray Hotspot Observed with the Telescope Array Surface Detectors," *PoS*, vol. ICRC2015, p. 276, 2016. 24

[113] H. Alfven, *Cosmical Electrodynamics*. Oxford, 1950. 25, 36, 86

[114] P. P. Kronberg, "Extragalactic magnetic fields," *Reports on Progress in Physics*, vol. 57, no. 4, p. 325, 1994. 26, 30

[115] R. Beck, "Galactic and extragalactic magnetic fields," *Space Science Reviews*, vol. 99, no. 1-4, p. 243–260, 2001. 26, 30

[116] L. M. Widrow, "Origin of galactic and extragalactic magnetic fields," *Reviews of Modern Physics*, vol. 74, no. 3, p. 775, 2002. 26

[117] J. D. Jackson, *Classical Electrodynamics, 3rd edition*. Wiley, 1999. 26, 27, 28

[118] A. Dolginov, Y. N. Gnedin, and N. Silant'ev, "Propagation and polarisation of radiation in cosmic media," *Propagation and polarisation of radiation in cosmic media, by Dolginov, AZ; Gnedin, YN; Silant'ev, NA, ISBN 2 88124 987 6. 382 pp., 1995*, 1995. 27

[119] K. M. Ferriere, "The interstellar environment of our galaxy," *Reviews of Modern Physics*, vol. 73, no. 4, p. 1031, 2001. 27

[120] L. Spitzer, *Physics of Fully Ionized Gases*. Wiley & Sons, 1962. 28

[121] P. A. Sturrock, *Plasma physics: an introduction to the theory of astrophysical, geophysical, and laboratory plasmas.* , Cambridge University Press, cup ed., 1994. 28, 35

[122] R. D. Carovillano and J. F. McClay, "Physics of the Magnetosphere," in *Physics of the Magnetosphere*, vol. 10, 1968. 29, 82, 83, 84

[123] J. Jokipii, "Turbulence and scintillations in the interplanetary plasma," *Annual Review of Astronomy and Astrophysics*, vol. 11, no. 1, p. 1–28, 1973. 30

[124] S. Chandrasekhar, "Stochastic problems in physics and astronomy," *Reviews of modern physics*, vol. 15, no. 1, p. 1, 1943. 31, 40

[125] D. T. Gillespie, *Markov processes: an introduction for physical scientists.* Elsevier, 1991. 31

[126] A. Shalchi, *Nonlinear Cosmic Ray Diffusion Theories.* Springer Science & Business Media, 2009. 32, 36, 38, 39, 43, 44

[127] N. J. Higham, ed., *The Princeton Companion to Applied Mathematics.* Princeton University Press, 2015. 33

[128] J. M. McDonough, "Introductory lectures on turbulence: physics, mathematics and modeling," 2007. 33

[129] O. Reynolds, "XXIX. An experimental investigation of the circumstances which determine whether the motion of water shall he direct or sinuous, and of the law of resistance in parallel channels," *Philosophical Transactions of the Royal Society of London*, vol. 174, p. 935–982, 1884. 33

[130] A. N. Kolmogorov, "The local structure of turbulence in incompressible viscous fluid for very large Reynolds numbers," in *Dokl. Akad. Nauk SSSR*, vol. 30, p. 299–303, 1941. 33

[131] A. N. Kolmogorov, "Dissipation of energy in locally isotropic turbulence," in *Dokl. Akad. Nauk SSSR*, vol. 32, p. 16–18, 1941. 33

[132] A. N. Kolmogorov, "Equations of turbulent motion in an incompressible fluid," in *Dokl. Akad. Nauk SSSR*, vol. 30, p. 299–303, 1941. 33

[133] A. N. Kolmogorov, "On the degeneration of isotropic turbulence in an incompressible viscous fluid," in *Dokl. Akad. Nauk SSSR*, vol. 31, p. 319–323, 1941. 33

[134] A. M. Y. A. S. Monin, *Statistical Fluid Mechanics, Volume I*. Courier Corporation, 2007. 33

[135] A. M. Y. A. S. Monin, *Statistical Fluid Mechanics, Volume II*. Courier Corporation, 2013. 33

[136] A. Tsinober, *An informal introduction to turbulence*, vol. 63. Springer Science & Business Media, 2001. 34

[137] D. Lohse and S. Grossmann, "Intermittency in turbulence," *Physica A: Statistical Mechanics and its Applications*, vol. 194, no. 1-4, p. 519–531, 1993. 34

[138] D. Biskamp, *Magnetohydrodynamic turbulence*. Cambridge University Press, 2003. 34

[139] S. Sridhar and P. Goldreich, "Toward a theory of interstellar turbulence. 1: Weak Alfvenic turbulence," *The Astrophysical Journal*, vol. 432, p. 612–621, 1994. 36

[140] P. Goldreich and S. Sridhar, "Toward a theory of interstellar turbulence. 2: Strong alfvenic turbulence," *The Astrophysical Journal*, vol. 438, p. 763–775, 1995. 36

[141] R. Schlickeiser, *Cosmic ray astrophysics*. Springer Science & Business Media, 2013. 36, 38, 40, 43

[142] G. K. Batchelor, *The Theory of Homogeneous Turbulence* . , Cambridge University Press, 1959. 36, 37

[143] A. Achterberg, Y. A. Gallant, C. A. Norman, and D. B. Melrose, "Intergalactic propagation of UHE cosmic rays," *arXiv preprint astro-ph/9907060*, 1999. 38, 40, 43, 46

[144] J. R. Jokipii, "Cosmic-ray propagation. I. Charged particles in a random magnetic field," *The Astrophysical Journal*, vol. 146, p. 480, 1966. 40

[145] A. Shalchi, "Second-order quasilinear theory of cosmic ray transport," *Physics of plasmas*, vol. 12, no. 5, p. 052905, 2005. 40

[146] C. Gardiner, *Stochastic methods*, vol. 4. springer Berlin, 2009. 40, 41

[147] B. Oksendal, *Stochastic Differential Equations*. Springer Science & Business Media, 2013. 42

[148] R. C. Davidson, *Methods in nonlinear plasma theory*. Pure and applied physics, v. 37, New York, Academic Press, 1972. 43

[149] D. Harari, S. Mollerach, E. Roulet, and F. Sanchez, "Lensing of ultra-high energy cosmic rays in turbulent magnetic fields," *JHEP*, vol. 0203, p. 045, Mar. 2002. 45, 71

[150] R. Aloisio and V. Berezinsky, "Diffusive propagation of ultra-high-energy cosmic rays and the propagation theorem," *The Astrophysical Journal*, vol. 612, no. 2, p. 900, 2004. 48, 57

[151] B. B. Mandelbrot, *The fractal geometry of nature*. , W. H. Freeman and Company, 1 ed., 1982. 50

[152] A. Keivani, G. R. Farrar, and M. Sutherland, "Magnetic Deflections of Ultra-High Energy Cosmic Rays from Centaurus A," *Astropart. Phys.*, vol. 61, p. 47–55, 2014. 53

[153] H. B. Kim, "Centaurus A as a point source of Ultra-High Energy Cosmic Rays," *Astrophys. J.*, vol. 764, p. 121, 2013. 53

[154] P. Abreu, M. Aglietta, E. Ahn, D. Allard, I. Allekotte, J. Allen, J. A. Castillo, J. Alvarez-Muñiz, M. Ambrosio, A. Aminaei, *et al.*, "Update on the correlation of the highest energy cosmic rays with nearby extragalactic matter," *Astroparticle Physics*, vol. 34, no. 5, p. 314–326, 2010. 53

[155] M. Kachelriess, S. Ostapchenko, and R. Tomas, "High energy radiation from Centaurus A," *New Journal of Physics*, vol. 11, no. 6, p. 065017, 2009. 53

[156] D. Fargion, "Light nuclei solving the AUGER puzzles: the Cen-A imprint," *Physica Scripta*, vol. 78, no. 4, p. 045901, 2008. 53

[157] K. Dolag, M. Kachelriess, and D. V. Semikoz, "UHECR observations and lensing in the magnetic field of the Virgo cluster," *JCAP*, vol. 0901, p. 033, 2009. 53, 74

[158] M. Giler, J. Wdowczyk, and A. W. Wolfendale, "Ultra-high-energy cosmic rays from clusters of galaxies," *Journal of Physics G: Nuclear Physics*, no. 12, p. 1561, 1980. 53

[159] V. Berezinskii, S. Grigor'eva, and V. Dogiel, "Predicted spectrum and anisotropy of the ultra-high energy cosmic rays in a single-source model," *Astronomy and Astrophysics*, vol. 232, p. 582–588, 1990. 53

[160] D. Harari, S. Mollerach, and E. Roulet, "Anisotropies of ultrahigh energy cosmic rays diffusing from extragalactic sources," *Phys. Rev. D*, p. 123001, Jun 2013. 53

[161] D. Harari, S. Mollerach, and E. Roulet, "Anisotropies of ultrahigh energy cosmic ray nuclei diffusing from extragalactic sources," *Phys. Rev. D*, p. 063014, Sep 2015. 53

[162] C. Isola, M. Lemoine, and G. Sigl, "Centaurus A as the source of ultrahigh-energy cosmic rays?," *Phys. Rev. D*, vol. 65, p. 023004, Dec 2001. 53

[163] P. Francis, *Étude mathématique du mouvement brownien de rotation.* PhD thesis, Université de Paris, 1928. 54

[164] K. V. Mardia, *Directional statistics*. Chichester New York: J. Wiley, 2000. 54, 55, 56

[165] P. H. Roberts and H. D. Ursell, "Random walk on a sphere and on a Riemannian manifold," *Phil. Trans. R. Soc. Lond. A*, vol. 252, no. 1012, p. 317–356, 1960. 55

[166] R. Fisher, "Dispersion on a sphere," in *Proceedings of the Royal Society of London A: Mathematical, Physical and Engineering Sciences*, vol. 217, p. 295–305, The Royal Society, 1953. 55

[167] D. Harari, S. Mollerach, and E. Roulet, "Angular distribution of cosmic rays from an individual source in a turbulent magnetic field," *Phys. Rev.*, vol. D93, no. 6, p. 063002, 2016. 56

[168] J. D. Hunter, "Matplotlib: A 2D graphics environment," *Computing In Science & Engineering*, vol. 9, no. 3, p. 90–95, 2007. 59

[169] M. Urban, "Comparison of Monte Carlo Generators for Ultra High Energy Cosmic Rays," Master's thesis, 2011. 62

[170] K. Dolag, D. Grasso, V. Springel, and I. Tkachev, "Constrained simulations of the magnetic field in the local Universe and the propagation of ultrahigh energy cosmic rays," *Journal of Cosmology and Astroparticle Physics*, vol. 2005, no. 01, p. 009, 2005. 66, 67

[171] E. Armengaud, G. Sigl, and F. Miniati, "Ultrahigh Energy Nuclei Propagation in a Structured, Magnetized Universe," *Phys.Rev. D*, vol. 72, p. 043009, Dec. 2005. 66, 67

[172] R. A. Batista, A. Dundovic, M. Erdmann, K.-H. Kampert, D. Kuempel, G. Müller, G. Sigl, A. van Vliet, D. Walz, and T. Winchen, "CRPropa 3—a public astrophysical simulation framework for propagating extraterrestrial ultra-high energy particles," *Journal of Cosmology and Astroparticle Physics*, vol. 2016, no. 05, p. 038, 2016. 66, 67, 98, 106

[173] S. Hackstein, F. Vazza, M. Brueggen, G. Sigl, and A. Dundovic, "Propagation of Ultra High Energy Cosmic Rays in Extragalactic Magnetic Fields: A view from cosmological simulations," July 2016. 67

[174] R. Alves Batista, M.-S. Shin, J. Devriendt, D. Semikoz, and G. Sigl, "Implications of strong intergalactic magnetic fields for ultrahigh-energy cosmic-ray astronomy," *Phys. Rev. D*, p. 023010, Jul 2017. 67

[175] J. M. Colberg *et al.*, "The Aspen–Amsterdam Void Finder Comparison Project," *Mon. Not. Roy. Astron. Soc.*, vol. 387, p. 933, 2008. 67

[176] P. A. R. Ade *et al.*, "Planck 2015 results. XIX. Constraints on primordial magnetic fields," *Astron. Astrophys.*, vol. 594, p. A19, 2016. 67

[177] R. Jansson and G. R. Farrar, "A new model of the galactic magnetic field," *The Astrophysical Journal*, vol. 757, no. 1, p. 14, 2012. 71, 105

[178] P. Abreu *et al.*, "Constraints on the origin of cosmic rays above 1018 ev from large-scale anisotropy searches in data of the pierre auger observatory," *The Astrophysical Journal Letters*, vol. 762, no. 1, p. L13, 2012. 72

[179] A. Aab *et al.*, "Multi-resolution anisotropy studies of ultrahigh-energy cosmic rays detected at the Pierre Auger Observatory," *JCAP*, vol. 1706, no. 06, p. 026, 2017. 72

[180] G. Cavallo, "On the Sources of Ultra-high Energy Cosmic Rays," *Astron. Astrophys.*, no. 65, 1978. 74

[181] W. G. Mathews and F. Guo, "Cosmic ray diffusion fronts in the Virgo cluster," *The Astrophysical Journal*, vol. 736, no. 1, p. 6, 2011. 74

[182] G. L. Harris, M. Rejkuba, and W. E. Harris, "The distance to NGC 5128 (Centaurus A)," *Publications of the Astronomical Society of Australia*, vol. 27, no. 4, p. 457–462, 2010. 76

[183] S. Mei, J. P. Blakeslee, P. Cote, J. L. Tonry, M. J. West, L. Ferrarese, A. Jordan, E. W. Peng, A. Anthony, and D. Merritt, "The ACS Virgo cluster survey. XIII. SBF distance catalog and the three-dimensional structure of the Virgo cluster," *The Astrophysical Journal*, vol. 655, no. 1, p. 144, 2007. 76

[184] K. M. Górski, E. Hivon, A. J. Banday, B. D. Wandelt, F. K. Hansen, M. Reinecke, and M. Bartelmann, "HEALPix: A Framework for High-Resolution Discretization and Fast Analysis of Data Distributed on the Sphere," *ApJ*, vol. 622, p. 759–771, Apr. 2005. 77

[185] P. Erdoğdu, J. P. Huchra, O. Lahav, M. Colless, R. M. Cutri, E. Falco, T. George, T. Jarrett, D. H. Jones, C. S. Kochanek, *et al.*, "The dipole anisotropy of the 2 micron all-sky redshift survey," *Monthly Notices of the Royal Astronomical Society*, vol. 368, no. 4, p. 1515–1526, 2006. 77

[186] V. López-Barquero, S. Xu, P. Desiati, A. Lazarian, N. Pogorelov, and H. Yan, "TeV Cosmic-Ray Anisotropy from the Magnetic Field at the Heliospheric Boundary," *The Astrophysical Journal*, vol. 842, no. 1, p. 54, 2017. 82

[187] H. Goldstein, C. Poole, and J. Safko, *Classical mechanics*. AAPT, 2002. 83

[188] W. Swann, "Application of Liouville's theorem to electron orbits in the Earth's magnetic field," *Physical Review*, vol. 44, no. 3, p. 224, 1933. 83

[189] G. Lemaître and M. S. Vallarta, "On Compton's latitude effect of cosmic radiation," *Physical Review*, vol. 43, no. 2, p. 87, 1933. 84

[190] C. Stömer, *The Polar Aurora*. Oxford University Press, 1955. 85

[191] C. Störmer, "Critical Remarks on a Paper by G. Lemaitre and MS Vallarta on Cosmic Radiation," *Physical Review*, vol. 45, no. 11, p. 835, 1934. 86

[192] W. E. Byerly, *An Elementary Treatise on Fourier's Series and Spherical, Cylindrical, and Ellipsoidal Harmonics, with Applications to Problems in Mathematical Physics*. Ginn & Company Publishers, 1893. 94

[193] E. Armengaud, G. Sigl, T. Beau, and F. Miniati, "Crpropa: a numerical tool for the propagation of uhe cosmic rays, gamma-rays and neutrinos," *Astropart. Phys.*, vol. 28, p. 463–471, 2007. 98

[194] K.-H. Kampert, J. Kulbartz, L. Maccione, N. Nierstenhoefer, P. Schiffer, G. Sigl, and A. R. van Vliet, "CRPropa 2.0–a public framework for propagating high energy nuclei, secondary gamma rays and neutrinos," *Astroparticle Physics*, vol. 42, p. 41–51, 2013. 98

[195] D. S. Walz, *Constraining models of the extragalactic cosmic ray origin with the Pierre Auger Observatory.* Dissertation, RWTH Aachen University, Aachen, 2016. Veröffentlicht auf dem Publikationsserver der RWTH Aachen University; Dissertation, RWTH Aachen University, 2016. 98

[196] G. Müller, *A search for sources of extragalactic cosmic rays using structured magnetic fields and advanced propagation software with the Pierre Auger Observatory.* Dissertation, RWTH Aachen University, Aachen, 2016. Veröffentlicht auf dem Publikationsserver der RWTH Aachen University 2017; Dissertation, RWTH Aachen University, 2016. 98

[197] L. Merten, J. B. Tjus, H. Fichtner, B. Eichmann, and G. Sigl, "CRPropa 3.1—a low energy extension based on stochastic differential equations," *Journal of Cosmology and Astroparticle Physics*, vol. 2017, no. 06, p. 046, 2017. 99

[198] A. Mücke, R. Engel, J. Rachen, R. Protheroe, and T. Stanev, "Monte Carlo simulations of photohadronic processes in astrophysics," *Computer Physics Communications*, vol. 124, no. 2-3, p. 290–314, 2000. 101, 106

[199] L. Euler, *Leonhardi Euleri Institutionum calculi integralis.-Volumen primum [-tertium].-Editio tertia.-Petropoli: impensis Academiae Imperialis Scientiarum, 1824-1827.-3 v.; 4o: 1: Volumen primum in quo methodus integrandi a primis principiis usque ad integrationem aequationum differentialium primi gradus pertractatur.* impensis Academiae imperialis scientiarum, 1824. 102

[200] J. D. F. Richard L. Burden, *Numerical Analysis* . Thomson Brooks/Cole, 2005. 102

[201] E. Fehlberg, "Low-order classical Runge-Kutta formulas with stepsize control and their application to some heat transfer problems," 1969. 102

[202] J. R. Cash and A. H. Karp, "A variable order Runge-Kutta method for initial value problems with rapidly varying right-hand sides," *ACM Transactions on Mathematical Software (TOMS)*, vol. 16, no. 3, p. 201–222, 1990. 102

[203] J. Giacalone and J. Jokipii, "The transport of cosmic rays across a turbulent magnetic field," *The Astrophysical Journal*, vol. 520, no. 1, p. 204, 1999. 105

[204] G. Giacinti, M. Kachelrieß, D. Semikoz, and G. Sigl, "Ultrahigh energy nuclei in the turbulent galactic magnetic field," *Astroparticle Physics*, vol. 35, no. 4, p. 192–200, 2011. 105

[205] M. Frigo and S. G. Johnson, "FFTW: An adaptive software architecture for the FFT," in *Acoustics, Speech and Signal Processing, 1998. Proceedings of the 1998 IEEE International Conference on*, vol. 3, p. 1381–1384, IEEE, 1998. 105

[206] M. Pshirkov, P. Tinyakov, P. Kronberg, and K. Newton-McGee, "Deriving the global structure of the galactic magnetic field from Faraday rotation measures of extragalactic sources," *The Astrophysical Journal*, vol. 738, no. 2, p. 192, 2011. 105

[207] H.-P. Bretz, M. Erdmann, P. Schiffer, D. Walz, and T. Winchen, "PARSEC: a parametrized simulation engine for ultra-high energy cosmic ray protons," *Astroparticle Physics*, vol. 54, p. 110–117, 2014. 106

Eidesstattliche Versicherung

Hiermit erkläre ich an Eides statt, dass ich die vorliegende Dissertationsschrift selbst verfasst und keine anderen als die angegebenen Quellen und Hilfsmittel benutzt habe.

Declaration on oath

I hereby declare, on oath, that I have written the present dissertation by my own and have not used other than the acknowledged resources and aids.

Andrej Dundović

Acknowledgement

Words and sentences in this work are a product of my own thoughts and capacities. However, all of these did not come from nowhere, and this work certainly would not be possible without many benefactors, and I can hardly name them all.

I have to thank my supervisor, Prof. Günter Sigl, who took me in his group, and secured the necessary conditions for my Ph.D. - without him this work certainly would not be possible. In addition, his vast knowledge of concepts and works in the field of research, that no online search engine can match, helped me in many occasions when I stuck in doubts or struggle with questions regarding physics. I thank Peter Niksa and Andrey Saveliev, and other members of the theoretical astroparticle group, both ex and present, not only for their help and time in professional matters but in out-of-office matters, too. I grateful to the people in the Pierre Auger Collaboration, youngsters and seniors, for making me the subject of cosmic rays closer, and certainly more real.

I appreciate the help from David Walz, Gero Müller and Tobias Winchen regarding CRPropa and related topics, and I particularly thank Tobias for reviewing the CPRpropa appendix of this thesis.

My thanks go to Stefan Hackstein, a fellow in the battles of Liouville, for endless discussions, and efforts to understand better those anisotropies. He also translated the abstract of this thesis for me, to the language which I, unfortunately, did not master.

I am indebted to Natacha Leite, my trustworthy and lovely office mate who offered me many joyful, supportive and helpful conversations. She also went through a tedious work of proofreading the whole thesis, and all those errors, which are left in the text, are introduced by me after the proofreading.

I am grateful to the teachers who influenced me the most through my education and pushed me to the path of science: Tomislava Topolovec, Vlasta Starčević, Marko Barić, and Ratko Višak.

I could not go through all my endeavours without the support of my family. It's a cliché, but this acknowledgement would be untruthful and without the meaning if I do not mention my parents and sister on whom I can always rely on.

I'm thankful to my secret admirer, for giving me joy and inspiration, especially needed during these times that were poor with romance and intuition.

My comrade and flatmate Petar, I thank for reaching this point on my scientific journey. He undoubtedly had a tremendous influence on my life in the last four years. Not only for endless discussions about physics and metaphysics, music and arts, religion and history, politics and society, among many other topics during long sleepless nights in Hamburg, but I also thank him for his friendship, for sharing the everyday difficulties of living in a foreign country which made these three years much more pleasant than it could be without him. I immodesty did expect friendship from him before we started this journey, but I also got a great teacher for many subjects that could be hardly found elsewhere.

Although it is not a person, I acknowledge the city of Hamburg, its riverbanks, canals and bridges, for giving me a sanctuary for contemplation in the last three years.